P-112

STANFORD UNIVERSITY

Guidance and Control Laboratory

Final Report Grant No. NCA2-IR745-407

SPACE INFRARED TELESCOPE POINTING CONTROL SYSTEM

INFRARED TELESCOPE TRACKING IN THE PRESENCE OF TARGET MOTION

Submitted to
NASA AMES RESEARCH CENTER
Moffett Field, Calif. 94035

by
J. David Powell, Principle Investigator
Julie Benson Schneider, Research Assistant

Guidance and Control Laboratory
Department of Aeronautics and Astronautics
STANFORD UNIVERSITY
Stanford, California 94305

June 6, 1986

Final Report Grant No. NCA2-IR745-407

SPACE INFRARED TELESCOPE POINTING CONTROL SYSTEM

INFRARED TELESCOPE TRACKING IN THE PRESENCE OF TARGET MOTION

submitted to
NASA AMES RESEARCH CENTER
Moffett Field, Calif. 94035

by
J. David Powell, Principle Investigator
Julie Benson Schneider, Research Assistant

Guidance and Control Laboratory
Department of Aeronautics and Astronautics
STANFORD UNIVERSITY
Stanford, California 94305

June 1986

Abstract

The use of charge-coupled-devices, or CCD's, has been documented by a number of sources as an effective means of providing a measurement of spacecraft attitude with respect to the stars. A method exists of defocussing and interpolation of the resulting shape of a star image over a small subsection of a large CCD array. This yields an increase in the accuracy of the device by better than an order of magnitude over the case when the star image is focussed upon a single CCD pixel. This research examines the effect that image motion has upon the overall precision of this star sensor when applied to an orbiting infrared observatory. While CCD's collect energy within the visible spectrum of light, the targets of scientific interest may well have no appreciable visible emissions.

Image motion has the effect of 'smearing' the image of the star in the direction of motion during a particular sampling interval. As the interpolation process effectively finds the centroid of the image read out from the CCD pixels, the fact that the star was actually at the extreme end of the smeared image at the end of the sampling period must be accounted for. In addition, errors grow rapidly if the star moves off the edge of the integration area. This problem may be remedied in part by the use of larger integration areas, but this has drawbacks as well. A compromise may be selected by increasing the size of the readout array in the direction of motion, as opposed to the normally square integration area used for a

stationary star image. Shorter integration times also help to relieve the problem, but are limited in their usefulness where dim stars are involved.

The major reason that increasing the size of the integration area does not eliminate the problem of off-edge scanning is the increased noise content of the interpolated signal that results. There are many different sources that contribute to the overall noise level of the CCD measurement, but they may be broken into two general categories; background noise and shot noise. The larger the array, the more noise electrons will be present with a larger 'moment-arm' about the array center, thus skewing the interpolation process. Image motion is shown to have a slight, but unimportant effect upon the noise content of the signal.

For purposes of estimating gyro drift with a Kalman filter using star tracker measurements, a noise analysis of a candidate dry-tuned gyro for the mission was performed. Data for this analysis is drawn from manufacturer literature. A satisfactory curve is fit to gyro Power Spectal Density data.

The presence of image motion is incorporated into a Kalman filter for the system, and it is shown that the addition of a gyro command term is adequate to compensate for the effect of image motion in the measurement. The updated gyro model is included in this analysis, but has natural frequencies faster than the projected star tracker sample rate for dim stars. The system state equations are reduced by modelling gyro drift as a white noise process. There exists a tradeoff in selected star tracker sample time between the CCD, which has improved noise characteristics as sample time increases, and the gyro, which will potentially drift further between long attitude updates. A sample time which mimimizes pointing estimation error exists for the random drift gyro model as well as for a random walk gyro model.

Table of Contents

List of Figures

List of Tables

List of Symbols

A_1	SIRTF effective aperture area
D	Random walk gyro drift
D_1	SIRTF effective aperture diameter
$\bar{D}$	Predicted estimate of gyro drift prior to star measurement
err_{cent}	Centroid timing error
E_1	SIRTF optical transmissivity
$\mathbf{F}$	System dynamics matrix (continuous)
G_c	Control distribution matrix (continuous)
G_n	Process noise distribution matrix (continuous)
$G_x(\omega)$	PSD of gyro input
$G_y(\omega)$	PSD of gyro output
$H_g(s)$	Transfer function of gyro noise shaping filter
H	Star tracker measurement matrix
i_0	Maximum CCD surface charge density
j	$\sqrt{-1}$ except when used as summation index
$\tilde{k}$	Star position uncertainty due to noise in the ith line spread
$\hat{k}$	Calculated image centroid with respect to pixel matrix center
k'	Corrected calculated image centroid with respect to pixel matrix center

K	Measurement feedback gain matrix
K_n	Gain of gyro PSD model
$\mathbf{M}$	Estimate–error covariance matrix prior to measurement
m_p	Number of pixel subarray columns
M_v	Visual Star Magnitude
n	Discrete time step counter (Chapter Five)
n_b	CCD background noise
n_{ij}	Noise in (i,j)th pixel signal
n_p	Number of pixel subarray rows, and columns if square
n_{ct}	Noise contribution due to CCD charge transfer inefficiency
n_{sn}	CCD shot noise
n_w	Noise input driving gyro noise model
$\mathbf{P}$	Estimate–error covariance matrix following a measurement
q	Total surface charge for uniform CCD array
Q	Process noise covariance matrix
R	Measurement noise covariance matrix
R_0	CCD photresponse as a function of star magnitude
R_1	Trapezoidal star image approximationupper radius
R_2	Trapezoidal star image approximation lower radius
s	Laplace Transform variable
S	Sum of all line spreads, or total signal level present on array
S_i	ith line spread (row or column sum) of pixel signals
$\bar{S}$	Moment of line spreads about center of pixel subarray
$\bar{S}_i$	Mean value of ith line spread

$\tilde{S}_i$	Noise in the ith line spread
S_{ij}	(i,j)th pixel signal
t	Time
T	Star tracker sampling interval
u	Control input
v	Star tracker measurement noise
w	Process noise
X	Gyro shaping filter auxiliary state variable
$\mathbf{x}$	State vector
$\hat{\mathbf{x}}$	Current state–estimate vector
$\bar{\mathbf{x}}$	Predicted state–estimate vector
y	System measurement

Greek Symbols

Φ	Discrete system matrix
Γ_c	Discrete control distribution matrix
Γ_n	Discrete process–noise distribution matrix
ω	Frequency
ω_1	Numerator break frequency for gyro noise model
ω_2	Natural frequency for gyro noise model
ζ	Damping ratio
θ_I	Image position on CCD array
$\bar{\theta}_I, \hat{\theta}_I$	Predicted and current estimates of θ_I
Θ	Integral of image position

Θ'	Θ delayed by one star–tracker sampling period
$\dot{\theta}_c$	Commanded rate input of telescope
θ_m	Measured image position on CCD array
ϵ	CCD charge transfer efficiency factor
τ	Integration variable

Other Symbols

$int()$	Computational integer value of some number
$sgn()$	Polarity of value in the argument
μ	micro or 10^{-6}
PSD	Power Spectral Density
E()	Expected value
$(\dot{})$	Time derivative
$\approx$	Approximately equal to

Chapter 1

Introduction

Background Information The NASA Space Infrared Telesope Facility (SIRTF) is being proposed to allow astronomers to examine interstellar targets that have been previously inaccessible to uncontaminated study. This type of target might typically include interstellar gas clouds where new star systems may be forming and distant galaxies which seem to radiate most of their energy in the infrared spectrum as well as closer targets, such as comets and moons. The resolution of such studies has been previously limited in earth–based telescopes by interference from atmospheric radiation. While telescopes launched by balloon or installed in special aircraft have had some success, a space–based infrared observatory (IRAS) was launched in January, 1973. During its relatively short life, it collected enough valuable information to justify the development of a larger, higher resolution, serviceable telescope to be known as SIRTF.

SIRTF is being developed as a one meter class, free flying, cryogenically cooled observatory. Initial design studies conceived SIRTF as a fixed package making observations from the payload cargo bay of the Space Shuttle, mounted upon a gimballed platform. Placement on the Space Shuttle, which uses mass expulsion de-

vices for attitude control and suffers from the disturbances of astronaut movement within the cabin, places extra limitations upon telescope performance, however. Demands from the scientific community for increased flight time and improved accuracy has led to the current ongoing development of SIRTF as a free flying spacecraft. The configuration of SIRTF is not yet finalized, but two proposed designs are shown in Figure 1–1 [SAL–1]. In addition, Figure 1–2 shows the optical configuration for this telescope. The differences between the two configurations arise from whether the spacecraft was designed for a sun–synchronous polar orbit with a 98 degree inclination or an equatorial orbit of 28 degree inclination. Both are targeted for relatively low earth orbit (700 and 600 km, respectively) [SAL–1]. The spacecraft is currently projected for launch in the early 1990's.

The design of a very accurate pointing and tracking control system for SIRTF is subject to several handicaps not found in most three–axis stabilized spacecraft [SAL–1]. The majority of these satellites use some form of thrusters for basic control or reaction wheel momentum dumping. However, inasmuch as the presence of mass expulsion devices have helped make the shuttle an unacceptable platform, so, too, would they contaminate the focal plane of a free–flyer. The large, liquid helium–filled hollow structure of the telescope also provides a set of flexibility and cryogen slosh challenges which must be included in control system design.

The pointing requirements for SIRTF are quite tight, as would be expected for a space–based telescope. The control sensor strategy has previously been developed around a combination of a Fine Guidance Sensor (FGS), which provides inertial attitude information with respect to the stars and conventional attitude gyroscopes. The FGS star sensor thus provides long term stability by updating satellite attitude relative to fixed visible guide stars, but, due to its relatively slow data rate, must be augmented by conventional gyros to provide short–term stability between star

tracker samples. Thus, in this pairing, the star sensor provides a basis for correction of gyro error and drift. Table 1.1 contains a summary of the Fine Guidance Sensor specifications for SIRTF.

Table 1–1
SIRTF FGS Specifications

Guidance Field of View	1800 arcseconds dia.
Offset Pointing Accuracy	0.1 arcsecond
Noise Equivalent Angle	0.125 arcsecond
Sensitivity, M_v	
Required	≥ 14
Goal	≥ 16
Multiple Target Capability	
Video Signal	
Detector Operating Temperature	≤ 150 K
Data Rate	≥ 1 per second

The NASA-Lockheed Space Telecope is a recent project of similar scope and purpose as SIRTF. However, as Space Telecope was scheduled to fly in late 1986, it is based on slightly older technologies. An important difference, in terms of its effect on configuration and control system philosophy, between these two spacecraft is the fact that nearly all of Space Telecope's experiments and observations will be carried out in the spectrum of visible radiation. This allows for direct acquisition and tracking of the target of interest (if it is of sufficient brightness). The attitude sensor hardware selected for use on Space Telescope consists of a combination of photomultiplier tubes for fine guidance, fixed head star trackers for coarse guidance, and rate gyros [DOU–1]. As described previously for SIRTF, the photomultiplier

tubes and star trackers provide long-term attitude information, while the gyros provide short-term rate and position data. The use of photomulitplier tubes in Space Telescope is quite complex, however. Each of the four tubes has an effective field of view of 3 arc-sec^2, while the total required FGS field of view is about 60 arc-min^2. In addition, the tubes are used in an interferometric mode during fine pointing, which leads to a limited dynamic range. To accomplish this task, the tubes are combined with rate control systems which contain rotating prisms to manuever the limited field of view of the photomultiplier tube over the entire FGS area. In effect, the star sensor itself is steered so that the target remains within its field of view.

In contrast, the FGS star tracker being targeted for use on SIRTF is a flat–plane charge–coupled–device, or CCD. It achieves a high level of accuracy without either the field-of-view limitations or need for interferometry of the photomultiplier tubes of Space Telescope ([EIS–1], [GOS–1], [HIL–1], [MAR–1 and –2], [S&G–1] and [S&H–1]). Some of the advantages of this instrument are high performance, maintenance of precision in a very cold environment as provided by close proximity to cryogenics, and low power consumption. The gyroscope hardware currently being examined consists of Teledyne dry–tuned gyros, favored for their low noise and drift characteristics.

Purpose Many targets of interest to the scientific community on this mission are not necessarily stationary with respect to the guide stars used to orient the telescope. Targets of this sort include planets, planetary moons and comets. Therefore SIRTF should also have the capability to track a moving target. It is also worth noting that the moving scientific target may not have appreciable emissions in the visible spectrum where the spacecraft star tracker is effective. The issues discussed by this work include the effect that motion has upon the performance of

the fine guidance sensor and a discussion of a Kalman filter formulation designed to estimate gyro drift based upon the star tracker measurement of attitude.

A brief summary of the contents of this report follows:

Chapter Two describes the operation of CCD's for star sensing applications and gives a review of past work that studies the use of CCD's as star trackers.

Chapter Three introduces the problem of tracking targets in motion. A simulation routine for the CCD is developed which is used to estimate of the accuracy of this sensor for this application. Some limitations of CCD performance under these conditions are presented.

Chapter Four reviews the noise levels that may be expected from the Fine Guidance Sensor and also develops a noise model for the candidate gyro to be flown on this mission, the NASA Standard DRIRU II.

Chapter Five investigates tracking motion with a the incorporation of a Kalman Filter in the FGS system for estimation of gyro drift using the results of Chapters Three and Four. Past work is reviewed, and modifications required for the moving target and updated gyro model are presented.

The conclusions of this research are presented in Chapter Six.

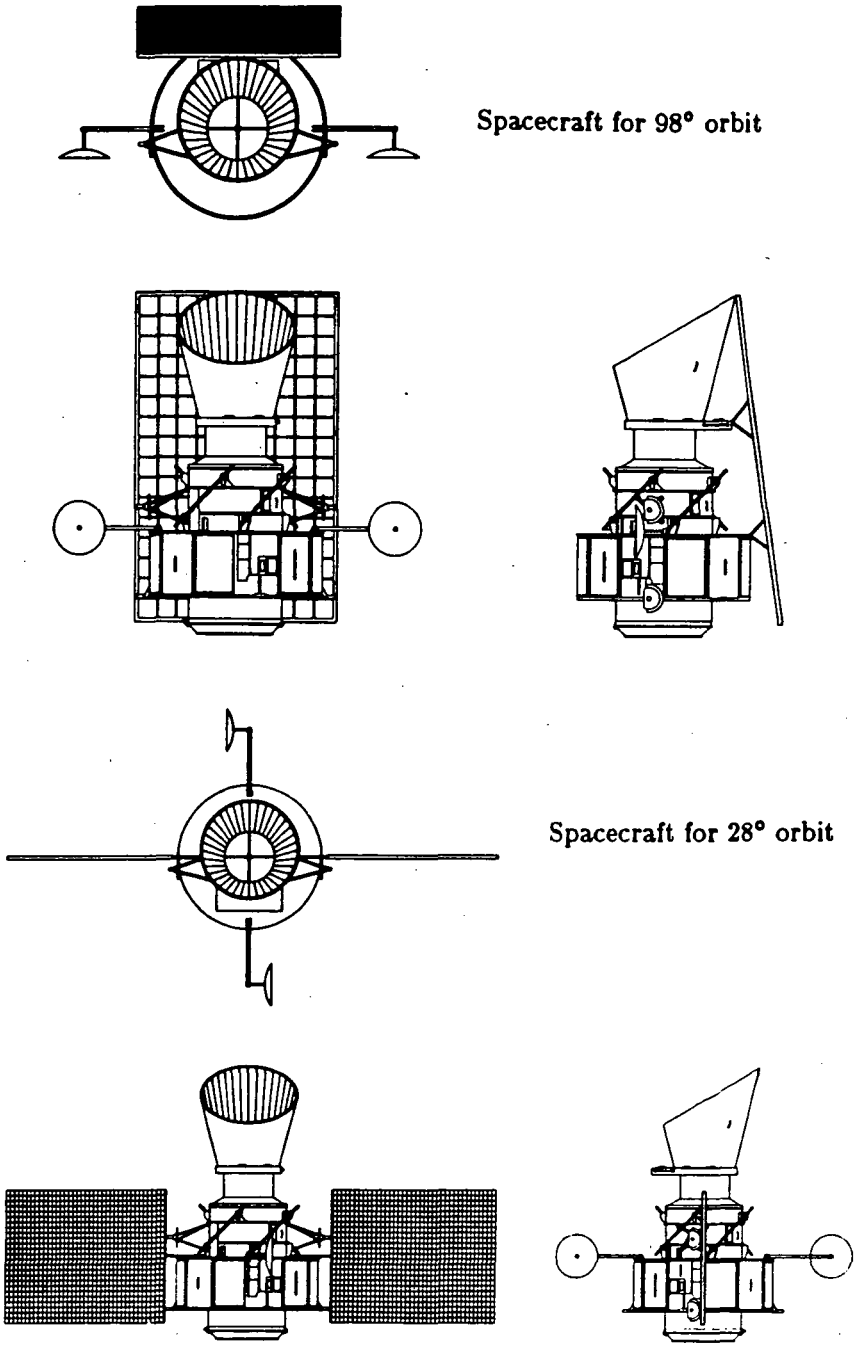

Figure 1–1 Proposed SIRTF configurations [SAL–1]

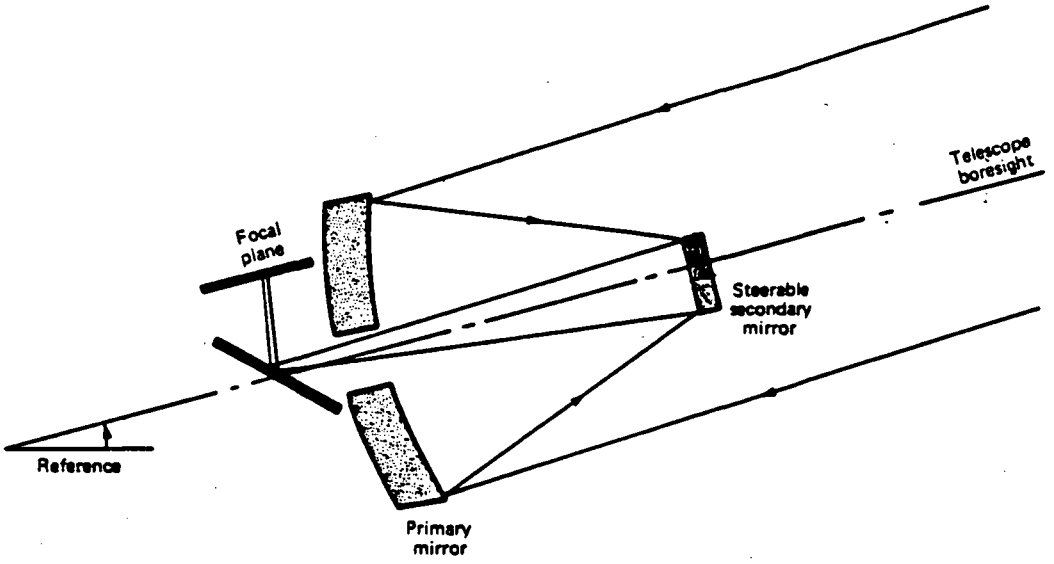

Figure 1–2 Proposed SIRTF optical model [PSH–1]

Chapter 2

Review

The system currently being proposed for use as a fine guidance star sensor for SIRTF is based upon the use of a CCD, or charge–coupled device. These small semiconductor chips are divided into an array of radiation–sensitive pixels, which may then be combined with optical elements to provide a signal based upon star position. This chapter will summarize some of the basic characteristics and limitations of CCD's when used for this application, as well as provide a review of the work previously done for the case of a stationary star image. A presentation of hardware characteristics and assumptions about the star image will be made. Finally, the computer routine that was extensively used to simulate CCD performance will be described.

The operation of a CCD for this application is based on the device's ability to count the photoelectrons of incident light hitting a pixel element. Each pixel of the array is connected to read–out registers which transfer the signal to processing electronics. The charge developed on a given pixel is thus proportional to the amount of photons incident to the pixel up to some saturation level. The time

allowed for a charge to build, or integration time, is selectable and will in practice vary with the brightness of the object being sensed. The read–out registers and processing electronics have the ability to identify each pixel and its signal uniquely for purposes of identification and tracking.

The resolution of the system is automatically limited to the size of a pixel element if the star image is focussed on a single pixel. Typically, a CCD array might have a total field of view of 30 arc–minutes which would limit the accuracy to about 4.5 arc–seconds for an array 400 pixels square. Noise and other error sources also contribute to the total resolution. Since the SIRTF baseline specifications are far more stringent than this, the quality of the signal must somehow be enhanced.

The method for accomplishing this goal has been developed by Jet Propulsion Laboratories ([S&G–1],[S&H–1], [GOS–1] and [MAR–1]). The accuracy of the CCD when used as an image detector may be improved by better than an order of magnitude by a process of defocussing and interpolation. The defocussing process increases the number of pixels that a given star is imaged upon. In this way the size of the image is increased from less than a pixel to a size that will fit on a subarray that is three or four pixels square (Figure 2–1). The centroid of the image, based upon the first moment of the row and column pixel signals about the subarray center, is interpolated both horizontally and vertically to yield a calculation of the position of the star. The interpolation routine uses the individual pixel signal levels, or point spread, S_{ij} (i =row, j =column), as follows:

The vertical line spread, or horizontal sums of the point spread, is given by

$$S_i = \sum_{j=1}^{n_p} S_{ij} \qquad i = 1, n_p \tag{2.1}$$

where n_p is the number of vertical pixels in the subarray.

The horizontal line spread is given by

$$S_j = \sum_{i=1}^{m_p} S_{ij} \qquad j = 1, m_p \tag{2.2}$$

where m_p is the number of horizontal pixels in the subarray.

The first moment of each line spread about the center of the pixel subarray may then be written as

$$\overline{S} = \sum_{i=1}^{int(n_p/2)} \left(\frac{n_p + 1}{2} - i \right) \left(S_{n_p+1-i} - S_i \right) \tag{2.3}$$

or, specifically, for a 4x4 array,

$$\overline{S} = 1.5(S_4 - S_1) + 0.5(S_3 - S_2) \tag{2.4}$$

or a 3x3 array,

$$\overline{S} = (S_3 - S_1) \tag{2.5}$$

Naturally, the same equation applies whether the estimated centroid of either the horizontal or vertical line spread is to be found. In addition, the total signal is given by

$$S = \sum_{i=1}^{n_p} \sum_{j=1}^{m_p} S_{ij} \tag{2.6}$$

The star image position is then found by dividing the first moment of the line spread calculated above by the total signal, or

$$\hat{k} = \frac{\overline{S}}{S} \tag{2.7}$$

where $\hat{k}$ is the estimated star position with respect to the center of the subarray.

The accuracy of this process is limited by several things. Perfect precision is impossible due to the fact that the CCD is basically an integer device that develops a charge related to the count of whole numbers (not fractions) of photoelectrons that occur during a given integration period. Centroid errors of this sort decrease with increasing integration time due to the fact that the total signal level is relatively greater and the effects of this sort of 'quantization' error tend to become less significant. This effect is demonstrated in Figure 2–2 by plotting error levels compared to signal levels. The solid line on the error graph represents the error that would exist if the CCD had no quantization effects. The dashed line demonstrates how the actual error approaches this limiting value with increasing signal level. If the signal levels are large, the device error becomes small when compared to overall specifications, but must be considered to be a factor if high integration rates and dim stars are to be combined in operation.

Another limitation can be the physical configuration of the device itself. Two different instruments were analyzed during this course of the study. These were the Fairchild 211 CCD and the RCA 501 CCD (Figure 2–3). Characteristics of each of these are summmarized in Table 2–1. While the RCA or a similar device is most likely to be selected as flight hardware, the Fairchild was initially considered

during the early phases of this research. It will be presented here briefly as it has a unique configuration that raises several interesting issues.

Table 2–1
CCD Specifications

	Fairchild	RCA
Array size	244 rows 190 columns	320 rows 512 columns
CCD element subtense, SIRTF optics	6.136 arcsec horizontal 3.689 arcsec vertical	5.625 arcsec square
Element dimensions	30μm horizontal 18μm vertical	30μm square
Saturation	250,000e^-	390,000e^-

The Fairchild CCD is an instrument designed with older technology and requires the presence of opaque charge–transfer registers which collect no signal interspersed between columns of charge–collecting pixels. In addition, the pixels themselves are not square. The opaque registers result in a loss of usable signal for the device, which is demonstrated by Figure 2–4 for a simple star image intensity profile spread over a 4x4 pixel subarray. These factors can cause certain amounts of position error when used in conjunction with the simple centroid Equation 2.7. The errors were found to be regular with respect to the position of the star image on the face of the device, both horizontally and vertically (Figure 2–5). The vertical errors were linear with the actual star position, while the horizontal errors were found to be quadratic, of magnitude up to 0.5 arcsecond. Curves were be fit to these errors, however, which resulted in the following corrections to the

interpolation: [P&P–1]

$$k'_{vertical} = 1.35\hat{k}_{vertical}$$
$$k'_{horizontal} = sgn(\hat{k}_{horizontal})\left(-0.7024 + \sqrt{0.4933 + 1.898|\hat{k}_{horizontal}|}\right) \quad (2.8)$$

The application of these equations reduces the overall error of the device to acceptable levels, as shown by Figure 2–6. The effect of star image shape upon the constants in these equations was never assessed.

The RCA device, on the other hand, has square pixel elements and also contains no opaque registers that result in signal loss (Figure 2–7). Thus, with the inherent integer nature of the device as a basic limitation, the algorithm should work accurately and have identical vertical and horizontal error curves. The typical variation in error with star image position for a 4x4 subarray is shown in Figure 2–8. Note the magnitude of the error is less than 0.003 arcseconds and is largely due to the effect of 'photon counting' described previously. These errors take on a sinusoidal component and could obviously be fitted, if required, with a Fourier series of two terms.

Other inaccuracies of the device are more dependent upon variations of each individual CCD due to manufacturing irregularities as well as imperfections in the imaging optics. These errors are significant and result in different corrections at different locations on the 320x512 CCD array. Work in this area is being accomplished by Glavich and Goss [G&G–1], who have developed an adaptive tracking algorithm which moves an image in steps across a pixel, measures the resulting errors and then develops a polynomial correction of up to five terms. On–board electronics would thus make the neccesary correction to the measurement depending on the location of the star on the entire CCD array. The contrast between

the corrected and uncorrected errors for a sample device is shown in Figure 2–9. Note that, after correction, the errors take on a similar sort of sinusoidal type of characteristic as discussed previously.

Several topics merit a brief discussion in regard to the computer routine used to generate the error characteristics shown in Figures 2–3 and 2–5—2–9. The original algorithm (Appendix A–1) was developed by Parsons [PAR–1] utilizing the physics of the Fairchild device combined with a baseline 4x4 pixel subarray. It has since been modified extensively by this author to include different physical characteristics, most notably those changes required to support the newer RCA device, different subarray sizes–including nonsquare cases, and most especially, a nonstationary image. While some of these topics will be addressed more completely in subsequent chapters, a few important considerations will be addressed here.

The basic algorithm simulated the signal generated on a pixel element by making use of the fact that the charge developed on a CCD by incident radiation is dependent on the number of photons hitting the device. From Hill [HIL–1], a CCD with no insensitive areas ideally collects a charge of

$$q = A_1 E_1 R_0 T \text{ photoelectrons} \tag{2.9}$$

where

T = integration time (seconds)

A_1 = effective aperture area = $\pi(\frac{D_1}{2})^2$ (m^2)

E_1 = overall optical transmissivity (%)

R_0 = CCD photoresponse as a function of star magnitude (photoelectrons/sec-m^2)

D_1 = effective aperture (m)

or, specifically for the Fairchild array using SIRTF parameters,

$$D_1 = 1 \text{ m}$$

$$E_1 = 60\%$$

$$R_0 = (1.54912 \times 10^{10}) 10^{-0.4M_v} \text{ photoelectrons/sec-m}^2$$

so that

$$q = (7.3 \times 10^9) * 10^{-0.4M_v} * T \text{ photoelectrons} \qquad (2.10)$$

When applied to the simple distribution shown in Figure 2–3, the maximum intensity, i_0, is the 'height' of the image shown in Figure 2–3 and is determined for simulation purposes by setting the total charge developed during time T equal to the "volume" of the shape, and solving for i_0, or, for this case,

$$i_0 = \frac{q}{\frac{1}{3}\pi \left(R_1^2 + R_2^2 + R_1 R_2\right)} \text{photoelectrons}/\mu\text{m}^2 \qquad (2.11)$$

where R_1, R_2, and i_0 are as shown in Figure 2–3.

As the purpose of this research was conceptual, rather than quantitative, and based upon the assumption that the optical and radiative properties for SIRTF will change several times before flight, these overall charge sensitivities were also used in the computer simulation of signals for the RCA device. This is expected to have no significant impact on the major findings of this analysis.

Previous studies ([G&G–1], [MAR–2]) have reported that the accuracy of the interpolation/centroiding algorithm is quite sensitive to the actual distribution of intensity of the star image. Preliminary SIRTF studies ([MAR–3], [P&P–1])

suggested that, given the optical parameters (Figure 2–10) selected at that time, that a trapezoidal image profile was representative of a typical star when defocussed throught the FGS optics. We have seen a contour plot of the intensity profile of an actual star image (Figure 2–1) when defocussed through more recent optics. Figure 2–11 shows a cross–sectional 'slice' of that contour plot. With the exception of the sharp intensity spike in the center of the figure, the trapezoidal approximation can be seen to be a viable, yet computationally simple, model. Obviously a large number of distributions exist which more accurately mimic the 'typical' star image shape and work has been accomplished in this area [G&G–1]. Table 2–2 shows a list of possible image distributions currently being explored by JPL. A combination of actual empirical results from actual star images as well as a sensitivity analysis of the algorithm to star image shape is important to accomplish before flight, but is beyond the scope and purpose of this report, and will not affect the major findings herein.

Table 2-2
Candidate Artificial Point Spread Functions [GOV-1]

1. Intensity $= A_0 + \sum_1^5 A_N R^{-N}$
2. Intensity $= A_0 + \left[\sum_1^5 A_N X^{-N}\right]\left[\sum_1^5 B_N Y^{-N}\right]$
3. Intensity $= A_0 + A_1 \exp\left[-A_2 (R - A_3)^2\right]$
4. Intensity $= A_0 + \exp\left[-A_2 (X - A_3)^2\right] \exp\left[-A_4 (Y - A_5)^2\right]$
5. Intensity $= A_0 + A_1 \left[\frac{J_1(2\pi A_2 R)}{2\pi A_2 R}\right]^2$
6. Intensity $= A_0 + A_1 \left[\text{sinc}^2 (2\pi A_2 X)\right]\left[\text{sinc}^2 (2\pi A_3 Y)\right]$
7. Point by Point Sums or Products of Any of These

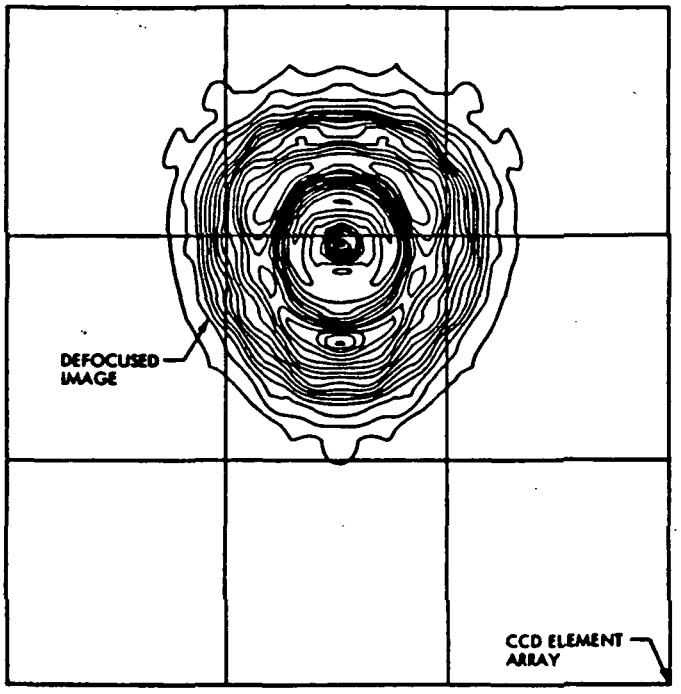

Figure 2–1 Contour plot of actual star image [G&G–1]

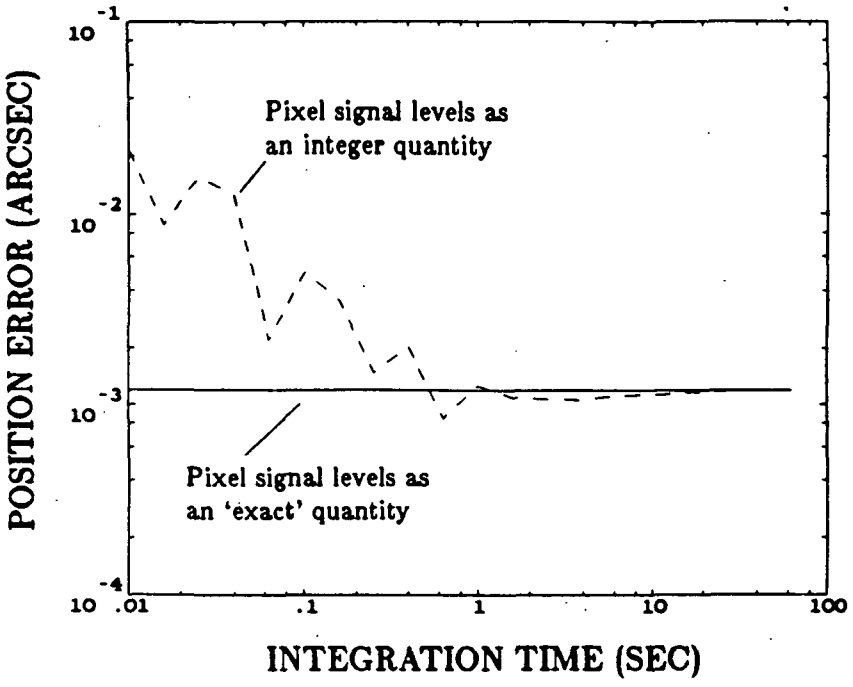

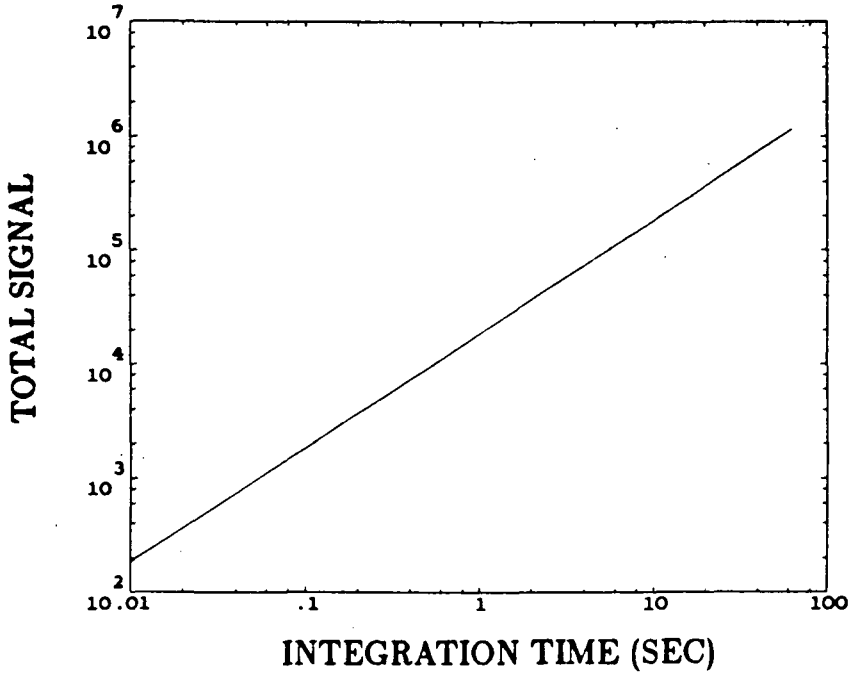

Figure 2–2 Effect of total signal level on centroid error

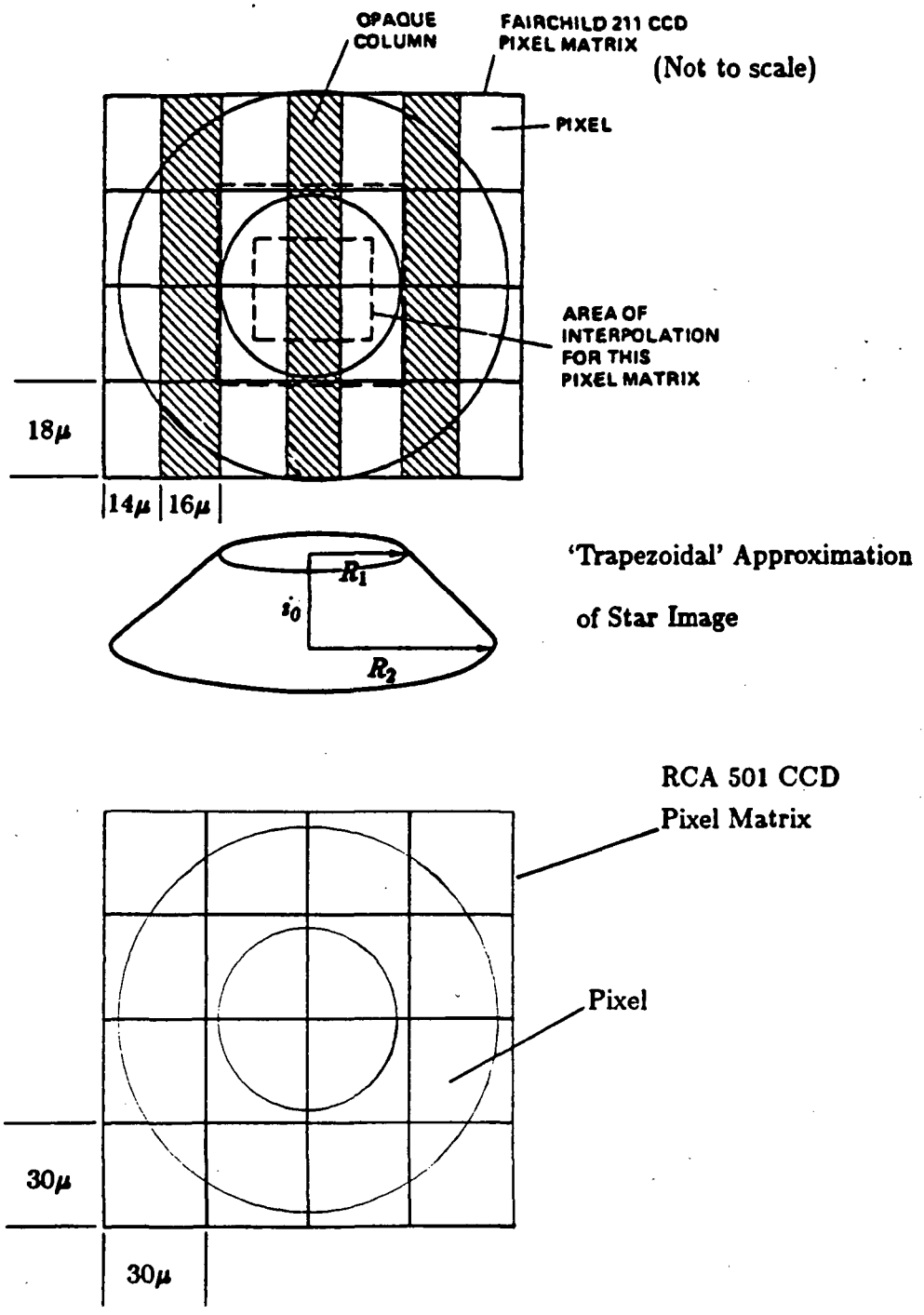

Figure 2–3 Configuration comparison between the Fairchild 211 CCD and the RCA 501 CCD with assumed star image shape

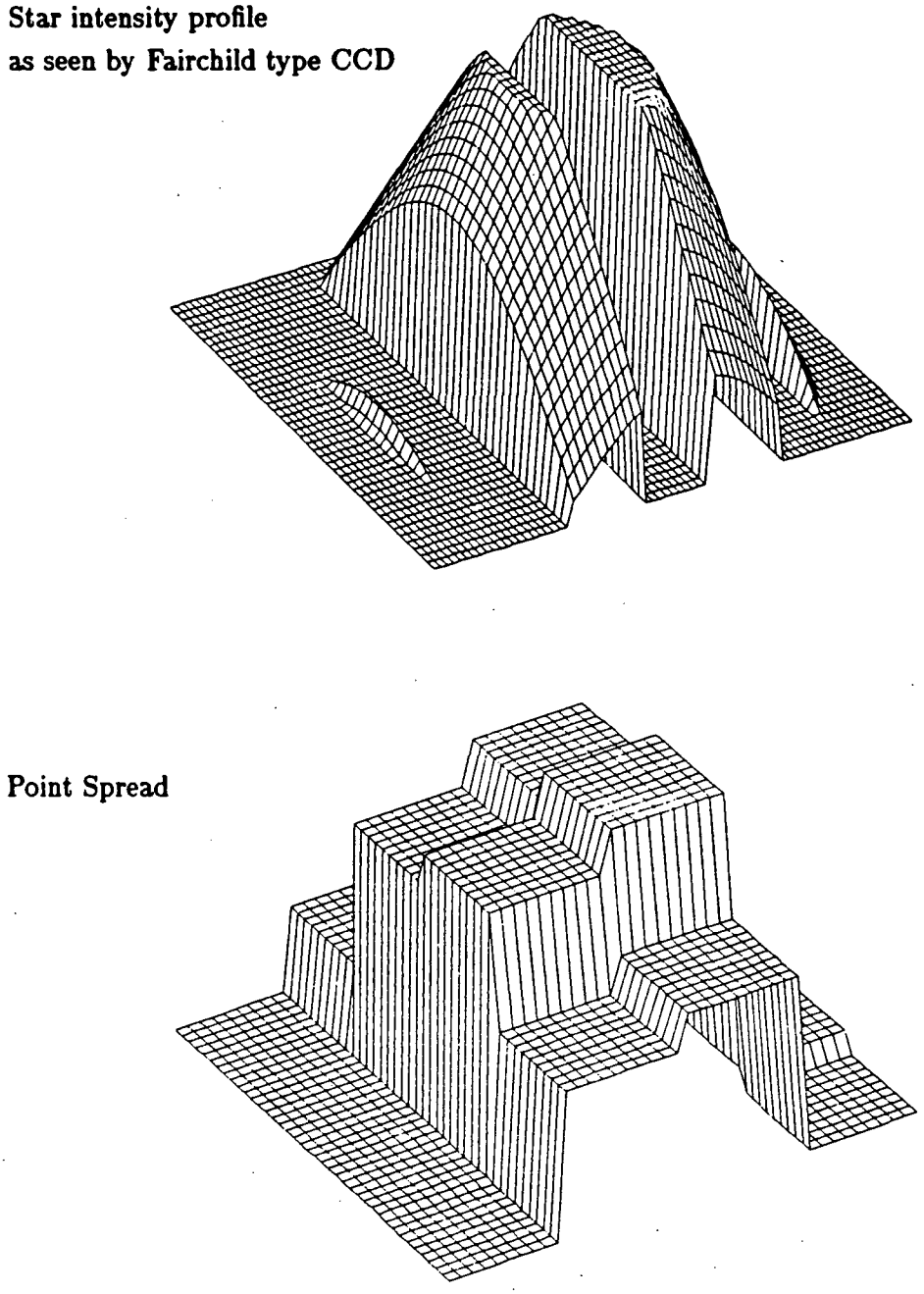

Figure 2–4 Simulated Star image and resulting point spread for the Fairchild 211 CCD

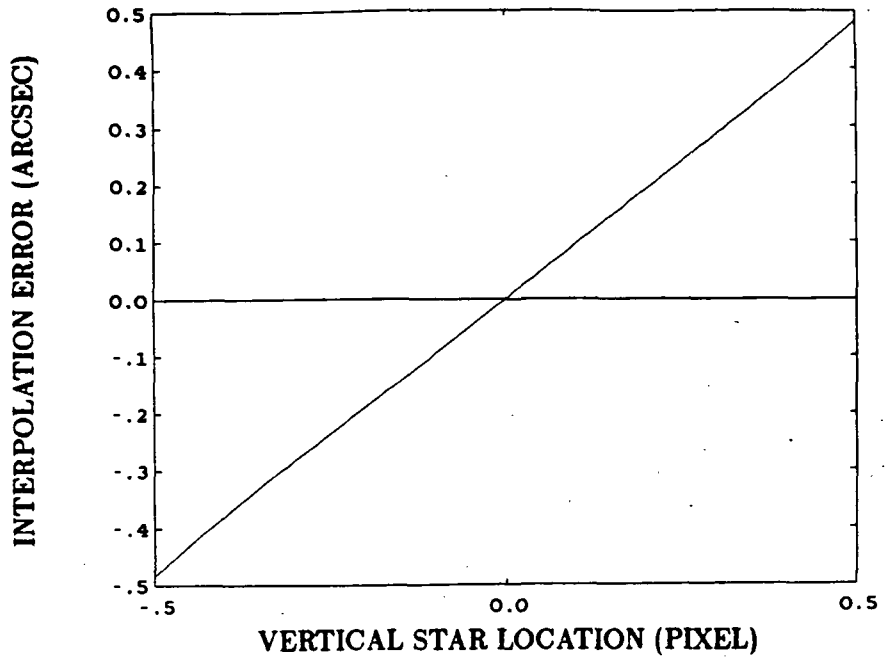

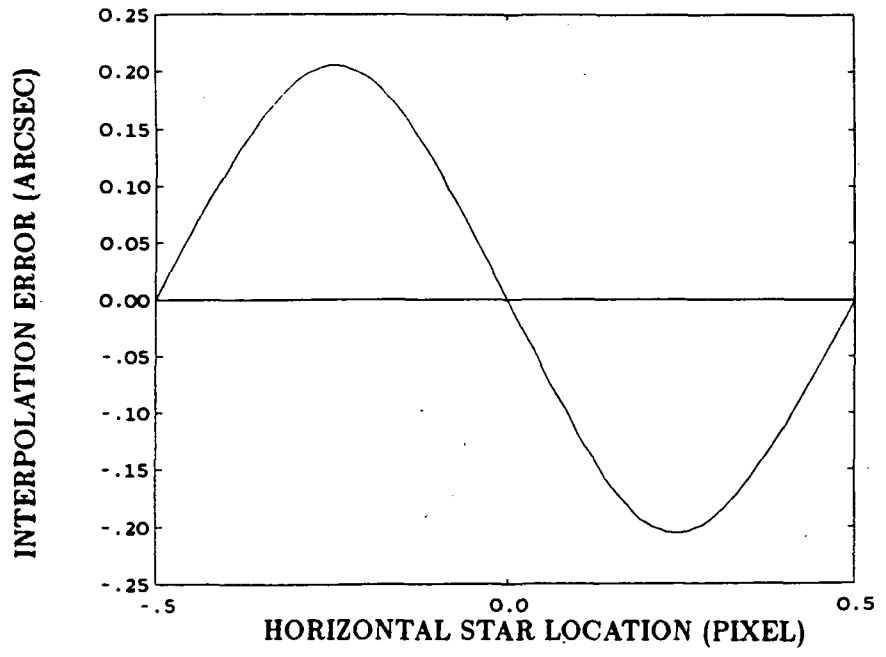

Figure 2–5 Error in calculated position without correction to interpolation equation for the Fairchild 211 CCD

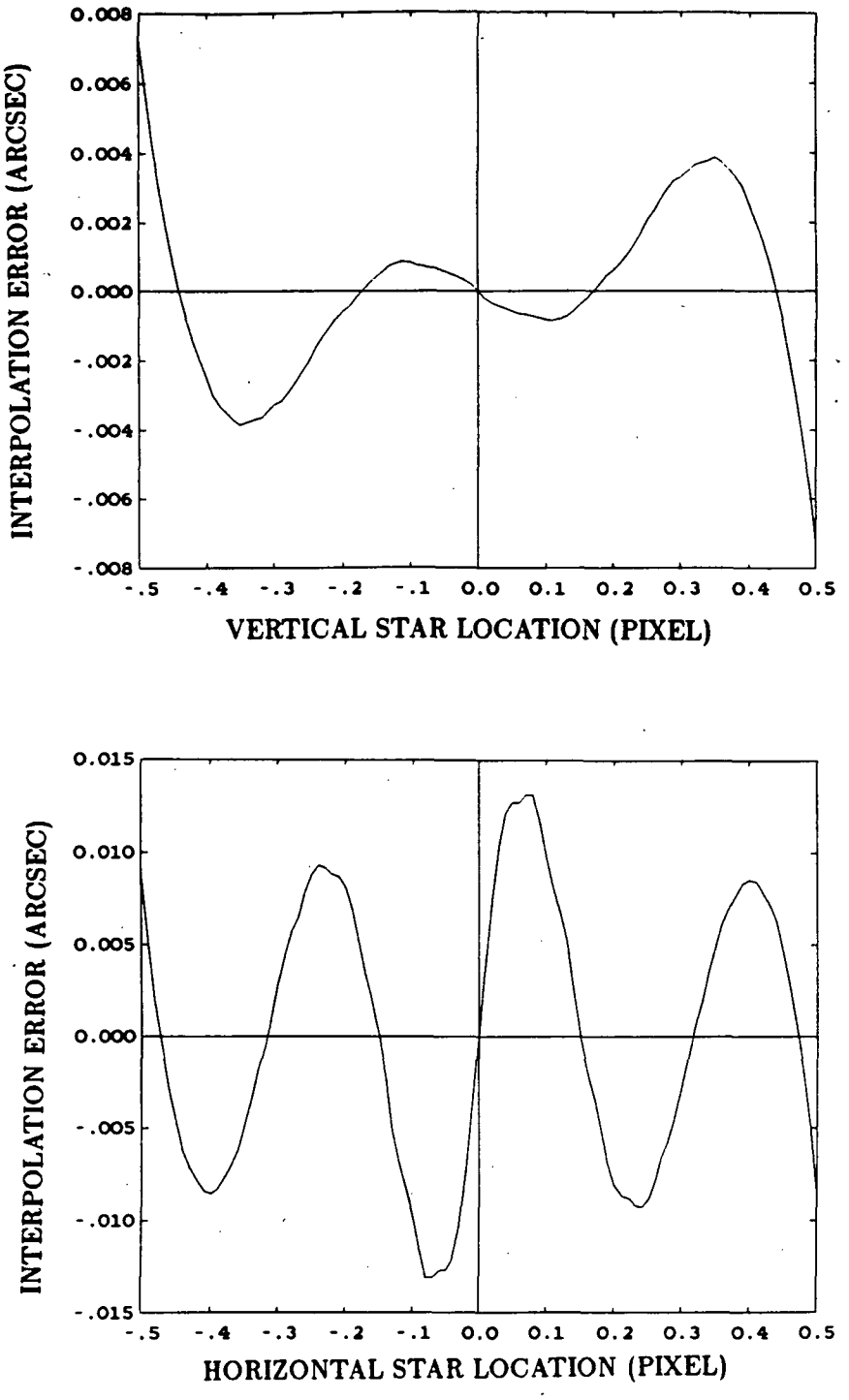

Figure 2–6 Error in calculated position after application of correction factor for the Fairchild 211 CCD

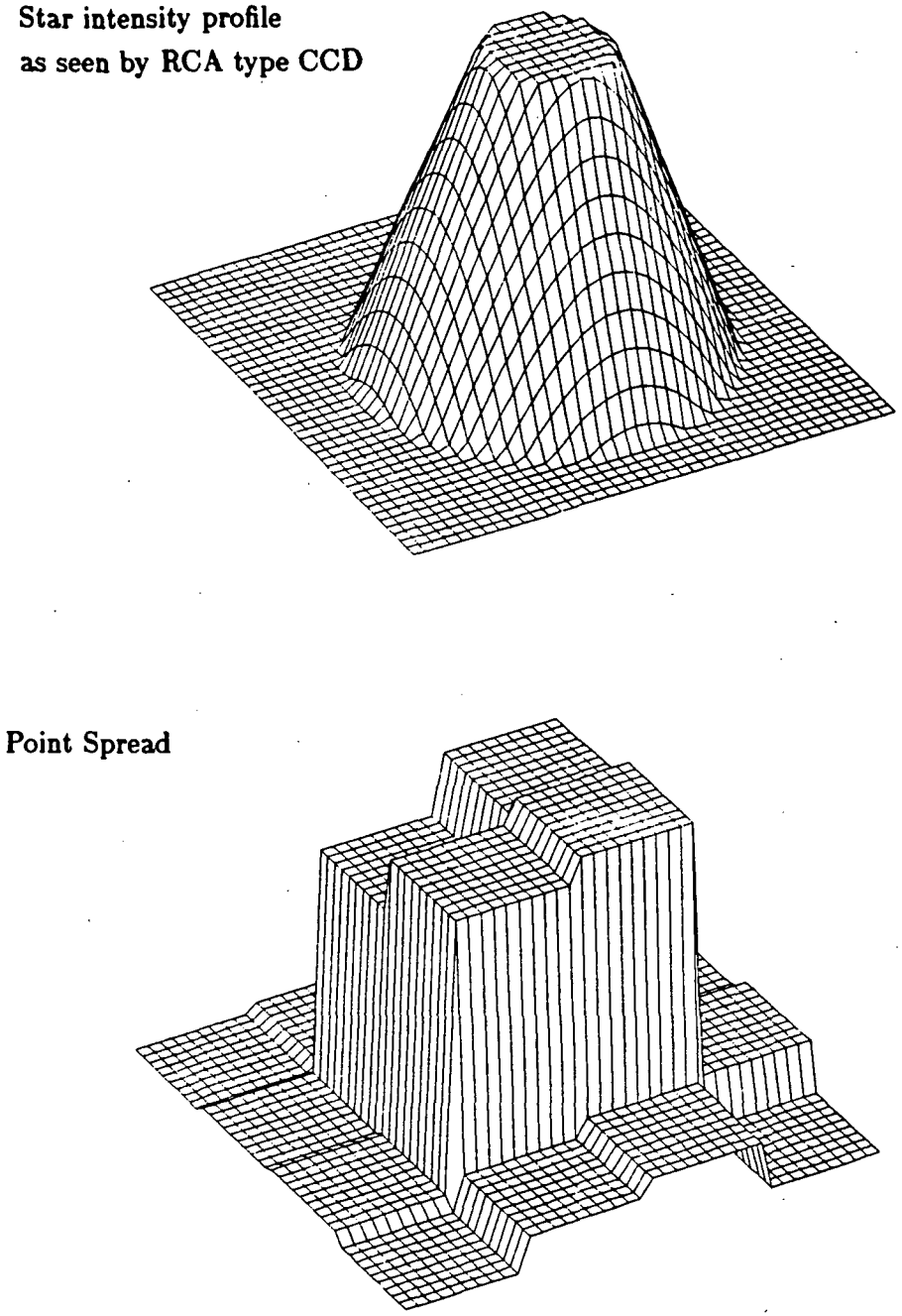

Figure 2–7 Simulated star image and resulting point spread for the RCA 501 CCD

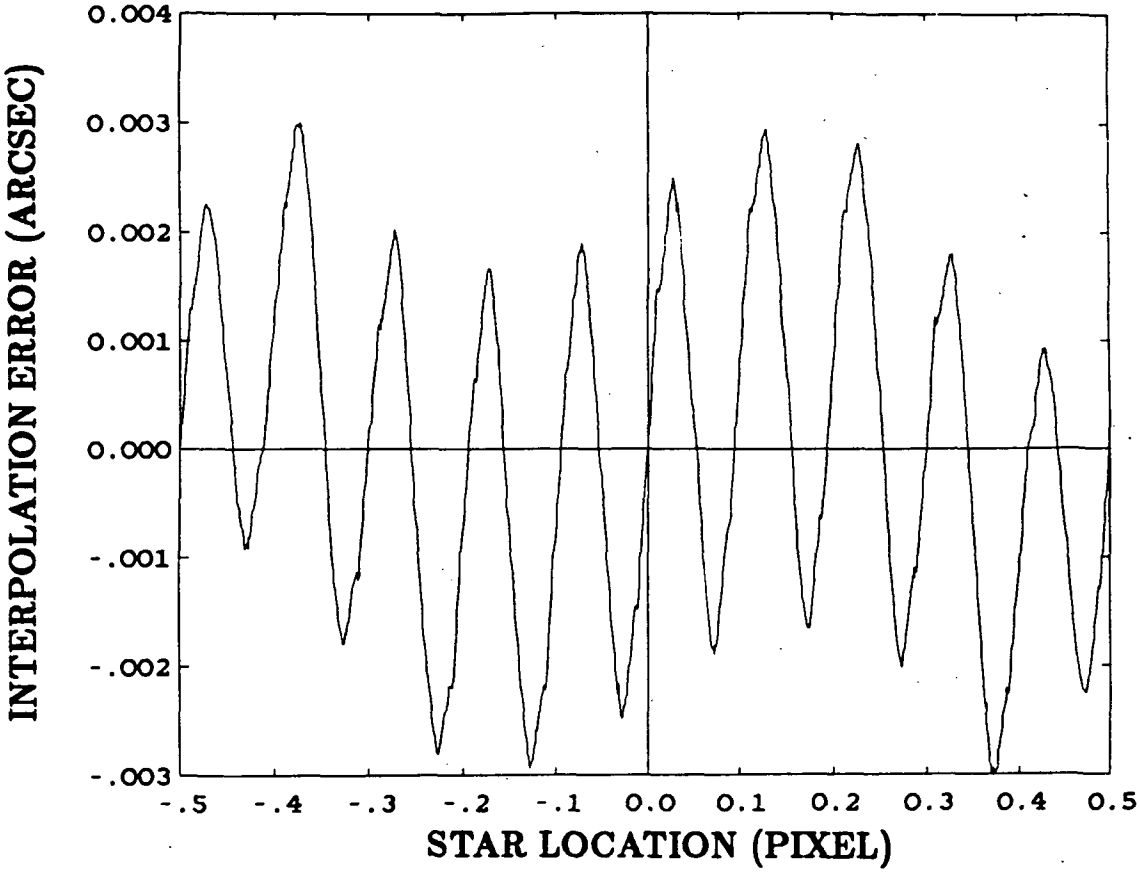

Figure 2–8 Error in calculated position for the RCA 501 CCD

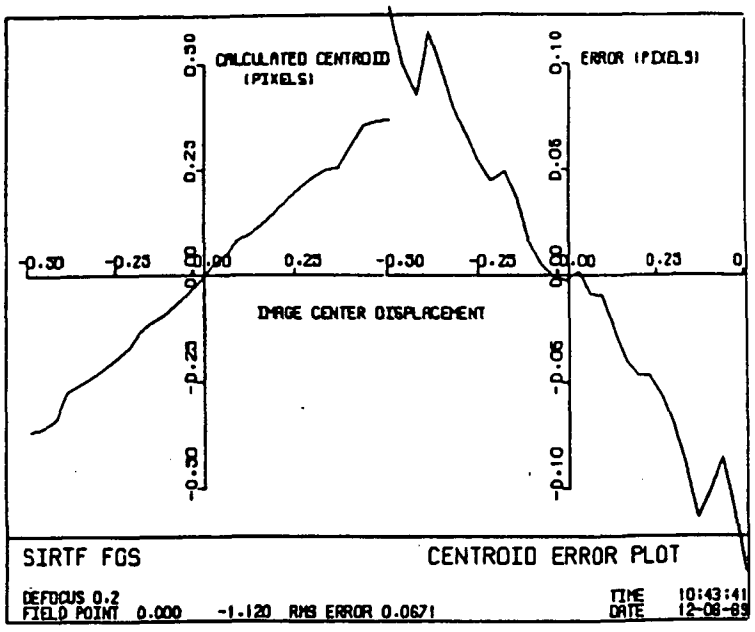

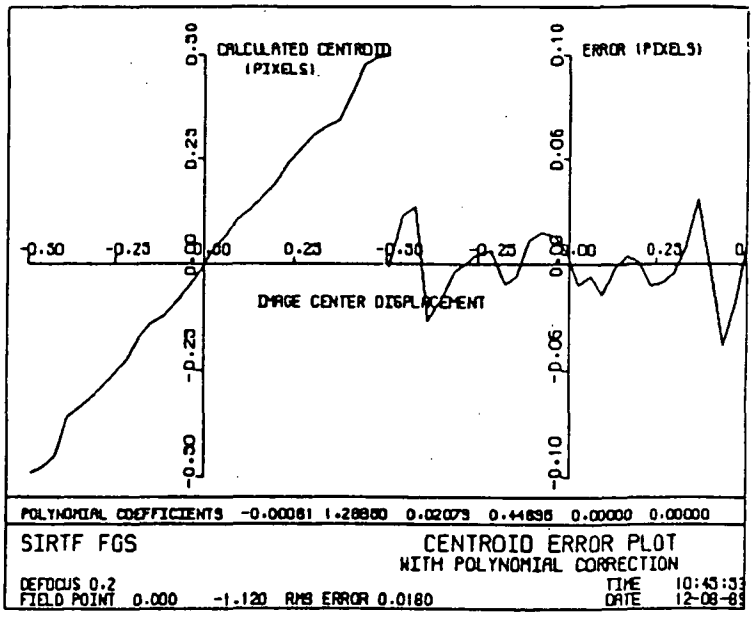

Figure 2–9 Empirical errors in calculated star position before and after polynomial correction for RCA 501 CCD [G&G–1]

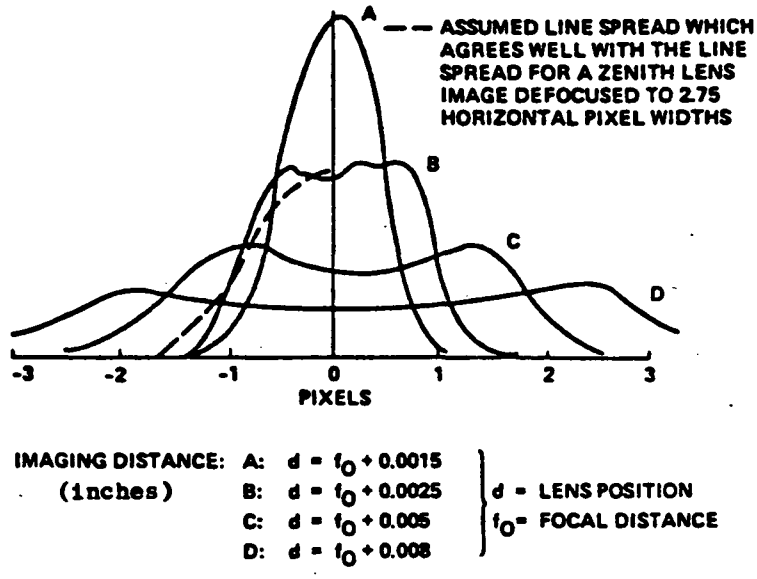

Figure 2–10 Star image shapes resulting from varying optical defocus parameters [PAR–1], [MAR–3]

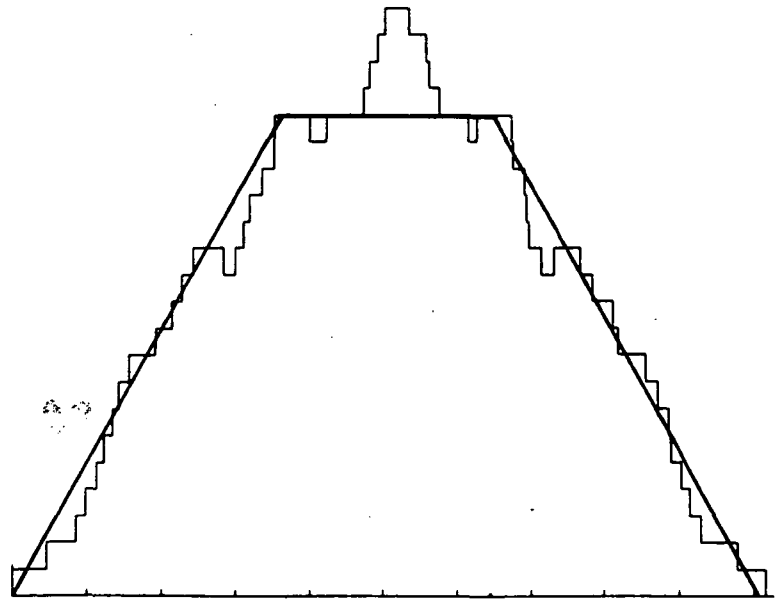

Figure 2–11 Cross-section of Contour Star Image

Chapter 3

Extension to a Moving Image

The goal of SIRTF is the scientific study of both stationary and moving targets. Prior work ([P&P-1], [PAR-1], [LPP-1], [PPL-1]) has developed control laws and established the accuracy that may be expected for the stationary case. The purpose of this work is to examine the effect of a moving target on pointing accuracy. Planets, moons and comets represent types of moving targets of additional interest to space scientists. Consideration of this facet of star sensor performance required the modification of the star signal simulation discussed in Chapter Two. This chapter will describe the problems involved when tracking moving infrared objects, outline the algorithm changes needed to achieve a sensor signal simulation for the moving body and, finally, present the accuracy and limitations of the sensor and interpolation algorithm when used for this application.

The motion—rate and trajectory—of the target is assumed to be a well-known function. The motion of planets, moons and comets will be tabulated by astronomers for the purposes of this project and are assumed to be available to star tracker processing electronics in much the same way as a star ephemeris is available for primary pointing. If the target to be studied with the infrared scientific

instruments also emits radiation in the visible spectrum, the problem of tracking reduces to a fairly straightforward extension of existing control system philosophies [P&P-1]. Acquisition of a target in motion may be a topic of some concern in this case, but should not present major conceptual difficulties over and above those that would exist for the stationary case. Problems may arise, however, when the infrared target cannot be sensed by the visible CCD detectors. For this case, visible guide stars in the vicinity of the target must be used for proper pointing. The moving infrared object must be motionless with respect to the field of view of the scientific instruments, so therefore the image of the guide stars must move across the face of the star sensor in a prescribed fashion corresponding to the motion of the target. The result is that, during a given integration time, the image of the guide stars on the sensor will have shifted with respect to the face of the CCD, resulting in a 'smeared' image. This is demonstrated by the images in Figure 3–1 in which the stationary 'trapezoidal' image is compared to the same image in motion. For a moderate scan rate, the resultant shape is more peaked than the original image. The image resulting from very high scan rates is shown in Figure 3–2, where the contour is no longer peaked, but resembles an elongated 'camel back' and has moved off the edge of the integration area as well. It is important to note that the attitude control system tracks the target in an open loop mode since the control system is actually following a prescribed time history of the moving target. The means and necessity of using the scientific instruments in the control loop to verify the presence of the infrared target in the telescope field of view and to use them as a sensor to provide loop closure has not, as yet, been established.

The shape of the star intensity profile for simulation purposes is taken to be the simple trapezoidal shape described in the previous chapter. However, when smeared across the face of the device, the resulting image profile becomes more

mathematically complex, especially when variations in target rate, intensity and integration time are considered simultaneously. Rather than develop a family of curves to describe the shape geometrically, an approximation was devised. The trapezoidal image was moved across the face of the pixel in increments of 1/100 or 1/1000 of the actual integration time, and integrated at each position. The sum of these intermediary integrations then becomes the total signal for the device. Figure 3–3 shows the effect of the number of intermediate integrations on the characteristics of the error curve for a simple sample case. The curves for 100 and 1000 time steps are negligibly different, but it is clear that the curve for 10 steps is not completely converged.

The angular rate required to track Halley's comet, as specified by the Hubble Space Telescope project [BRO-1], has been established at 0.21 arcseconds per second. This number was used as a baseline for most of the analysis done in this chapter. Additionally, SIRTF Fine Guidance Sensor (FGS) specifications call for the capability to track a 14th magnitude star. Unless otherwise specified, all simulated stars approximated such a dim object.

The graphs that are presented in this section are typical of sensor performance that may be expected, but each is a specific test case, run for a single star magnitude, scan rate, and initial image position with respect to the center of the CCD subarray. The general test scan angle was up and to the right at 30 degrees at the maximum projected rate of 0.21 arcseconds/second. The initial location of the star with respect to the center of the CCD subarray varies from plot to plot, but, unless otherwise noted, is the same for the case of several curves shown on the same graph. Results have been obtained for the case of 3x3, 4x4, and 6x6 pixel subarray sizes. Results for larger arrays can be extrapolated from this data, but

actual computer runs with these large subarrays was not accomplished due to the amount of computer time required.

A fundamental characteristic of the behavior of the interpolation algorithm becomes apparent at this point. The actual position of the star image is at one end of the smeared image at the beginning of the sample period and at the opposite end of the smeared image at the end of the integration period (Figure 3–1). The algorithm, however, finds the centroid of the complete smeared image, which, for a constant target rate, is exactly halfway between the two extremes. For this case, then, the interpolation will yield the actual star position midway through the integration period. The severity and nature of interpolation errors will now be examined in detail using the computer simulation of the CCD performance.

Without some form of correction to the basic interpolation results for the smeared image, the dominant centroid error for a constant rate, linear target motion is simply due to the timing error which is given by:

$$err_{cent} = \frac{T}{2} * \dot{\theta}_c \tag{3.1}$$

where $\dot{\theta}_c$ is the target rate. This result is corroborated by the results of the simulation. Figure 3–4 demonstrates the error that results from a typical image moving at a specified constant rate as the integration time increases. Errors resulting from different target rates are shown, as well as a comparison with the error magnitude that may be expected for a stationary image. As can be seen, the increase in error for a moving target is linear with increasing integration time (or increasing image motion) as predicted after the region of low signal levels is exceeded. The amount of motion that occurs during a sampling period is very small for short integration times so that the magnitude of the error is very close to that calculated for the stationary image. As the distance moved by the target during the integration period

increases beyond the quantization level, the true linear nature of the error becomes apparent.

The SIRTF specification for offset pointing accuracy has been stated as 0.1 arcsecond. Based upon the errors shown in Figure 3–4 this requirement is clearly not met at longer integration times, and only marginally met at lower ones. This unfortunately does not allow a budget for error from other sources. However, since its nature is well-known, this significant error contribution may be easily compensated for. Figure 3–5 shows the result of simply adding the known factor of $\frac{T}{2} * \dot{\theta}_c$ to the centroid estimate of the device based upon the formula given in Chapter 2. This particular graph was generated by using a relatively large 6x6 pixel submatrix. The starting point of the star image with respect to the matrix center was specifically placed in such a way as to ensure that no signal would be lost due to the image straying off the edge of the interpolated area. The error for the corrected image continues to decrease with increasing signal level, unlike the error for a stationary image, which approaches a constant value. This is due to the increased spread of the signal over a larger number of pixels, which makes the centroid equation (2.7) more sensitive. The slight irregularities are due to the fact that since these error levels are now quite small, quantization effects at even large signal levels exist in sufficient magnitude to produce an noticeable irregularity. If the truncation of the individual pixel element signals is removed, the curve becomes smooth, but still decreases at slower integration rates. At any rate, this simple addition brings the accuracy of the interpolation process to within the cited specifications and is, before the consideration of noise effects, an improvement over the error levels obtained for a stationary image.

There is another limitation to the accuracy of this method for the tracking of

moving targets, however. Position errors increase dramatically when any signal is lost due to the edge of the image leaving the selected pixel subarray. Figure 3–6 demonstrates this effect by comparing the corrected signal to the uncorrected signal for an image moving across a 4x4 subarray. At an integration time of about one second or so, the corrected error curve increases in correspondence with this loss of signal. The time step at which the image starts leaving the edge of the array is quite naturally highly dependent upon the starting point of the image with respect to the array center. The methods of avoiding this problem are simple: either move to increasingly larger subarrays for moving target tracking, or develop a very precise target acquisition scheme which ensures that the image will remain on the subarray during the integration period.

A large subarray, however, takes longer for the processing electronics to read, which in turn limits the data rate at which the device may be sampled. Larger arrays also have a negative effect on noise levels, as will be seen in Chapter Four. One compromise is to 'stretch' the dimension of the array in the predominate direction of motion. In other words, if the projected image motion is up and to the right at 30 degrees, then increasing the width of a 4x4 array to six pixels will maintain more of the signal with less of the related problems listed above. A test case for this premise is shown in Figure 3–7. In using a non–square array, the integration time step at which the error increases due to signal loss is improved from about one second to ten seconds. In this way most of the advantage gained by going to the 6x6 array is available in the 4x6 array with only a 50% increase in the number of pixels.

Obviously, the correction scheme as outlined breaks down if the a priori knowledge of target motion is inaccurate. Motion has been very carefully assumed to be linear for all results thus far, and errors are certainly introduced if the assumed

scan rate is incorrect, scan angle is off, or motion is nonlinear.

The errors due to uncertainty in scan rate alone are expected to be linear with integration time, much as the original correction factor was linear. The issue of importance is, naturally, the strength with which small errors in known motion affect the centroid error. Figure 3–8 demonstrates these errors for a 6x6 array, with the same specific starting point relative to the array center as in Figure 3–5 so that no signal loss occurs. Results are shown for varying levels of accuracy of the known scan rate, such that the 1% curve corresponds to the error that would result if there was 1% difference between the actual scan rate and the scan rate applied as a correction factor. As expected, the increase in error for each has a linear trend. An error of 1% in image rate does, however, maintain centroid error levels below 0.01 arcsec in general and to a level of .001 arcsecond for a 1 second baseline integration time. The effect of uncertainty in knowledge of the image motion angle is shown in Figure 3–9. This curve was produced by specifying the scan angle in a direction upward and to the right. This angle was set to 30 degrees for use in the motion error correction terms, while the actual scan rate varied by 0.3 and 0.03 degrees from this nominal value. As with linear motion rate uncertainty, errors do not become significant until long integration times are reached. The overall effect of this uncertainty is less than the previous case, however.

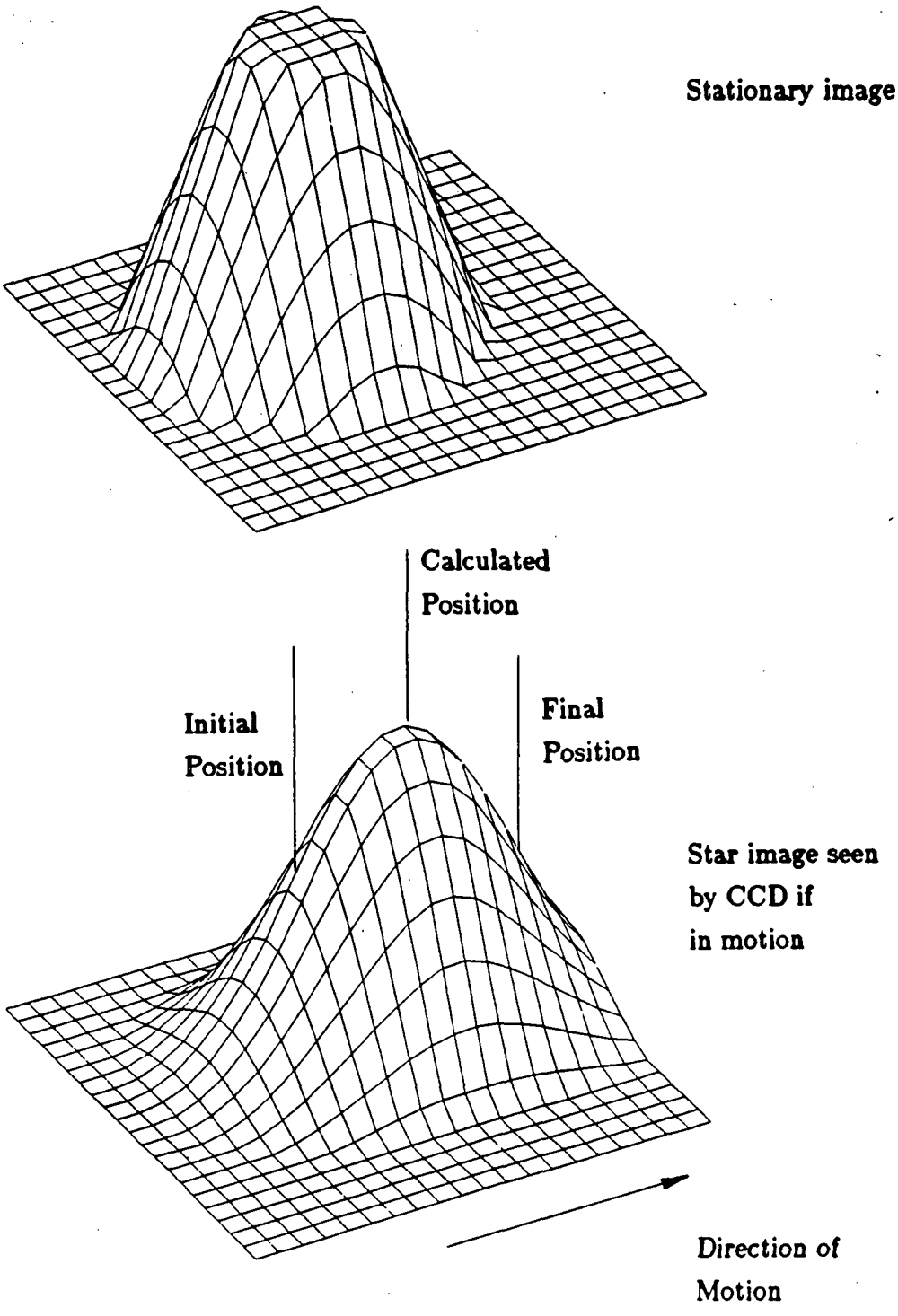

Figure 3–1 Effect of target motion on image shape as seen by the RCA 501 CCD (moderate scan rate)

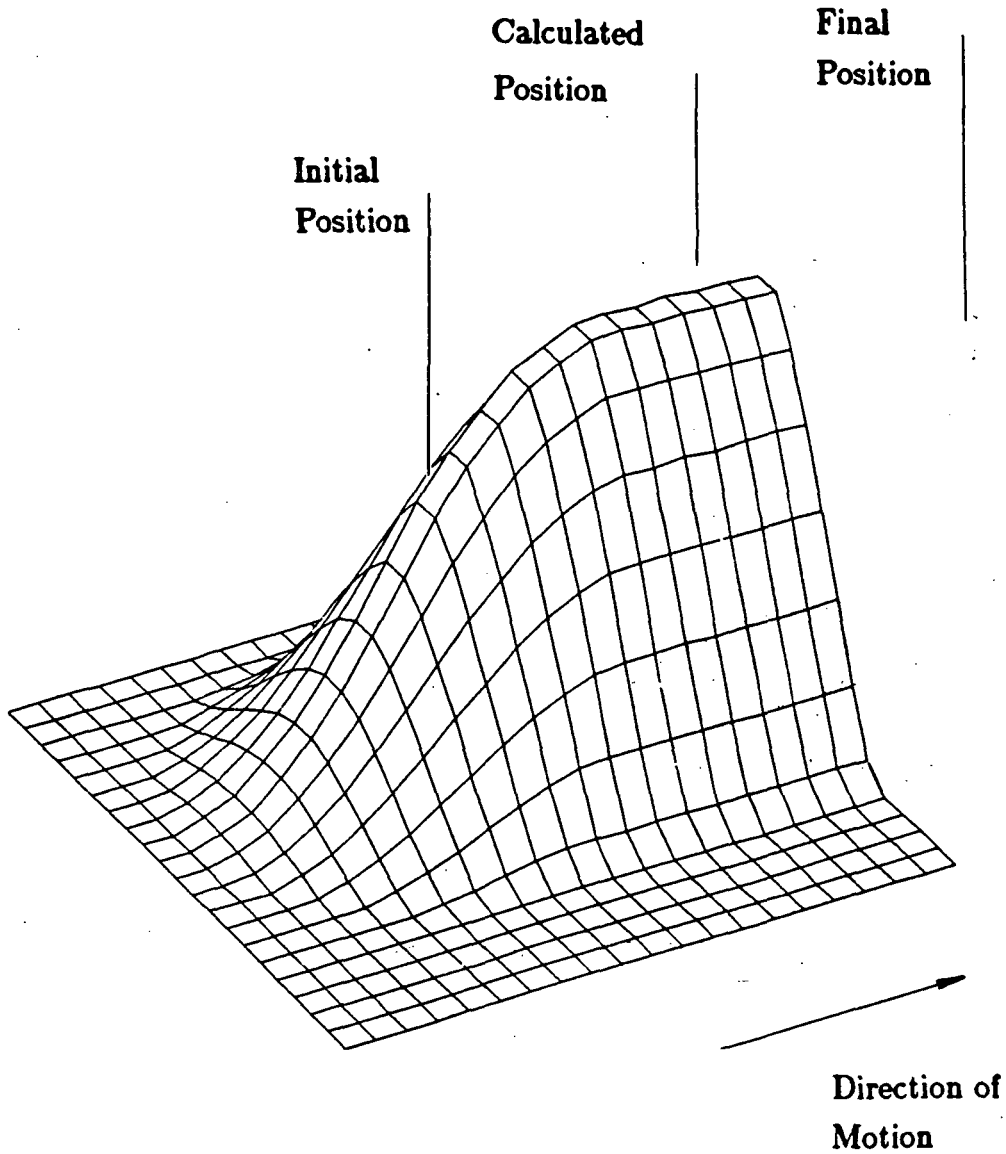

Figure 3–2 Effect of target motion on image shape as seen by the RCA 501 CCD (very high scan rate)

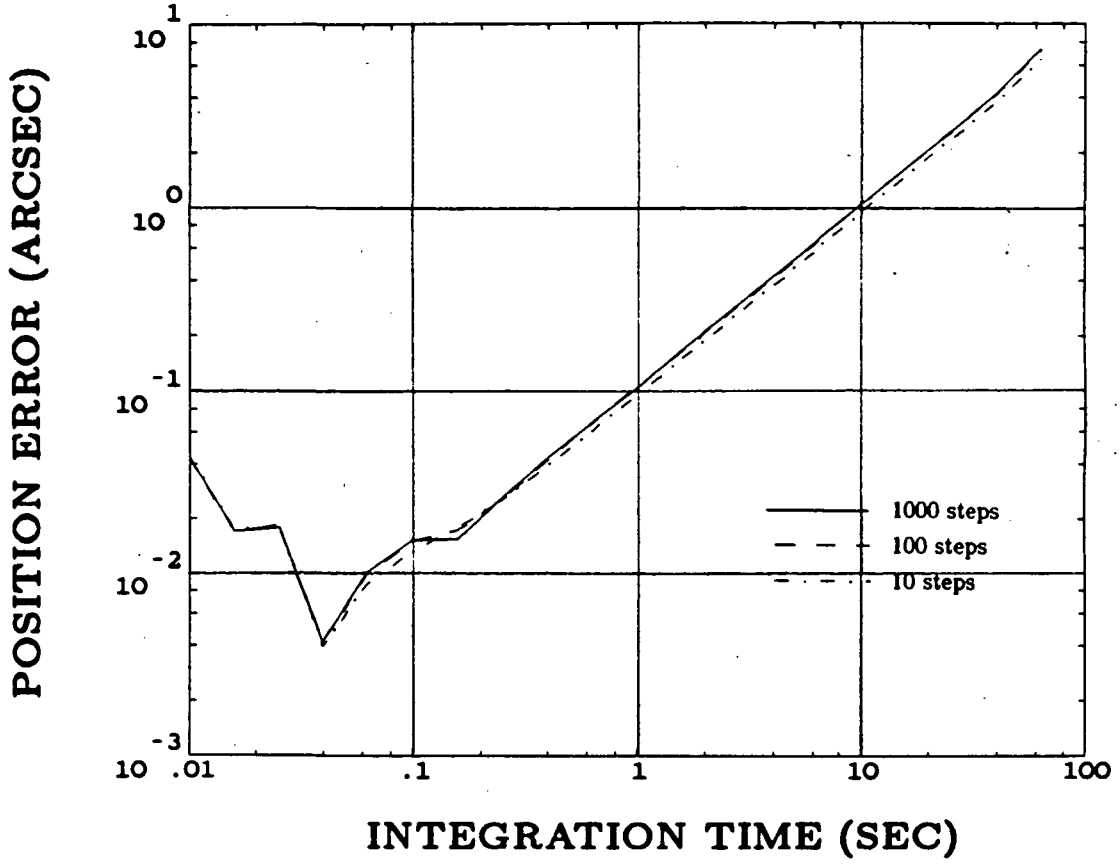

Figure 3–3 Effect of number of intermediate integrations of a moving target on centroid error

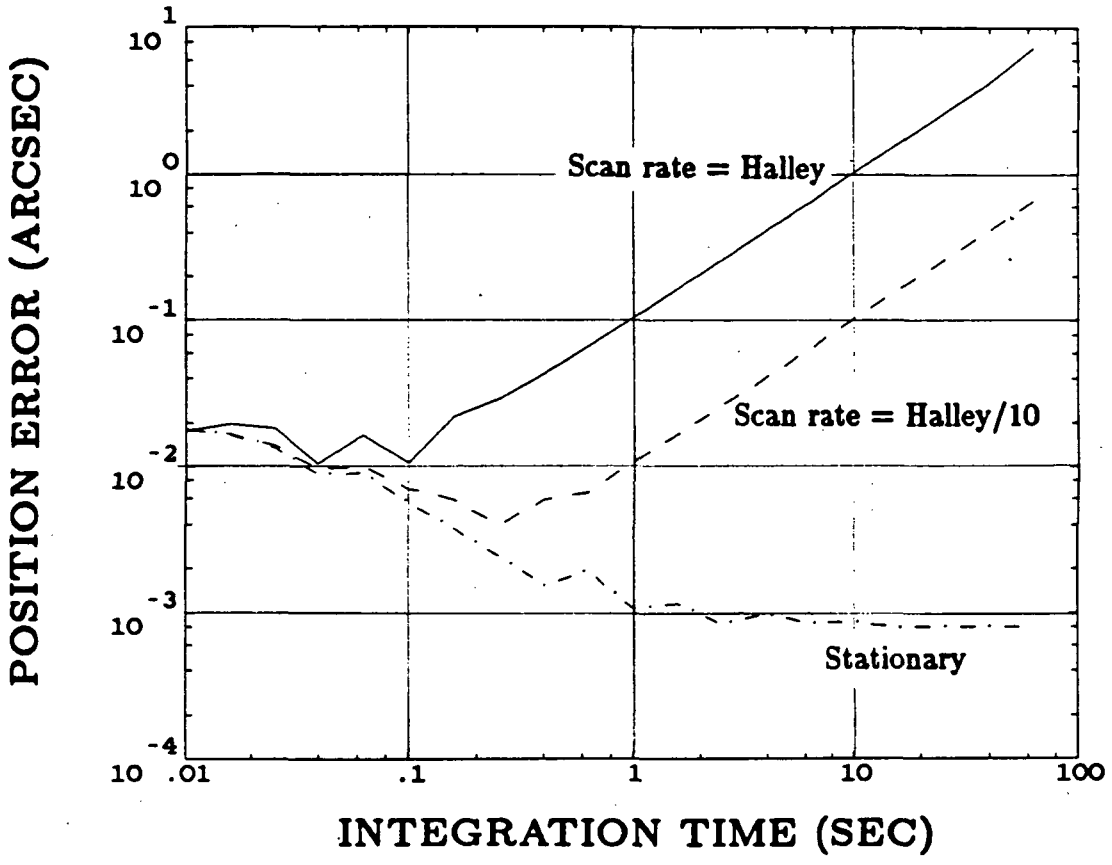

Figure 3–4 Centroid errors resulting from target motion
Halley's comet rate = 0.21 arcsecond/second

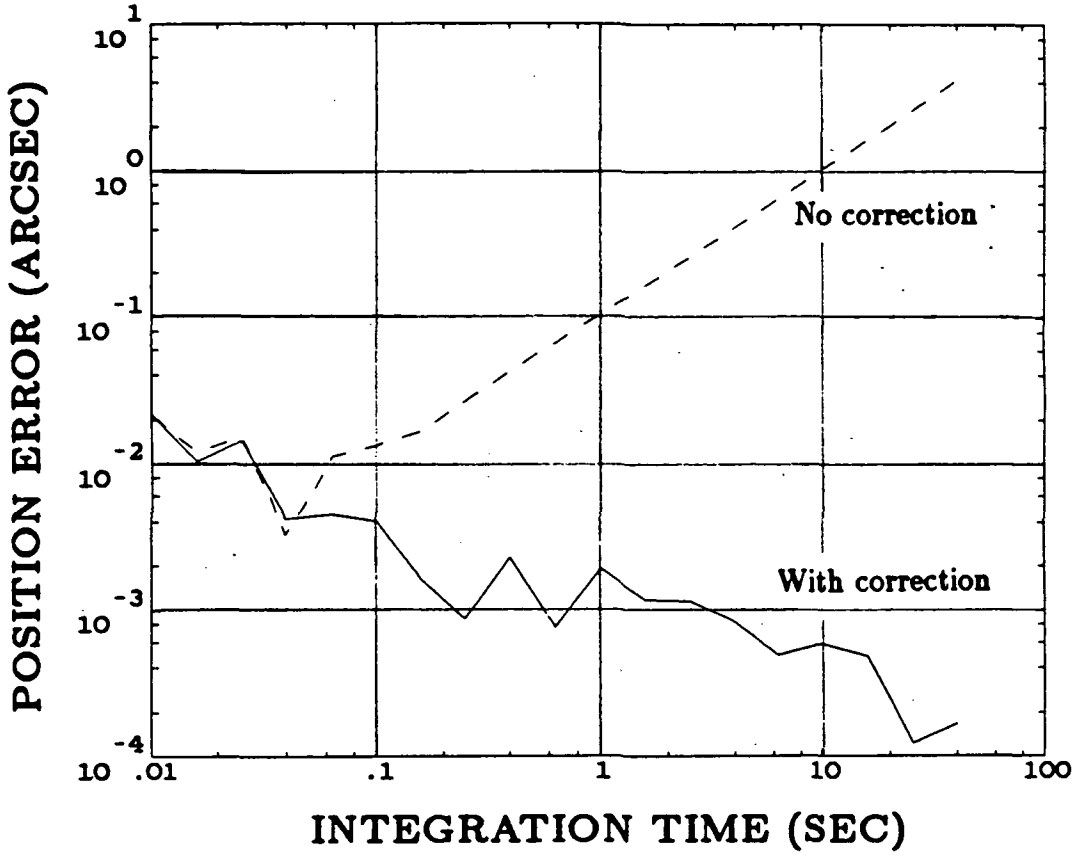

Figure 3–5 Effect of addition of correction term $\frac{T}{2}\dot{\theta}_c$ on centroid error for a 6x6 pixel subarray

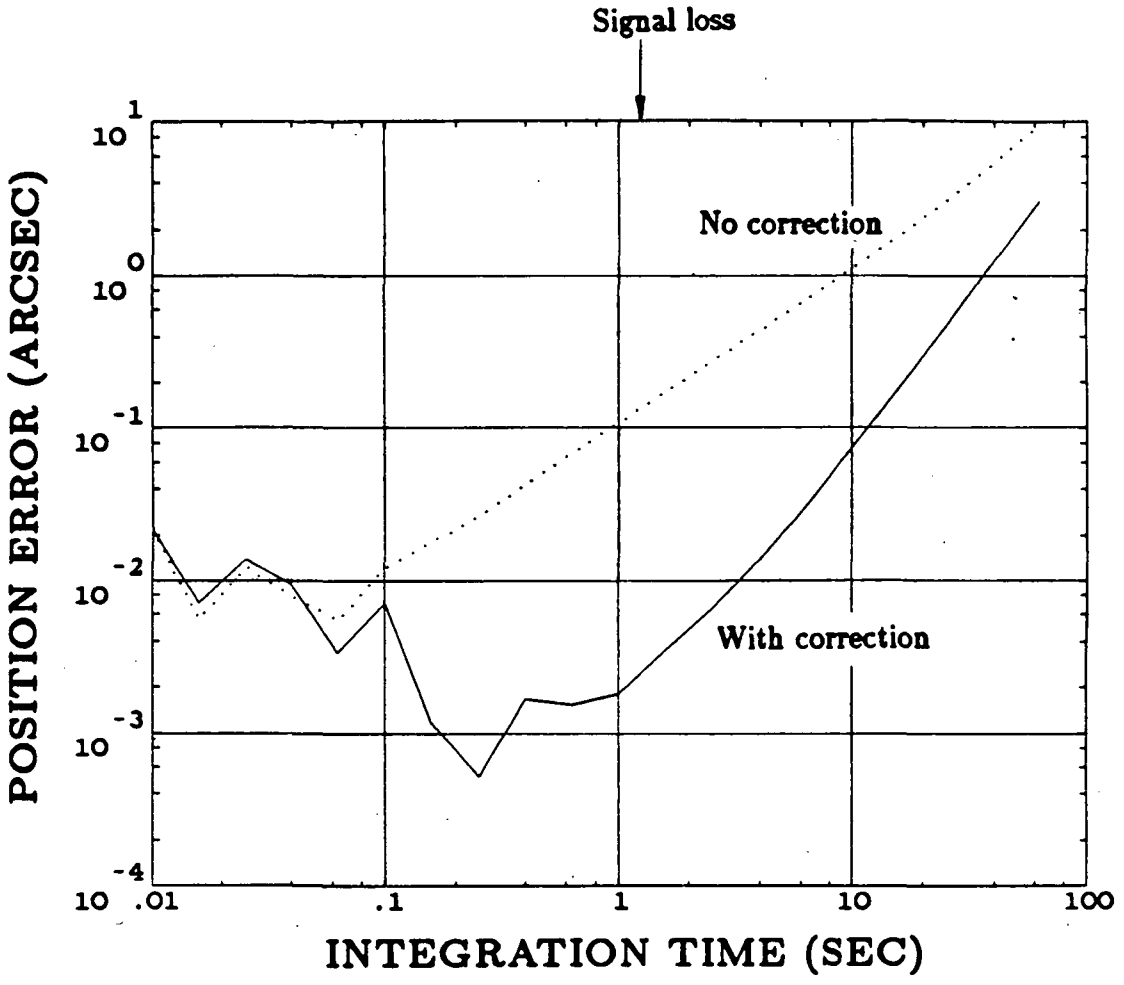

Figure 3–6 Effect of signal loss upon postion error for a 4x4 pixel subarray

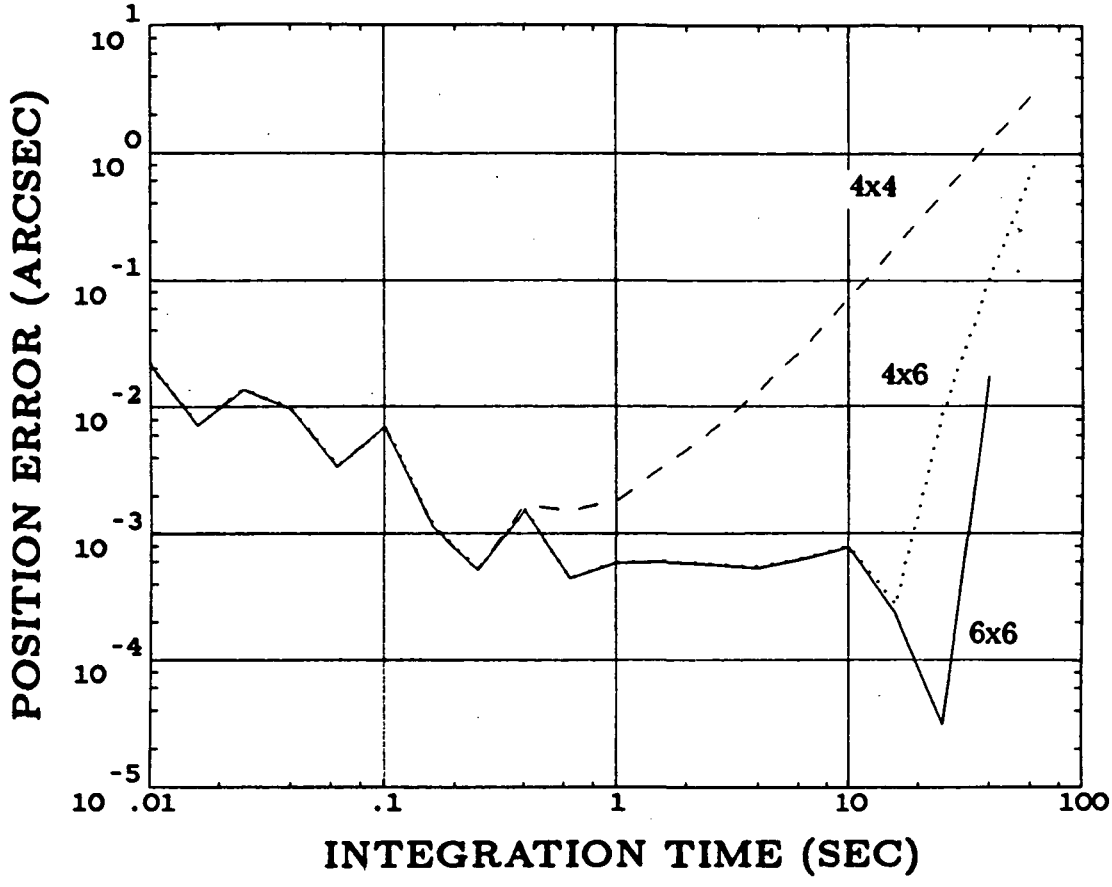

Figure 3–7 Impact of subarray dimension size upon magnitude of error due to signal loss

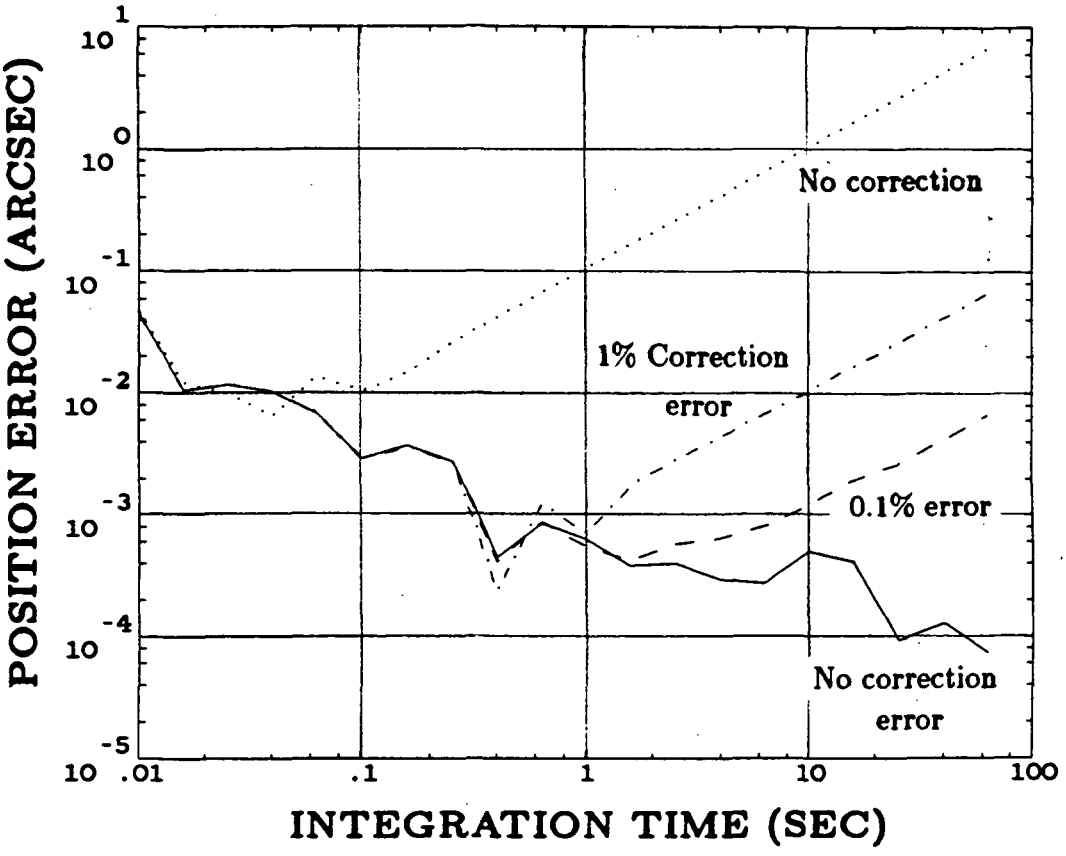

Figure 3–8 Error increase due to imperfect knowledge of scan rate

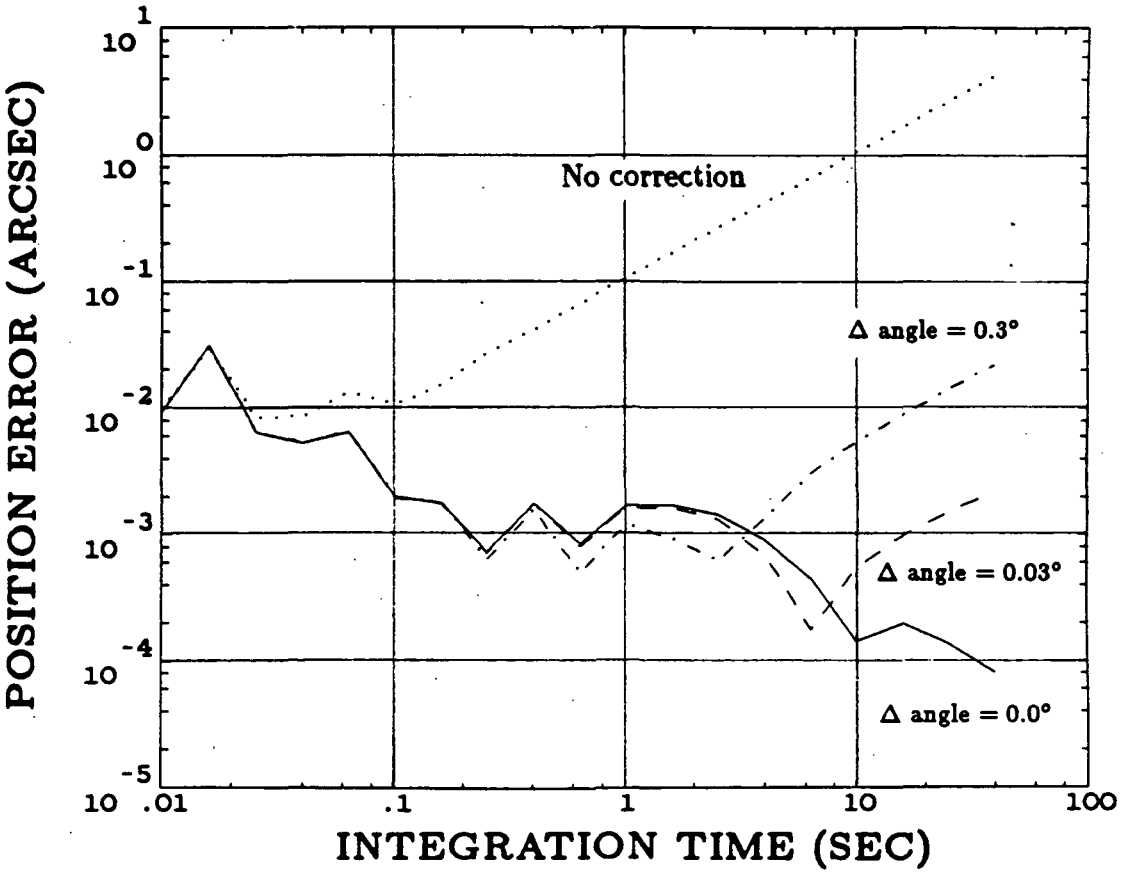

Figure 3–9 Error increase due to imperfect knowledge of image motion angle

Chapter 4

Noise Analyses

The star sensor simulations accomplished in Chapters Two and Three have neglected the contributing effects of sensor noise. Noise contributions include effects from the CCD itself, as well as consideration of the satellite attitude determination system which includes the gyro package necessary for short term stabilization. This chapter summarizes the important characteristics of each for the purpose of later integration into a Kalman filter.

§4.1 Star Sensor Noise

Many different factors contribute to the noise inherent in the CCD output. Effects due to manufacturing imperfections are not easily modelled for the general case. These imperfections vary from device to device and, as such, need correction factors based upon the discrepancies found in the individual instrument. These corrections are therefore a function of star position on the complete 320x512 array. This work, as mentioned in Chapter Two, is being accomplished by JPL, and is, in essence, more of an error source than a noise source. Noise effects, as referred to in this chapter, pertain to statistical uncertainties, which, for the CCD, include photon, or shot noise, dark current and background noise.

The analyses in previous chapters have assumed that the CCD signal was deterministic for purposes of establishing performance limits. Input photon noise, otherwise known as shot noise, arises from the fact that photon emission from a generating source is actually a random process [B&L–1]. Thus, the number of photons accumulated on a pixel during an integration period is a random variable. The standard deviation of the number of photoelectrons collected in the potential well is the photon noise. Photon emission from a source statistically follows a Poisson process, which means that the standard deviation of the number of photons is equal to the square root of the mean signal gathered, or

$$n_{en} = \sqrt{S_{ij}} \tag{4.1}$$

for a single pixel. This effect is most significant for sources of low strength, ie, dim stars.

Thermal radiation tends to generate white noise and therefore the production of dark current effects. The basic process of charge accumulation on a pixel entails electrons receiving energy from photons and making a transition from one energy state to another. It is therefore apparent that electrons can make the same jump by the absorption of thermal energy. Dark current is then a function of chip temperature and can be effectively lessened by cooling the device. The amount of cooling, however, is limited by the amount of supporting circuitry which surrounds the device and naturally generates heat. Since the FGS sensor for SIRTF is operated at very low temperatures (about 150K) due to the presence of telescope cryogenics, the dark current contribution of 1 electron per minute per pixel is taken to be negligible when compared to other noise sources [GGS–1].

Detector read noise, or background noise, makes a significant contribution to the overall noise levels. The term 'read noise' is used widely in the JPL–

based literature and is a combination of charge transfer noise and processing noise. Though individual contributions to total background noise are not broken out separately, the RCA CCD has a manufacturer–quoted 'read' noise of 80 electrons [GGS–1], while a bread board test of the device demonstrated a noise level of 98 electrons [G&G–1]. This latter, more conservative value is to be used in all simulations for this chapter.

Charge transfer noise emanates from two basic mechanisms: charge transfer inefficiency and fast interface states [B&L–1]. Noise from fast interface states originates from small flucuations in the total number of photoelectrons trapped at any given instant. Transfer noise due to imperfect efficiency results from random fluctuations in the charge transferred from one potential well to another. For a pixel carrying S_{ij} photocarriers, ϵS_{ij} photocarriers will remain after the transfer occurs, where ϵ is some small number. Thus there is a shot noise of mean square value ϵS_{ij} associated for each transfer from a particular pixel. In addition, this noise will be introduced into each charge packet as it arrives and leaves a potential well, so the mean square noise becomes $2\epsilon S_{ij}$. If ϵ is a constant, then the noise contribution due to charge transfer inefficiency is

$$n_{ct} = \sqrt{2\epsilon S_{ij}} \tag{4.2}$$

Typical values for ϵ are in the neighborhood of 1×10^{-4} [B&L–1].

The other contribution to background noise, process noise, is not negligible. It varies with the signal processing electronics and combines with charge transfer noise to build the overall background noise level to its demonstrated level of 98 electrons.

Leaving the background noise as a constant, then the noise level in each pixel carries an rms value of

$$n_{ij} = \left[n_b^2 + n_{sn}^2\right]^{\frac{1}{2}} \tag{4.4}$$

where n_b is the rms background noise level and n_{sn} is the contribution due to shot noise. Since $n_{sn} = \sqrt{S_{ij}}$, then

$$n_{ij} = \left[n_b^2 + S_{ij}\right]^{\frac{1}{2}} \tag{4.5}$$

The numerator and denominator of the interpolation formula (Equation 2–7) are both affected by the pixel noise content, so the total noise in centroid position is nonlinear with the individual pixel noises. A satisfactory linearization is given by Parsons [PAR–1] which has been slightly expanded and clarified for presentation here.

Linearization via a small–signal approximation of the nonlinear combinations of noise contributions in the centroid equation is justified when the overall signal to noise level is large. For a full well of 390,000 electrons, the shot noise component of 625 electrons and the background noise component of 98 electrons combine to yield a representative signal to noise ratio of $\approx$ 616, which should certainly be adequate for justification fot the use of small signal approximations. So, if $\tilde{k}_i$ is the approximate position uncertainty due to the noise in the ith line spread, then the uncertainty for small perturbations $\tilde{S}_i$ from the ith line spread near value $\bar{S}_i$ is

$$\tilde{k}_i \approx \left.\frac{\partial k'}{\partial S_i}\right|_{S_i=\bar{S}_i} \tilde{S}_i \tag{4.6}$$

and the line spread variances for uncorrelated individual pixel noise levels are given by

$$\tilde{S}_i = \sum_{j=1}^{n_p} n_{ij}^2 \tag{4.7}$$

The total rms centroid error is then

$$\tilde{k}_i = \left(\sum_{i=1}^{n_p} \tilde{k}_i^2\right)^{\frac{1}{2}} \tag{4.8}$$

$$= \left\{\sum_{i=1}^{n_p}\left[\left(\frac{\partial k'}{\partial S_i}\Big|_{S_i=S_i}\right)^2 \sum_{j=1}^{n_p} n_{ij}^2\right]\right\}^{\frac{1}{2}} \tag{4.9}$$

These equations may be manipulated to prove that centroid uncertainty decreases with increasing signal levels. This can be done by consideration of the term

$$\left(\frac{\partial k'}{\partial S_i}\right) = \left\{\frac{[i - \frac{n_p+1}{2}]}{S} - \frac{\bar{S}}{S^2}\right\}^2 \tag{4.10}$$

in addition,

$$\sum_{j=1}^{n}(n_{ij})^2 = n_p(98)^2 + S_i \tag{4.11}$$

so, the uncertainty, or jitter, due to the ith line spread is

$$\tilde{k}_i^2 = \left[i - \frac{n_p+1}{2} - \frac{\bar{S}}{S^2}\right]^2 \left[\frac{n_p(98)^2}{S} + \frac{S_i}{S}\right]\frac{1}{S} \tag{4.12}$$

which implies that larger total signals, S, reduce uncertainty. Therefore, the best integration time for a given star would be that which brings pixel signal levels close to the full well value.

These equations are easily implemented into a computer routine that augments the simulation algorithm previously discussed. Modifications were made to the original routine developed by Parsons to admit other CCD configurations and subarray sizes, including those that are not square.

It useful to examine the jitter levels that exist for a stationary target and then contrast them with those that arise for the moving target based upon this noise

model. Figure 4–1 shows a plot for a stationary image and, most importantly, contrasts the level of jitter present when using a 4x4 array versus a 6x6 array. The jitter level increases with increasing star magnitude, which is a reflection, in general, of signal to noise ratio. For a baseline integration time of one second, the jitter level for a 14th magnitude star on a 6x6 subarray is greater than one arcsecond, when specifications require an overall level of .125 arcsecond. The corresponding centroid noise level for the 4x4 array is about 0.2 arcsecond. It is clear that the smaller the subarray, the better the centroid jitter levels. A 3x3 subarray is required to bring the noise to within specified levels (Figure 4–2). The hypothesis that jitter decreases with increasing signal level is also confirmed by the negative slope of the graphs.

The overall jitter levels are somewhat higher than those presented by Parsons ([PAR–1)] but very close in magnitude to those presented by Goss, et al ([GGS–1]). Two elements underlie this effect. The results presented by Parsons include only the horizontal component of position jitter, whereas the plots presented here give the results for the combination of vertical and horizontal jitter. In addition, the previous studies used a fairly optimistic value of 50 electrons for the background noise level.

Centroid jitter levels are relatively unaffected by the presence of image motion, Figure 4–2 compares the centroid jitter resulting from a stationary object with that of a target in motion on a 3x3 array and contrasts this with corresponding plots of the inverse of total signal level. The small array was chosen here for maximum effect. The noise levels for the two cases are indistinguishable at higher sampling rates, but a noticeable spread begins to occur after a time period of about 1 second. The slope of the curve corresponding to the moving target then begins to shallow. This is another effect of the loss of signal that occurs when the image moves from

the integrated area of the array. As the centroid jitter is proportional to signal level, the loss of signal results in a decrease in negative slope of the curve. There is a direct correspondence between the decrease in slope of the inverse of the total signal level curve and the noise level curve. If no signal is lost, no more centroid jitter is developed for a moving target than for a stationary one.

A comparison of the overall centroid noise levels for a moving target on 3x3, 4x4 and 6x6 arrays is shown in Figure 4–3. These are the noise levels that accompany the interpolation errors depicted in Figure 3–8 and therefore all have some signal loss at longer integration times. As can be seen, the effect of the loss in signal is most noticeable for the 3x3 array, while the noise for the 6x6 array is almost identical to that for the stationary case.

The special case of the 4x6 nonsquare subarray is compared for the moving case in Figure 4–4. The 4x6 subarray is seen to be a compromise in noise level over the 6x6 case ,just as a similar 3x4 array would be over the 4x4 case. This could be implemented in the system software so that the optimum array size would be selected based upon estimated image starting position and trajectory.

The desired NEA, or noise equivalent angle, for the system has been quoted as .125 arcsecond. This is difficult to meet for the combination of low integration times and dim stars. The data does suggest strongly that the smallest possible subarray that can be used without significant data loss is preferable. It is important to remember, however, that for the general case more than one star will be used for pointing, and an estimation scheme based upon a combination of star tracker measurements and known relative star positions should be able to bring the level down.

§4.2 Gyroscopic noise Analysis

Previous studies [PAR-1, P&P-1] have assumed that conventional floated gyroscopes were to be used for attitude determination. Models for these gyros were combined with a model of the star tracker previously described for estimation of telescope attitude with respect to the stars. Developments in gyroscope technology have led to the proposal of the NASA DRIRU–II gyro assembly for use onboard SIRTF. As this package is based upon the Teledyne SDG–5 dry–tuned gyro, as opposed to more conventional floated designs, its noise characteristics need to be evaluated.

The pathology of the dry–tuned gyro is well–described in the existing literature ([DON–1], [CRA–1], and others). There are many differences between the dry–tuned gyro presented in Figure 4–5 and conventional floated gyros. The theory of operation for this device is based on the premise that dynamic reaction torques produced in the universal–joint suspension can be used to produce negligible torsional coupling between the rotor and the gyro housing. The suspension must therefore be precisely mechanically tuned for a resonant frequency equalling the spin speed of 100 Hz. This type of suspension also provides a very high degree of translational support. The manufacturer of this device cites higher reliability, decreased sensitivity to temperature gradients and reduced power requirements over standard gyros. In addition, due to the decoupling of the suspension system, quality of the bearing support is not as critical as in floated gyros. The detailed equations of motion are derived at length in [CRA–1].

The NASA DRIRU–II (Dry Rotor Inertial Reference Unit II) package uses three SDG–5 gyros for a base instrument (Figure 4–6). Each individual gyro with its accompanying electronics comprises a "gyro channel" which provides two axes of information on angular rate independent from the other two channels, hence

providing redundancy [I&R–1]. Table 4–1 lists the operating specifications for this device.

Table 4–1

DRIRU-II Operating Specifications

PARAMETER	VALUE			
	LOW MODE	HIGH MODE	ABSOLUTE	STABILITY
INPUT RATES (DEG/SEC) A. SURVIVAL B. TRANSITION C. PERFORMANCE			600 (20 MINUTES) 2 1.6	
CROSS AXIS COUPLING	X	X	1% (TO 1 HZ) 2% (TO 7 HZ)	± 0.005% 30 DAY LOW RATE ONLY
INCREMENTAL ANGLE OUTPUT				
SCALE FACTOR (SEC/PULSE)	0.05	0.8	0.5%	
SCALE FACTOR LINEARITY (%)	X		0.01	
SCALE FACTOR ASYMMETRY	X		1±0.00005	
RANGE (DEG/SEC)	0.11	2.0		
SCALE FACTOR STABILITY	X			0.01%/MO.
		X		0.1%/MO.
BANDWIDTH (HZ)	X	X	7 HZ MIN 0.5 < ζ < 1.0	
AIDR (SEC/SEC)	X		0.6	0.04/30DAY 0.003/6 HR 3.6/MO.
ASDR (SEC/SEC/G)	X	X	3.0	0.04/MO.
NOISE EQUIVALENT ANGLE (SEC)	X		1.0/1 HR P-P	
ANALOG RATE				
RANGE (DEG/SEC)	X	X	± 1.0 LINEAR 2.0 SAT.	
SCALE FACTOR (V/DEG/SEC)	X	X	12 ± 0.6	
SCALE FACTOR LINEARITY	10%	SAT.		
BANDWIDTH (HZ)	X	X	7 HZ MIN 0.5<ζ<1.0	
AIDR (BIAS) (SEC/SEC)	X		0.5	0.1/MO.
		X	7.2	3.6/MO.
ASDR (G SENSITIVITY)	X	X	3.0	0.04/MO.
NOISE (SEC/SEC RMS)	X	X	0.5(0.1 - 7 HZ)	
			0.05 (0.01 - 1HZ)	
			5.0 (100 HZ GREATER) MULTIPLES OF ROTOR FREQUENCY	
LIFE			2 YEAR (ORBIT) 2500 HOUR (GND) 600 - 1200 HOUR (PRE DELIVERY)	

Gyro noise characteristics are commonly measured using two methods—Power Spectral Density (PSD) and/or Noise Equivalent Angle (NEA) tests. The NEA measurement is conceptually quite simple. The instrument is operated in a stationary mode for a specified observation period (frequently one hour) and has the gyro rate output sampled at some frequency (5 Hz for the current example). The test is designed to evaluate the magnitude of the peak–to–peak excursions that occur during the test period. Any bias drift rate is corrected during this process, so analysis of the results of the test is performed in two stages [GOV–1]. The individual samples are summed to obtain the total drift angle, after which the linear

trend due to bias drift is removed via linear regression. The peak–to–peak NEA measurement of the remainder of the signal describes the angle noise. Sample drift time histories for the DRIRU–II are shown in Figure 4–7. In an uncompensated mode the value of the NEA was .63 arcseconds peak–to–peak, while with modified electronics the value decreased by better than an order of magnitude, to .048 arcseconds peak–to–peak. These results serve to further characterize the device as having a low noise content.

Another, more useful, way of measuring gyro noise characteristics is the Power Spectral Density test. The power spectrum may be described as the the magnitude squared of the linear spectrum of a given signal, in this case, gyro output. As such, it contains only magnitude information. A PSD plot for a conventional gyro when compared to the SDG–5 dry tuned gyro is shown in Figure 4–8.

Many conventional gyros show a signature characteristic in the PSD known as 'random walk.' Random walk is another term for integrated white noise. It can also easily be shown that the PSD of white noise is flat. The PSD of random walk, as inetegrated noise, would then exhibit a negative slope corresponding to -20 db/decade. The PSD of the derivative of the variable of interest would then, of course, be flat. Note that the conventional gyros of Figure 4–8 show a marked increase with decreasing frequency corresponding to this random walk signature.

Figures 4–9 through 4–11 show the results of PSD tests run on the DRIRU–II package. As the tests are run on different instruments at different facilities with varying capabilities and disturbance properties, it is difficult to draw any detailed conclusions for purposes of specifically modelling all the gyro idiosyncracies. Figure 4–9 [GRE–1] represents a test done at the manufacturer's facility. Note that this frequency data is plotted linearly in frequency, as opposed to logarithmically, which has the effect of spreading the details of the peaky areas. The information

accompanying this data suggests that the 33.8 Hz spikes are due to excitation of a 34 Hz test pad resonance by ambient conditions (rotating machinery, air movements, etc.). The 6 Hz spike corresponds to a V/F converter wash frequency. The 29.6 Hz peak is also considered, in the opinion of the test operator, to be environmental in nature. The peaks diminish when the device is reoriented on the test pad, suggesting strongly that these peaks are caused by ambient conditions rather than being a noise characteristic of the gyro itself.

A low frequency PSD for this device is shown in Figure 4–10 [GOV–1]. This measurement was also taken at the Teledyne test facility. The plots are quite flat within the narrow frequency range shown with no trace of a random walk signature. The noise in this case may be described as white at low frequencies. Figure 4–11 [GOV–1], shows a PSD test performed at the Holloman AFB Central Inertial Guidance Test Facility (CIGTF), a more sophisticated facility. The noise power content is flat until about 2.5 Hz, increases by a couple of orders of magnitude to about 25 Hz, then rolls off in random walk fashion. The shape of the curve is similar for the x and y channels of the test gyro. Although this plot is peakier than the others, the highest peaks are directly attributable to known factors. The 34 Hz spike is a bearing retainer frequency, 100 Hz is the rotor spin frequency, and 200 Hz is the second harmonic of the rotor spin frequency. Again, it is difficult to further separate environmental factors from the gyro characteristics. The results of these tests would have been improved by ensemble averaging but this was not done due to the time length required for extended low frequency testing. However, ensemble testing would no doubt smooth the details of the high frequency noise content.

The motion of the gyroscope testing platform due to seismic and environmental motions is not negligible when attempting to assess the accuracy of these extremely

sensitive gyros. An extended test [B&W-1] was conducted in a study of the facility at Holloman AFB. Sensitive sensors and geophones were used to measure table PSD's. The results exhibit peaks in the response of about the same order of magnitude as those found in the gyro PSD's previously presented. Most of the higher frequency spikes were traceable to environmental pumps and fans interacting with test table resonant frequencies.

The dominant characteristics of either curve of Figure 4-11 may be fit by a shaping filter of the form

$$H_g(s) = \frac{(\frac{s}{\omega_1} + 1)}{\frac{s^2}{\omega_2^2} + \frac{2\zeta s}{\omega_2} + 1} \tag{4.13}$$

For the case of a zero mean white noise input, a PSD for this response may be written in the form ([B&P-1])

$$G_y(\omega) = H_g(j\omega)H_g(-j\omega)G_x(\omega) \tag{4.14}$$

where G_y = PSD of gyro output, G_x = PSD of the gyro input, in this case the white noise driving the filter. This results in

$$G_y(\omega) = \frac{K_n\frac{\omega^2}{\omega_1^2} + 1}{\frac{\omega^4}{\omega_2^4} + (4\zeta^2 - 2)\frac{\omega^2}{\omega_2^2} + 1} \tag{4.15}$$

Values for ω_1, ω_2, ζ and K_n for each of the curves shown in Figure 4-11 are given in Table 4-2. These values are based on a visual assessment of the quality of the curve fit. The PSD's that result from the values of the parameters listed in Table 4-2 are compared with the original data in Figure 4-12.

Table 4–2
Results of Gyro PSD Curve Fit

	X Axis	Y Axis
K_n	6.5×10^{-8}	2.5×10^{-8}
ω_1	4.398 rad/sec (0.7 Hz)	6.283 rad/sec (1.0 Hz)
ω_2	103.7 rad/sec (16.5 Hz)	106.8 rad/sec (17 Hz)
ς	0.7	0.5

To represent the system in a state–space format for later incorporation into a system Kalman filter, consider that

$$H_g(s) = \frac{D(s)}{G_x(s)} \tag{4.16}$$

where

D = gyro drift (degrees/hour)

$G_x(s) = n_\omega$ = white noise input to shaping filter

The use of these values, when placed in the observer state form, results in

$$\begin{bmatrix} \dot{D} \\ \dot{X} \end{bmatrix} = \begin{bmatrix} -2\varsigma\omega_2 & 1 \\ -\omega_2^2 & 0 \end{bmatrix} \begin{bmatrix} D \\ X \end{bmatrix} + \begin{bmatrix} 1 \\ \omega_1 \end{bmatrix} n_\omega \tag{4.17}$$

where X is the necessary auxiliary state. These equations may then be incorporated into a Kalman filter with the star tracker.

Another approach to the problem is to simply describe the gyro noise content as white, with a PSD of the white noise set at some value Q corresponding to K_n of the 'fit' curve. Since the most recent control loop bandwidth specified for SIRTF is about 3 Hz [PSH–1], and the signature of the gyro PSD is fairly flat to about 2.5 Hz, this may be a reasonable assumption to make. The eventual filter equations are also simplified by use of this technique. These issues will be more completely addressed in Chapter Five.

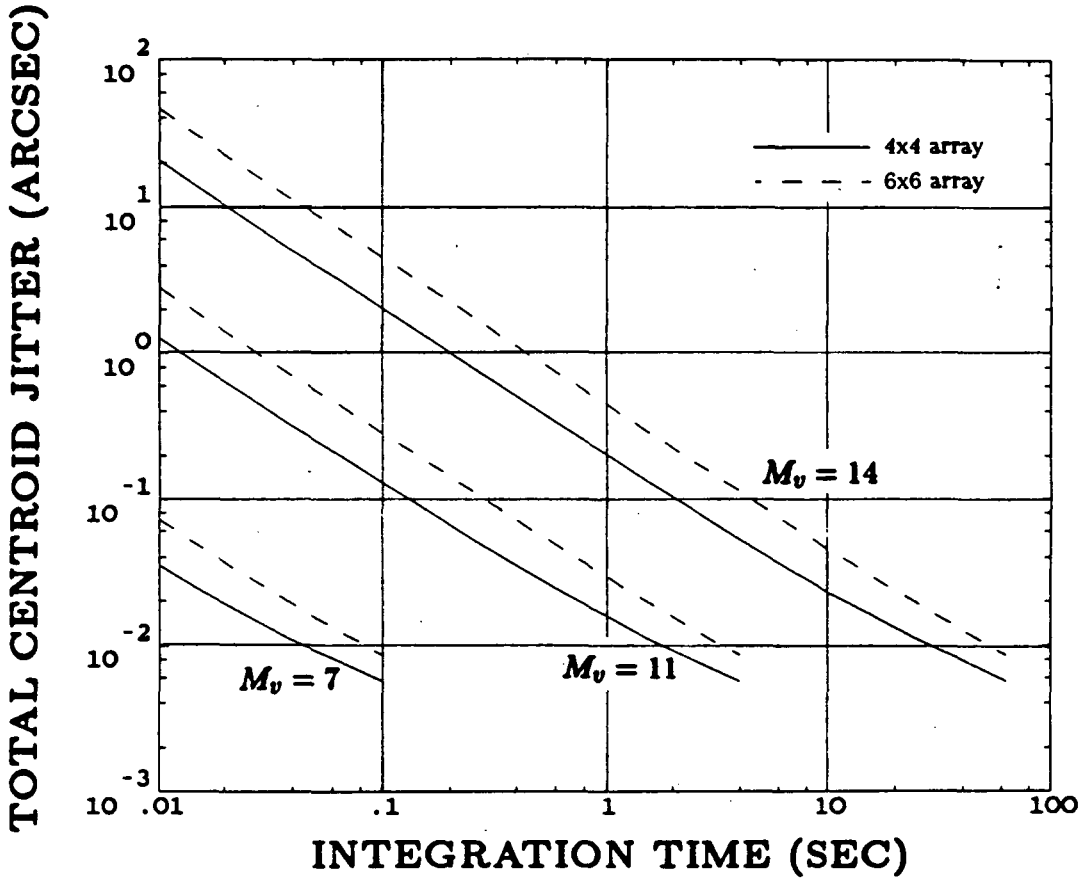

Figure 4–1 Centroid jitter for a stationary object as a function of star magnitude and pixel subarray dimension

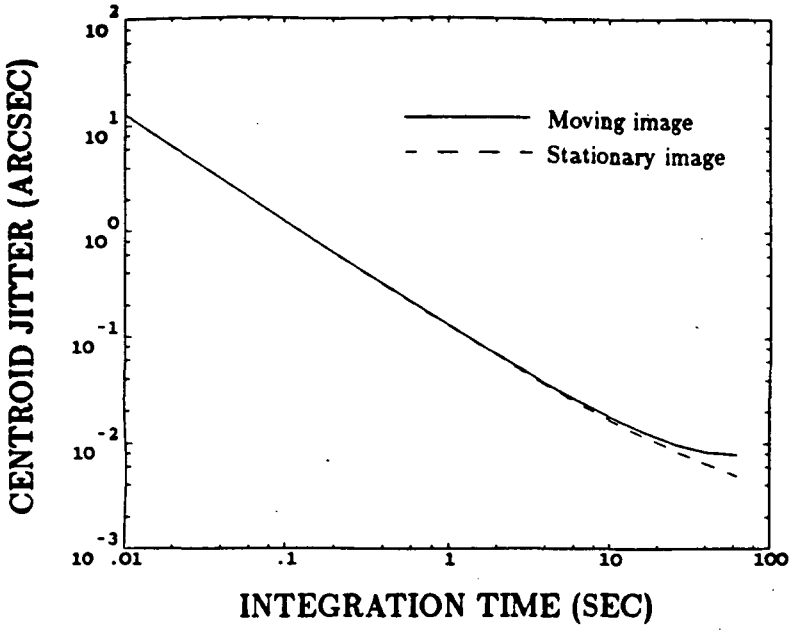

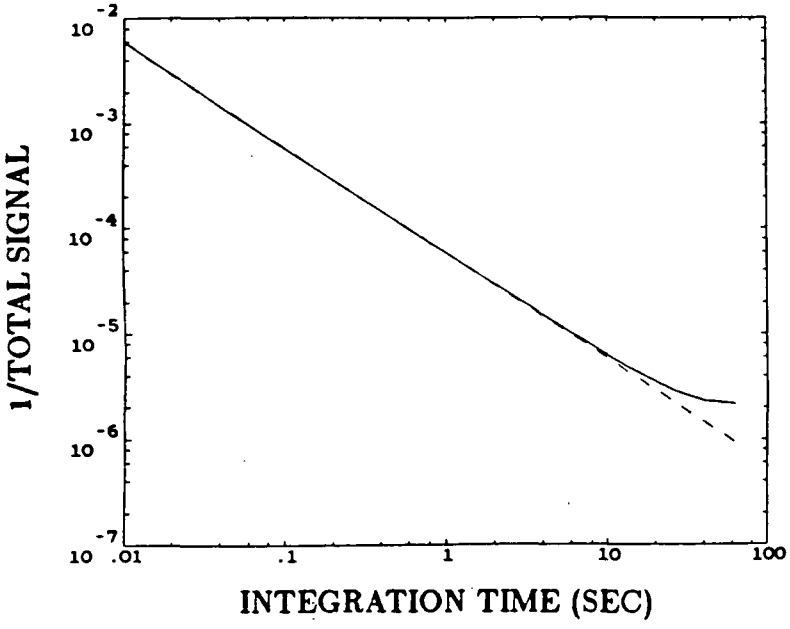

Figure 4–2 The impact of image motion upon centroid jitter levels for a 3x3 pixel subarray

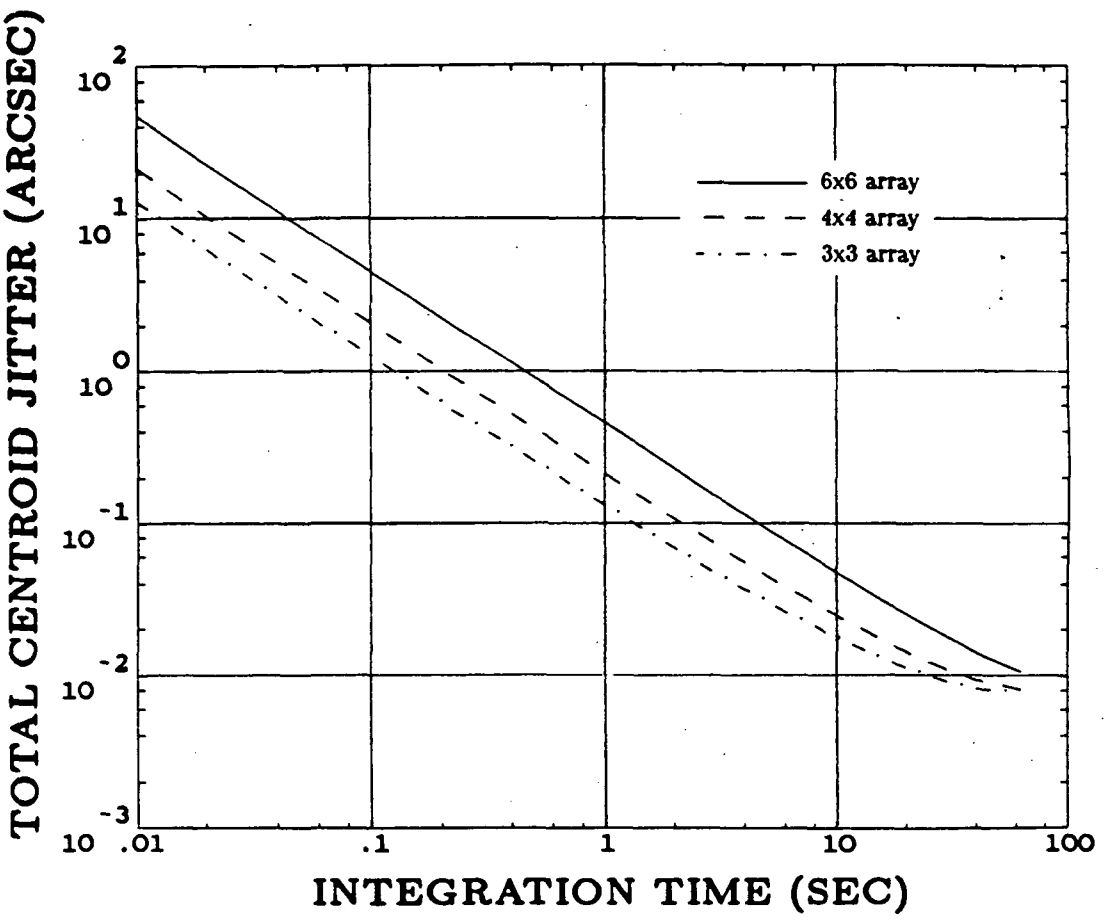

Figure 4–3 The effect of pixel subarray dimension upon jitter levels for a moving image

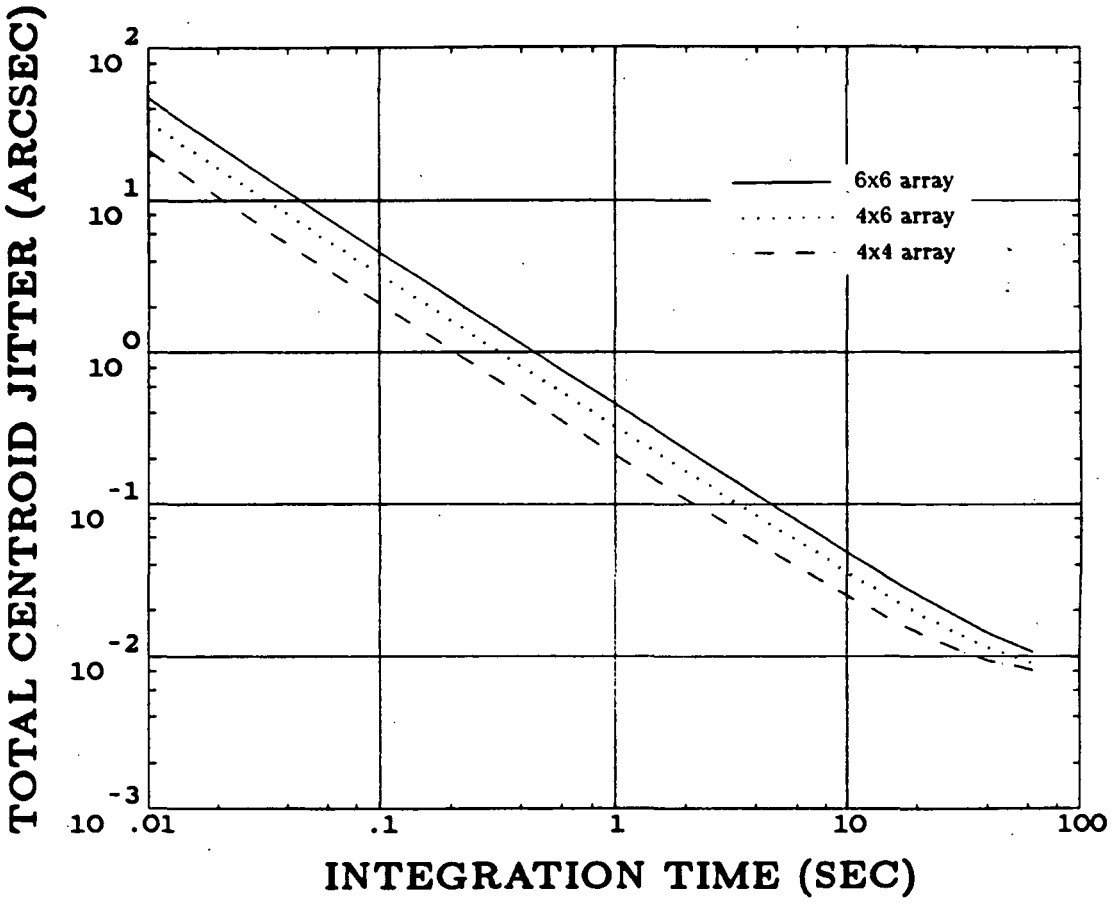

Figure 4–4 The effect of non–square pixel subarray dimensions upon jitter levels for a moving image

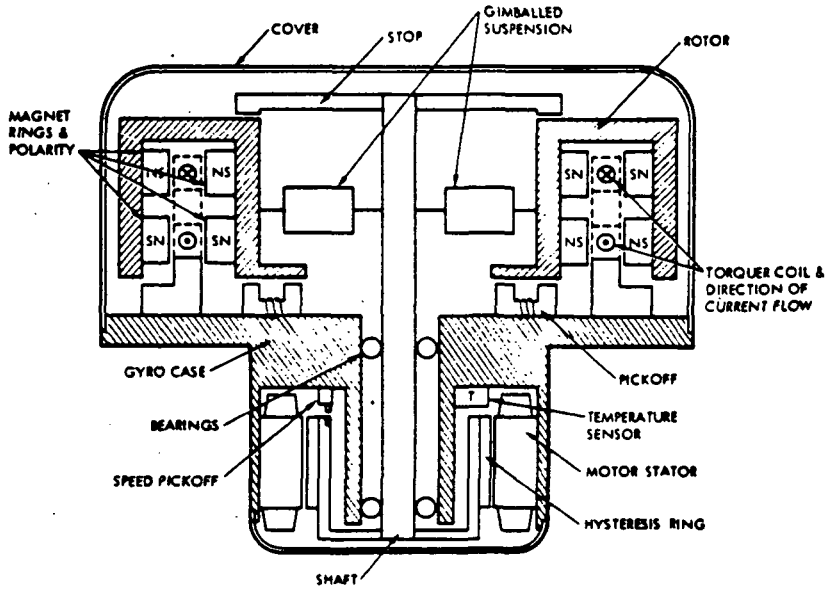

Figure 4–5 Cross–section of SDG–5 dry tuned gyro [GOV–1]

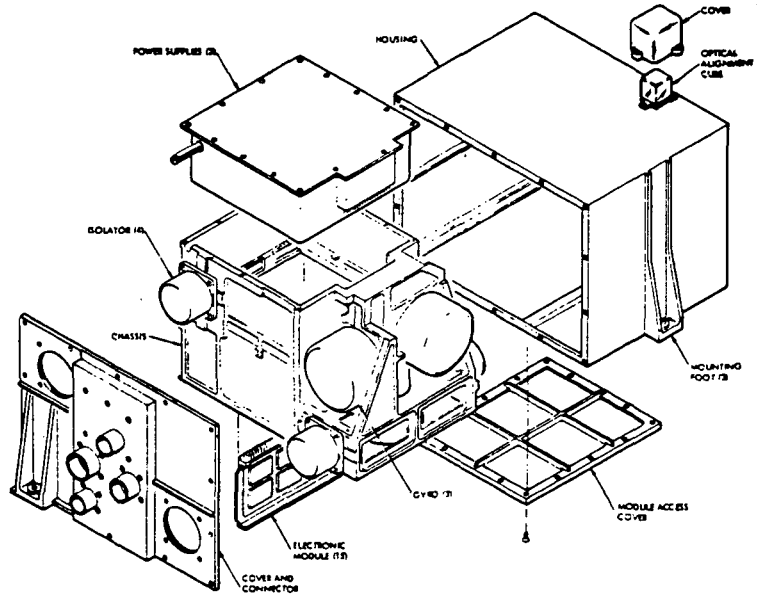

Figure 4–6 Exploded view of DRIRU–II gyro package [I&R–1]

Standard Package

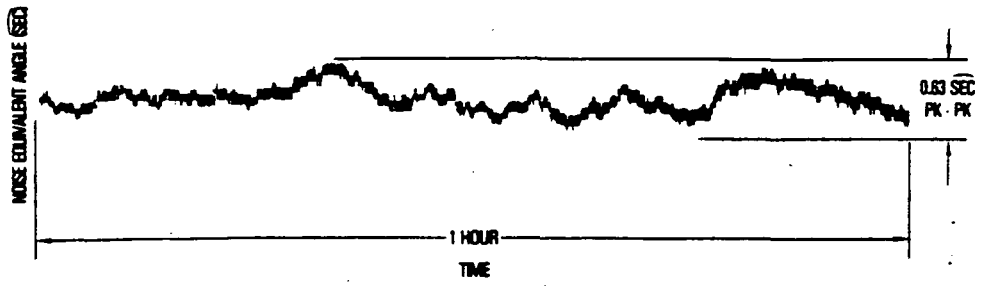

Modified Package

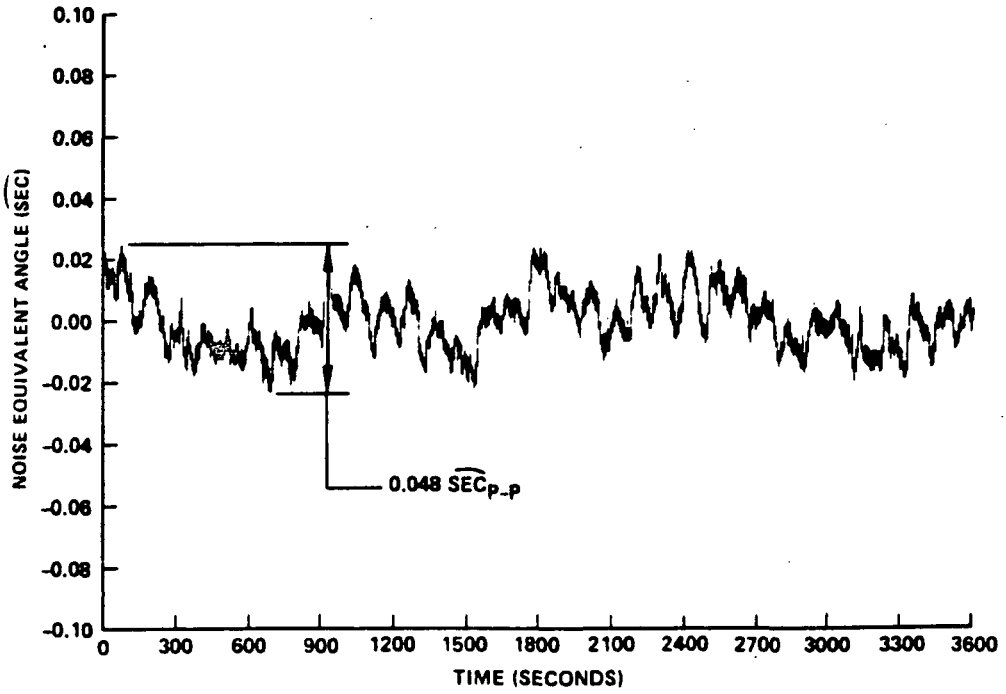

Figure 4–7 NEA time histories for the DRIRU–II Assembly [GOV–1]

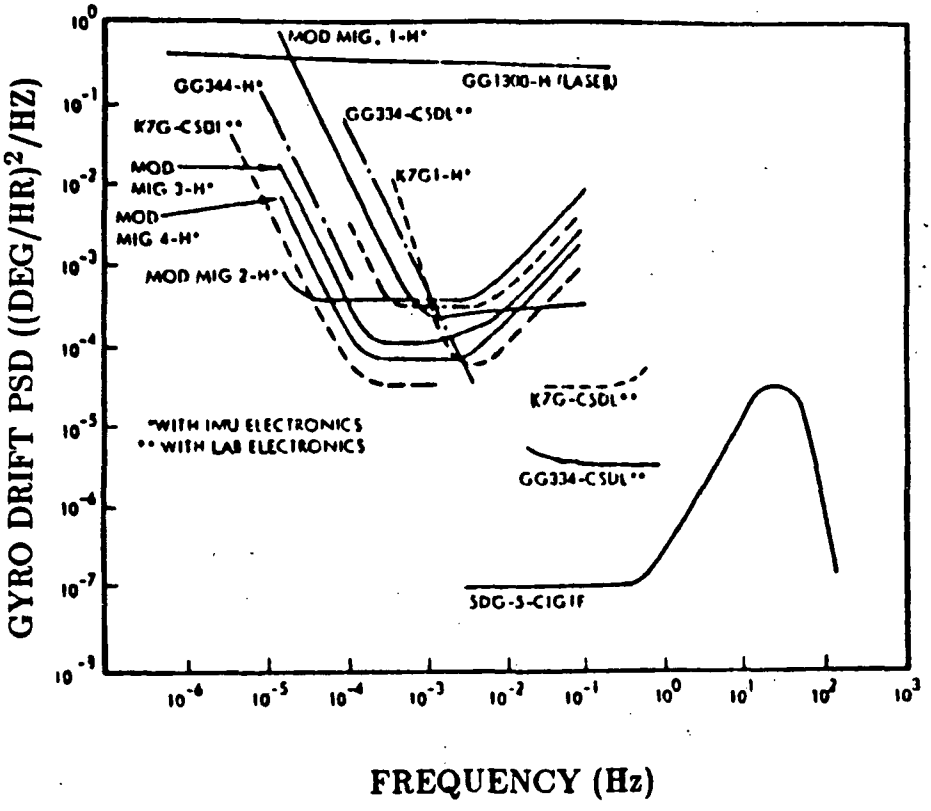

Figure 4–8 Comparison of PSD's for various conventional gyros with the PSD for the SDG–5 dry tuned gyro [DON–1]

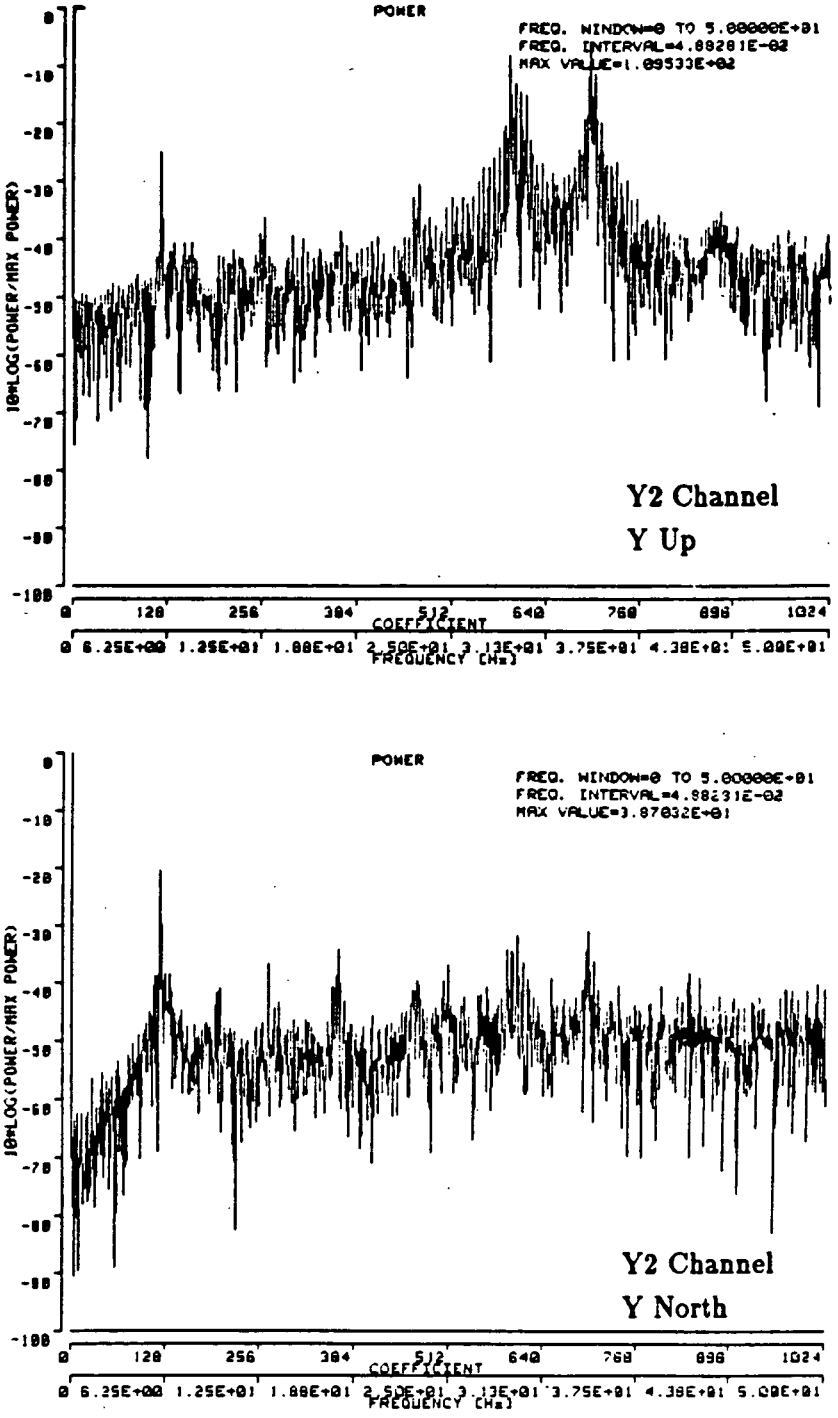

Figure 4–9 Power Spectral Density test for the DRIRU–II [GRE–1]

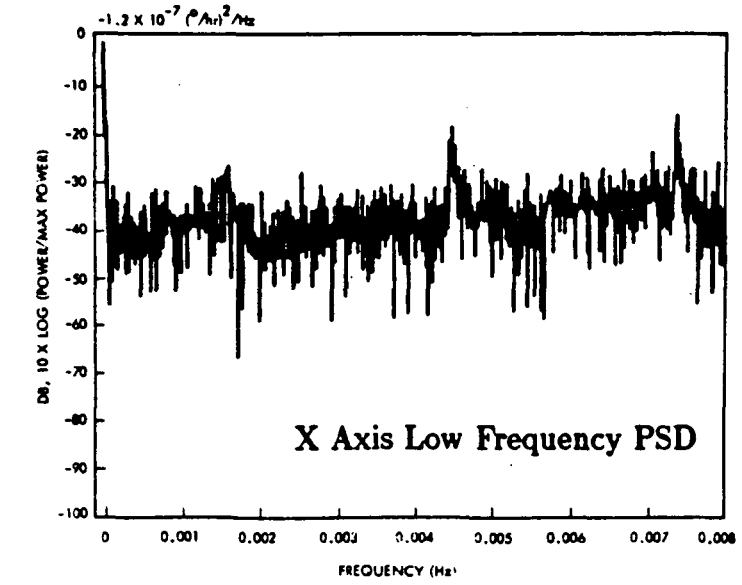

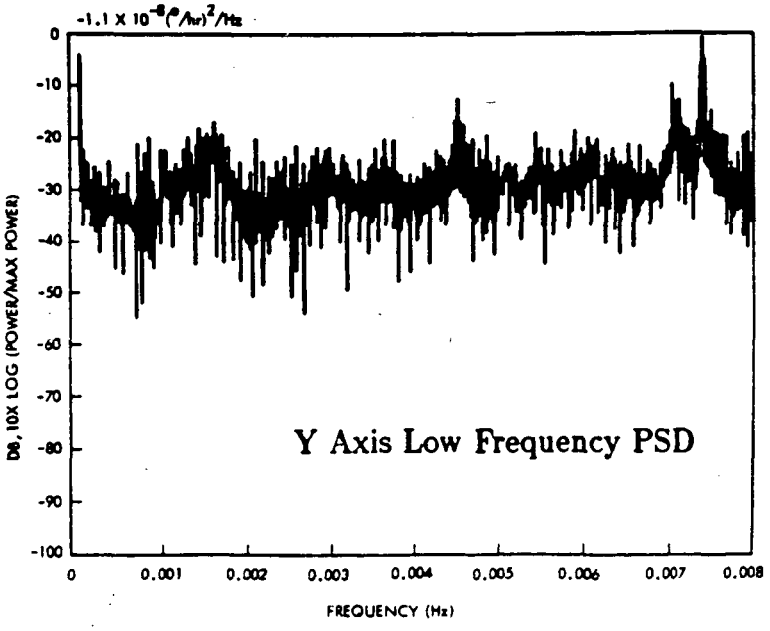

Figure 4–10 Low frequency PSD tests run at the Teledyne facility [GOV–1]

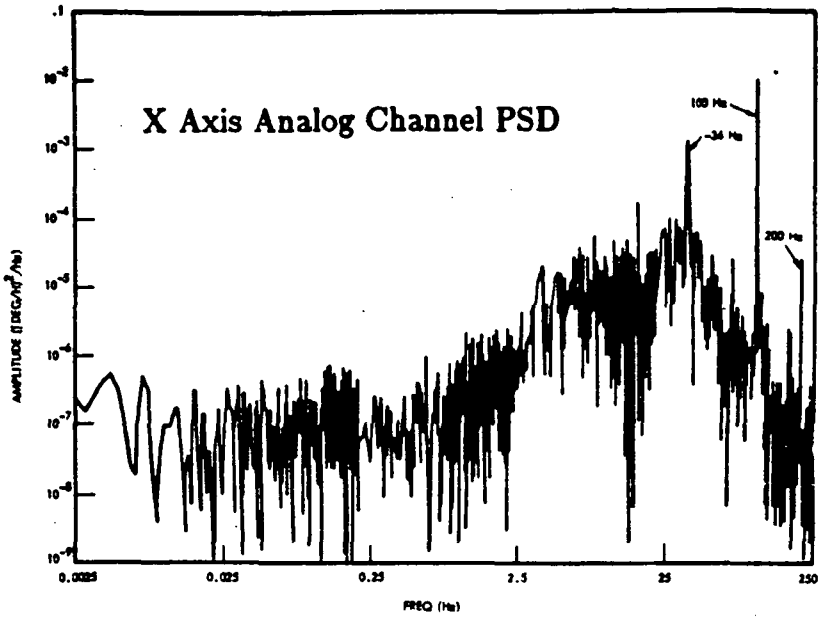

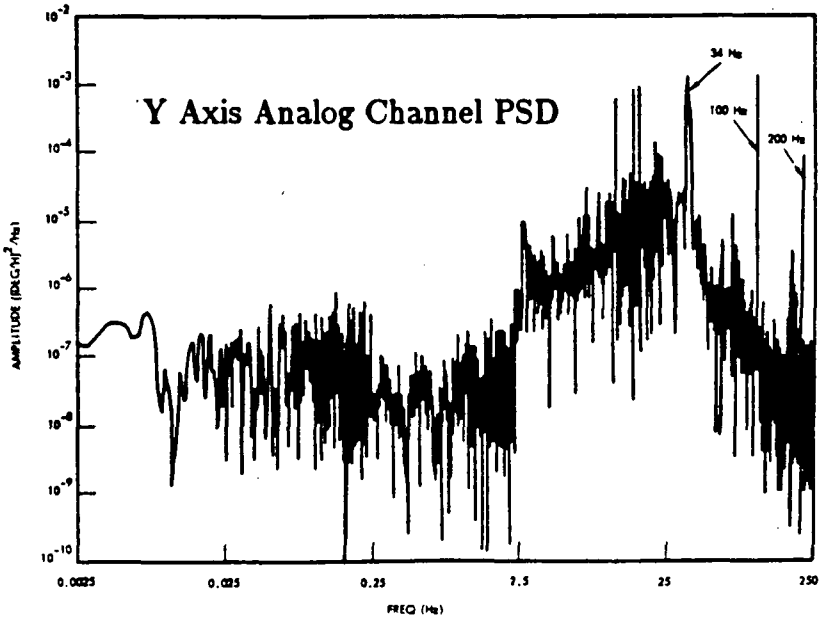

Figure 4–11 General PSD tests run at Holloman AFB [GOV–1]

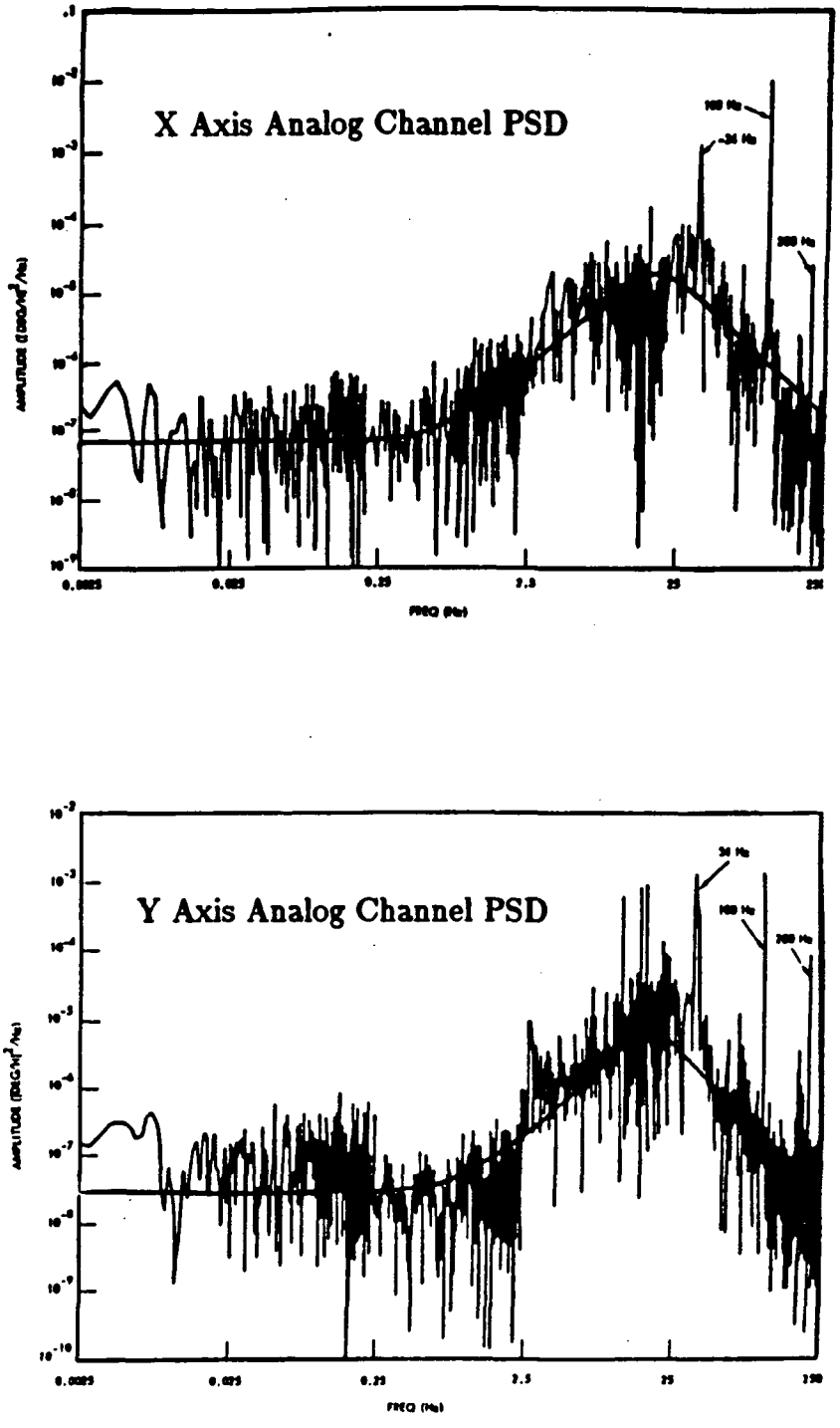

Figure 4-12 Comparison of PSD curves generated by equation 4.15 with test data

Chapter 5

Kalman Filter Analysis

The overall goal is that the best possible system performance be attained with the combination of the discrete star–tracker and the gyro package, utilizing the unique features of each to the greatest advantage. A method of accomplishing this task involves the use of optimal filtering and prediction, in which the accurate attitude measurement of the star–tracker is used to update an estimate of the gyro drift and therefore, pointing error. In this fashion, long–term stability against gyro drift is provided by the relatively slow–sampling CCD, while short–term stability between CCD readings is provided by the gyros. This chapter will present the additions to the original Kalman filter equations derived in [PAR–1] that are neccesary to include the case of moving targets as well as discuss the inclusion of the gyroscopic noise model.

As the concept for SIRTF has undergone a metamorphosis from a shuttle–fixed payload to a free–flying spacecraft, and the need for the added stabilization that a steerable secondary mirror would provide in question [PSH–1], the models presented here must be considered as conceptual in nature rather than resulting from finalized SIRTF control system design. Two studies relating to SIRTF control architecture have been published ([PSH–1] and [SAL–1]) which differ in scope and

configuration. Neither report, however, addresses the fine guidance sensor in detail. The discussion here will therefore be limited to interaction between the star tracker and the gyros, neglecting CMG's, flexible body dynamics and other sources of disturbance which may have an effect upon overall pointing accuracy.

The structure of the state space equations for the system has been previously established [PAR–1], and will be repeated briefly here. The continuous state equations take the familiar form for scalar inputs:

$$\begin{aligned} \dot{\mathbf{x}} &= \mathbf{F}\mathbf{x} + G_c u + G_n w \\ y &= H\mathbf{x} \end{aligned} \tag{5.1}$$

where $\mathbf{x}$ is an nx1 state vector, $\mathbf{F}$ is an nxn matrix, G_n and G_c are each have dimension nx1, while H is 1xn.

These equations may be equivalently expressed as a set of discretized equations

$$\begin{aligned} \mathbf{x}(n+1) &= \mathbf{\Phi}\mathbf{x}(n) + \Gamma_c u(n) + \Gamma_n w(n) \\ y(n) &= H\mathbf{x}(n) + v(n) \end{aligned} \tag{5.2}$$

where $\mathbf{\Phi}$ and Γ are computed using the matrix exponential $e^{\mathbf{F}T}$ in its series form and the integration time, T, ([F&P–1]) and $v(n)$ has been added to reflect the discrete star sensor measurement noise.

The Kalman filter equations take the familiar form ([BRY–1]):

Measurement update:

$$\begin{aligned} \hat{\mathbf{x}}(n+1) &= \bar{\mathbf{x}}(n+1) + K(n)\left[y(n+1) - H\bar{\mathbf{x}}(n+1)\right] \\ \mathbf{P}(n+1) &= \mathbf{M}(n) - \mathbf{M}(n)H^T(H\mathbf{M}(n)H^T + R)^{-1}H\mathbf{M}(n) \\ K(n) &= \mathbf{P}(n)H^T R^{-1} \end{aligned} \tag{5.3}$$

Time update:

$$\begin{aligned} \bar{\mathbf{x}}(n+1) &= \mathbf{\Phi}\hat{\mathbf{x}}(n) + \Gamma_c u(n) \\ \mathbf{M}(n+1) &= \mathbf{\Phi}\mathbf{P}(n)\mathbf{\Phi}^T + \Gamma_n Q \Gamma_n^T \end{aligned} \tag{5.4}$$

with $\mathbf{P}(0)$ and $\mathbf{x}(0)$ given. $\boldsymbol{Q}$ is the covariance of process noise and $\boldsymbol{R}$ is the covariance of the measurement noise. In addition,

$\bar{\mathbf{x}}_i$ = predicted estimate of $\mathbf{x}$, prior to a star measurement

$\hat{\mathbf{x}}_i$ = current estimate of $\mathbf{x}$, following a star measurement

$$\mathbf{M} = [E\{(\bar{\mathbf{x}}_i - \mathbf{x}_i)(\bar{\mathbf{x}}_i - \mathbf{x}_i)^T\}]^{\frac{1}{2}}$$

$$\mathbf{P} = [E\{(\hat{\mathbf{x}}_i - \mathbf{x}_i)(\hat{\mathbf{x}}_i - \mathbf{x}_i)^T\}]^{\frac{1}{2}}$$

The SIRTF attitude gyro has been modelled as a random-walk device in previous studies [PAR-1]. This requires that

$$\dot{D} = w \tag{5.5}$$

where D is the gyro drift (units of angular rate) and w is a white noise process with zero mean and variance Q.

The gyro drift over time produces a pointing error , i.e., the difference between the position of the star as maintained by the gyros and the actual position of the star, which may be expressed as

$$\theta_I(t) = -\int_0^t D(\tau)d\tau \tag{5.6}$$

or

$$\dot{\theta}_I = -D \tag{5.7}$$

where θ_I is the position of the star image on the CCD array. No other disturbances that would cause an error in the estimated position are included, such as bending between the point of attachment for the secondary mirror and the focal plane where the star sensor is mounted. The relations for the discrete star tracker measurement

may be given approximately as the average of the position of the star image over the time period, or

$$\theta_m = y(n) = \frac{1}{T}\int_{(n-1)T}^{nT} \theta_I(\tau)d\tau + v(n) \tag{5.8}$$

where θ_m is the measured image position from the star sensor. Alternately, defining Θ as the integral of image position, Equation 5.8 may be rewritten as

$$y(n) = \frac{1}{T}\{\Theta(nT) - \Theta[(n-1)T]\} + v(n) \tag{5.9}$$

where T is the star tracker integration time, and $v(n)$ is the discrete star tracker measurement noise with variance $R(T)$. Using this definition of Θ, then naturally

$$\dot{\Theta} = \theta_I. \tag{5.10}$$

The state–space equations that result from a stationary image with a discrete star tracker measurement and random walk gyro model are then given by

$$\begin{bmatrix} \dot{\Theta} \\ \dot{\theta}_I \\ \dot{D} \end{bmatrix} = \begin{bmatrix} 0 & 1 & 0 \\ 0 & 0 & -1 \\ 0 & 0 & 0 \end{bmatrix} \begin{bmatrix} \Theta \\ \theta_I \\ D \end{bmatrix} + \begin{bmatrix} 0 \\ 0 \\ 1 \end{bmatrix} w(t) \tag{5.11}$$

The addition of a moving target would add a commanded rate to the gyros provided by onboard electronics. If the gyros receive a scanning command $\dot{\theta}_c$, then the angle relation (Equation 5.6) above becomes

$$\theta_I = -\int_0^t D(\tau)d\tau - \int_0^t \dot{\theta}_c(\tau)d\tau \tag{5.12}$$

which adds to the state equations as

$$\begin{bmatrix} \dot{\Theta} \\ \dot{\theta}_I \\ \dot{D} \end{bmatrix} = \begin{bmatrix} 0 & 1 & 0 \\ 0 & 0 & -1 \\ 0 & 0 & 0 \end{bmatrix} \begin{bmatrix} \Theta \\ \theta_I \\ D \end{bmatrix} + \begin{bmatrix} 0 \\ 0 \\ 1 \end{bmatrix} w(t) + \begin{bmatrix} 0 \\ -1 \\ 0 \end{bmatrix} \dot{\theta}_c(t) \tag{5.13}$$

This equation is readily discretized using a simple summation of the series form of the matrix exponential, leading to

$$\begin{bmatrix} \Theta \\ \theta_I \\ D \end{bmatrix}_{(n+1)} = \begin{bmatrix} 1 & T & \frac{-T^2}{2} \\ 0 & 1 & -T \\ 0 & 0 & 1 \end{bmatrix} \begin{bmatrix} \Theta \\ \theta_I \\ D \end{bmatrix}_{(n)} + \begin{bmatrix} -\frac{T^3}{6} \\ -\frac{T^2}{2} \\ T \end{bmatrix} w(n) + \begin{bmatrix} -\frac{T^2}{2} \\ -T \\ 0 \end{bmatrix} \dot{\theta}_c(n) \quad (5.14)$$

Note that the discrete star-tracker measurement as given by Equation 5.12 involves a delayed state of Θ. This requires augmentation of the state vector by the state $\Theta'(n)$, which is simply $\Theta(n)$ delayed by one sample period, that is

$$\Theta'(n+1) = \Theta(n) \quad (5.15)$$

The discretized equations then become

$$\begin{bmatrix} \Theta' \\ \Theta \\ \theta_I \\ D \end{bmatrix}_{(n+1)} = \begin{bmatrix} 0 & 1 & 0 & 0 \\ 0 & 1 & T & -\frac{T^2}{2} \\ 0 & 0 & 1 & -T \\ 0 & 0 & 0 & 1 \end{bmatrix} \begin{bmatrix} \Theta' \\ \Theta \\ \theta_I \\ D \end{bmatrix}_{(n)} + \begin{bmatrix} 0 \\ -\frac{T^3}{6} \\ -\frac{T^2}{2} \\ T \end{bmatrix} w(n) + \begin{bmatrix} 0 \\ -\frac{T^2}{2} \\ -T \\ 0 \end{bmatrix} \dot{\theta}_c(n) \quad (5.16)$$

with

$$y(n) = \begin{bmatrix} -1/T & 1/T & 0 & 0 \end{bmatrix} \begin{bmatrix} \Theta' \\ \Theta \\ \theta_I \\ D \end{bmatrix}_{(n)} + v(n) \quad (5.17)$$

This system is not strictly observable, in that the observability matrix composed of

$$\begin{bmatrix} H \\ H\Phi \\ H\Phi^2 \\ H\Phi^3 \end{bmatrix} \quad (5.18)$$

has rank less than four, the order of the system. This is due in part to the method in which the measurement equation was constructed, i.e. the delayed state Θ' was added to the discrete equations solely for the purpose of modelling the measurement equation. Further observability analysis shows that only θ_I, D and the combination

of Θ and Θ' may be estimated accurately. This is a function of the mathematical model chosen for the star tracker measurement. This result makes intuitive sense, as the measurement of star position from the CCD is, in reality and as modelled, an average of its actual position during that sample period. One may not expect to be able to estimate the limits of motion, represented here by Θ and Θ', from the average of the two. From a physical viewpoint, it is impossible to estimate these limits. For all practical purposes, however, accurate estimates of D and θ_I are possible, with no need for estimation of the other two states individually, only their combination.

It is interesting to note that no "velocity correction" term of $\frac{T}{2}\dot{\theta}_c$ is explicitly added to the state equations as discussed in Chapter Three. The addition of the $\dot{\theta}_c$ command term is sufficient for estimation (assuming of course that the quality of the measurement from the CCD itself is good and is subject to no signal loss). This result will now be demonstrated.

The Kalman filter term

$$y' = [y(n+1) - H\bar{\mathbf{x}}(n+1)] \tag{5.19}$$

contained in the relation

$$\hat{\mathbf{x}}(n+1) = \bar{\mathbf{x}}(n+1) + K(n)\,[y(n+1) - H\bar{\mathbf{x}}(n+1)]$$

of Equations 5.3 should ideally go to zero for a perfect estimate in the absence of noise. This can be proven for the case of a moving target by manipulation of the Kalman filter equations. By substitution of $H\bar{\mathbf{x}}$ from the state equation (Equation 5.16) into Equation 5.18

$$y' = y(n+1) + \frac{1}{T}[\bar{\Theta}'(n+1) - \bar{\Theta}(n+1)]$$

Substitute for the $n+1$ terms from the state equations 5.16:

$$y' = y(n+1) - \bar{\theta}_I(n) + \frac{T}{2}\bar{D}(n) + \frac{T}{2}\dot{\theta}_c(n)$$

If this equation is now set equal to zero, the desired steady state error, and then solved for $\bar{\theta}_I$, the angle estimate error, then

$$\theta_I(n) = \underbrace{y(n+1)}_{startrackermeasurement} + \underbrace{\frac{T}{2}\bar{D}(n)}_{correctionfordrift} + \underbrace{\frac{T}{2}\dot{\theta}_c(n)}_{correctionforscanrate} \tag{5.20}$$

In reality, there will naturally be some error, since estimates are not perfect due to the presence of process and measurement noise and even this model assumes linear target motion during the sample period. Even though the overall target motion is not expected to be linear, this may not be a bad assumption, as a piecewise linear approximation to the curve will most likely be acceptable. However, it is evident that the correction for motion rate as presented in Chapter Three is present within the structure of the equations.

The addition of the dry-tuned gyro noise model presented in Chapter Four results in the following continuous state equations:

$$\begin{bmatrix} \dot{\Theta} \\ \dot{\theta}_I \\ \dot{D} \\ \dot{X} \end{bmatrix} = \begin{bmatrix} 0 & 1 & 0 & 0 \\ 0 & 0 & -1 & 0 \\ 0 & 0 & -2\zeta\omega_2 & 1 \\ 0 & 0 & -\omega_2^2 & 0 \end{bmatrix} \begin{bmatrix} \Theta \\ \theta_I \\ D \\ X \end{bmatrix} + \begin{bmatrix} 0 \\ 0 \\ 1 \\ \omega_1 \end{bmatrix} w(t) + \begin{bmatrix} 0 \\ -1 \\ 0 \\ 0 \end{bmatrix} \dot{\theta}_c \tag{5.21}$$

This system is more challenging to discretize, however. The powers of the matrix $\mathbf{F}$ in this case do not conveniently go to zero when calculating the matrix exponential as before and the resulting expressions for Φ and Γ are complicated, even for the first two or three terms of the series expansion. In addition, this series tends to diverge within the first few terms for larger values of T (greater than .01 seconds) when attempting numerical computation, which makes a simple series truncation of the matrix exponential unacceptable and inaccurate. This

type of phenomena is a common shortfall of using direct series summation for the evaluation of Φ and Γ and is generally caused by finite computer accuracy [M&L-1].

There are several other methods of calculating the matrix exponential, however. One method is to rewrite the summation for the matrix exponential in the form

$$\Phi \approx \mathbf{I} + \frac{\mathbf{F}T}{2}\left(\mathbf{I} + \frac{\mathbf{F}T}{3}\left(\cdots \frac{\mathbf{F}T}{N-1}\left(\mathbf{I} + \frac{\mathbf{F}T}{N}\right)\right)\cdots\right)$$

This method, known as "scaling and squaring," is summarized in [F&P-1] and is implemented in several of the 'standard' controls-system analysis packages. It is quite effective during most applications and gives adequate results for this case if sufficient computer precision is used. Extra precision is required, however, if there are large differences between the magnitudes of the elements of the $\mathbf{F}$ matrix and the sampling times are long, as are present in this problem.

Example Φ, Γ_n and Γ_c matrices that result for several sample rates are shown in Table 5-1 for the gyro shaping filter constants listed in Table 4-1 for the Y axis gyro PSD. The state vector has been augmented by the delay state Θ' as described in Equation 5.15. This increases the order of the discrete equations over the continuous system by one. The discrete measurement equation is unchanged from Equation 5.17 with the exception of the addition of the unmeasured state X:

$$y(n) = \begin{bmatrix} -1/T & 1/T & 0 & 0 & 0 \end{bmatrix} \begin{bmatrix} \Theta' \\ \Theta \\ \theta_I \\ D \\ X \end{bmatrix}_{(n)} + v(n) \qquad (5.22)$$

It is noted that, as expected, the Φ's for very high sample rates approach the identity matrix plus a term for the noise dynamics.

Table 5–1
Discretized State Equations at Varying Sample Times

$$x = [\theta' \quad \Theta \quad \theta_I \quad D \quad X]^T$$

$T = 0.0001$ sec

$$\Phi = \begin{bmatrix} 0 & 1 & 0 & 0 & 0 \\ 0 & 1 & 0.0001 & -5.0 \times 10^{-9} & 0 \\ 0 & 0 & 1 & -9.9 \times 10^{-5} & -5.0 \times 10^{-9} \\ 0 & 0 & 0 & .99 & -9.9 \times 10^{-5} \\ 0 & 0 & 0 & -1.135 & 1.0 \end{bmatrix}$$

$T = 0.0001$ sec

$$\Gamma_n = \begin{bmatrix} 0 \\ -1.7 \times 10^{-13} \\ -5.0 \times 10^{-9} \\ 1.0 \times 10^{-5} \\ 5.7 \times 10^{-4} \end{bmatrix}$$

$T = 0.0001$ sec

$$\Gamma_c = \begin{bmatrix} 0 \\ -5.0 \times 10^{-9} \\ -1.0 \times 10^{-4} \\ 0 \\ 0 \end{bmatrix}$$

$T = 0.001$ sec

$$\Phi = \begin{bmatrix} 0 & 1 & 0 & 0 & 0 \\ 0 & 1 & 0.001 & -4.8 \times 10^{-7} & 0 \\ 0 & 0 & 1 & -9.5 \times 10^{-4} & -4.8 \times 10^{-7} \\ 0 & 0 & 0 & 0.89 & -9.5 \times 10^{-4} \\ 0 & 0 & 0 & -10.8 & 0.99 \end{bmatrix}$$

$T = 0.001$ sec

$$\Gamma_n = \begin{bmatrix} 0 \\ -1.6 \times 10^{-10} \\ -4.8 \times 10^{-7} \\ 9.5 \times 10^{-4} \\ 7.7 \times 10^{-4} \end{bmatrix}$$

$T = 0.001$ sec

$$\Gamma_c = \begin{bmatrix} 0 \\ -5.0 \times 10^{-7} \\ -1.0 \times 10^{-3} \\ 0 \\ 0 \end{bmatrix}$$

$T = 0.01$ sec

$$\Phi = \begin{bmatrix} 0 & 1 & 0 & 0 & 0 \\ 0 & 1 & 0.01 & -3.3 \times 10^{-5} & -1.2 \times 10^{-7} \\ 0 & 0 & 1 & -5.1 \times 10^{-3} & -3.3 \times 10^{-5} \\ 0 & 0 & 0 & 0.083 & 5.1 \times 10^{-3} \\ 0 & 0 & 0 & -57.7 & 0.62 \end{bmatrix}$$

$T = 0.01$ sec

$$\Gamma_n = \begin{bmatrix} 0 \\ -1.3 \times 10^{-7} \\ -3.3 \times 10^{-5} \\ 5.3 \times 10^{-3} \\ 0.32 \end{bmatrix}$$

$T = 0.01$ sec

$$\Gamma_c = \begin{bmatrix} 0 \\ -5.0 \times 10^{-5} \\ -0.1 \\ 0 \\ 0 \end{bmatrix}$$

Table 5–1 presents results only for sample times less than 0.01 second. This is a relatively high rate in CCD terms, as poor accuracy and high noise levels accompany a CCD sampling quickly with a dim star. For slower sampling rates, the speed of the dynamics of the gyro noise shaping filter must be considered. The natural frequency of the filter is very fast (about 17 Hz) when compared to the projected sampling rates of 1–0.1 Hz for dim stars. If the rule of thumb of sampling no slower than twice the system natural frequency is observed, then the slowest sample time at which the colored noise characteristics could be estimated is around

0.1 second. Some reduction of the state equations will then occur if the sample rates are very slow.

The nature of this state reduction is suggested by the gyro PSD shown in Figure 4–12. It is apparent that the gyro noise characteristics may not be modelled accurately by a random walk model. In fact, the Power Spectral Density of the noise is flat for low frequencies, suggesting that the gyro drift rate in these regimes may be modelled as white, or

$$D = w \tag{5.23}$$

Since the continous model defined the drift angle, θ_I, as

$$\dot{\theta}_I = -D$$

then, for this reduced case,

$$\dot{\theta}_I = -w \tag{5.24}$$

The gyro drift **rate** is white, therefore the gyro drift **angle** is a random walk process.

The resulting reduced order continuous system is very simple:

$$\begin{bmatrix} \dot{\Theta} \\ \dot{\theta}_I \end{bmatrix} = \begin{bmatrix} 0 & 1 \\ 0 & 0 \end{bmatrix} \begin{bmatrix} \Theta \\ \theta_I \end{bmatrix} + \begin{bmatrix} 0 \\ -1 \end{bmatrix} w(t) + \begin{bmatrix} 0 \\ -1 \end{bmatrix} \dot{\theta}_c(t) \tag{5.25}$$

Discretizing is also simple, and, after the augmentation of the state vector by the delay state Θ', the discrete equations are

$$\begin{aligned} \begin{bmatrix} \Theta' \\ \Theta \\ \theta_I \end{bmatrix}_{(n+1)} &= \begin{bmatrix} 0 & 1 & 0 \\ 0 & 1 & T \\ 0 & 0 & 1 \end{bmatrix} \begin{bmatrix} \Theta' \\ \Theta \\ \theta_I \end{bmatrix}_{(n)} + \begin{bmatrix} 0 \\ -\frac{T^2}{2} \\ -T \end{bmatrix} w(n) + \begin{bmatrix} 0 \\ -\frac{T^2}{2} \\ -T \end{bmatrix} \dot{\theta}_c(n) \\ y(n) &= \begin{bmatrix} -1/T & 1/T & 0 \end{bmatrix} \begin{bmatrix} \Theta' \\ \Theta \\ \theta_I \end{bmatrix}_{(n)} + v(n) \end{aligned} \tag{5.26}$$

The pointing errors that result from the combination of a random walk gyro drift rate and the discrete star tracker have been examined in detail ([PAR–1],

[P&P-1] and [PPL-1]). An example of the variation of pointing error with CCD sample time is shown in Figure 5-1. This data was created by iteration of the matrix Riccati equations until convergence in the covariance matrices **M** and **P** was observed. The pointing estimate error just preceding a measurement is then given by

$$\left(\mathbf{M}_{\theta_I}(n)\right)^{1/2} = \left[E\left\{\left(\hat{\theta}_I(n) - \theta_I(n)\right)^2\right\}\right]^{1/2}$$

while the estimate error just after a measurement is given by

$$\left(\mathbf{P}_{\theta_I}(n)\right)^{1/2} = \left[E\left\{\left(\bar{\theta}_I(n) - \theta_I(n)\right)^2\right\}\right]^{1/2}$$

where $\mathbf{P}_{\theta_I}$ and $\mathbf{M}_{\theta_I}$ are the current and predicted elements of the covariance matrices corresponding to the state θ_I. The major result from this previous work describes the effect of a tradeoff between gyro drift and CCD integration time. At short integration times, very little gyro drift may occur, but the measurement noise from the star tracker is large. At longer integration times, the CCD noise is less, but the gyro can drift further within that period. An optimum sample time of 15.8 seconds for the example in Figure 5-1 gives the best pre-measurement prediction using the Fairchild CCD described in Chapter Two. The best post-measurement prediction is found at a sample period of 63 seconds. The Ferranti 125 gyro employed for these results had a PSD value for the strength of the random walk drift rate of 4.1667×10^{-10} arcsec^2/second^3 [PAR-1].

Similar results arise for the reduced-order system of Equation 5.25, even though the gyro drift angle is modelled as a random walk instead of the drift rate. The current and predicted estimate error curves for this system are shown in Figure 5-2. The CCD noise levels were implemented based upon the RCA CCD, a 14th magnitude star, and a 4x4 integration subarray as shown in Figure 4-1. The noise spectral density for the gyro drift is taken from the Y-axis gyro described in

Table 4–2 as 2.5×10^{-8} arcsec^2/second^2, or the power of the flat part of the curve of Figure 4–12.

Although the drift rate is random, the drift angle is a random walk and will meander in time. This accounts for the similarities in the curve shapes between the two figures, specifically, the rise in estimate error at long integration times due to the larger potential for the presence of a drift angle. The sample time at which optimum performance is observed has changed little, with the T at which the current estimate error is minimized (0.003 arcseconds) occurring at about 39 seconds, while the minimum predicted estimate error (0.0038 arcseconds) is found at about 10 seconds. The overall magnitude of the pointing estimate error is decreased from about 0.025 arcseconds for the system in Figure 5–1 to 0.0055 arcseconds for the system in Figure 5–2 at a CCD integration time of 1 second. This decrease is due to the different gyro error characteristics of the NASA DRIRU-II when compared to the Ferranti 125. While the CCD contribution to measurement noise is now greater than predicted by Parsons ([PAR–1]) for the reasons described in Section 4.1, the improvement of the gyro process noise characteristics more than compensates for this increase. Therefore, the use of CCD subarrays of larger dimension than 3x3 during image motion still results in acceptable pointing estimation error levels. This supports the obvious conclusion that a gyroscope with better drift characteristics will provide much improved pointing stability. The decision to implement this type of gyro on this mission appears to be well-founded, based upon the published test data.

These pointing errors have been based on gyro errors and CCD random errors only. Chapter Three discusses the sizeable errors that can result from uncompensated target motion. Errors of greater than 1 arcsecond are possible if the necessary corrections for image motion are not made.

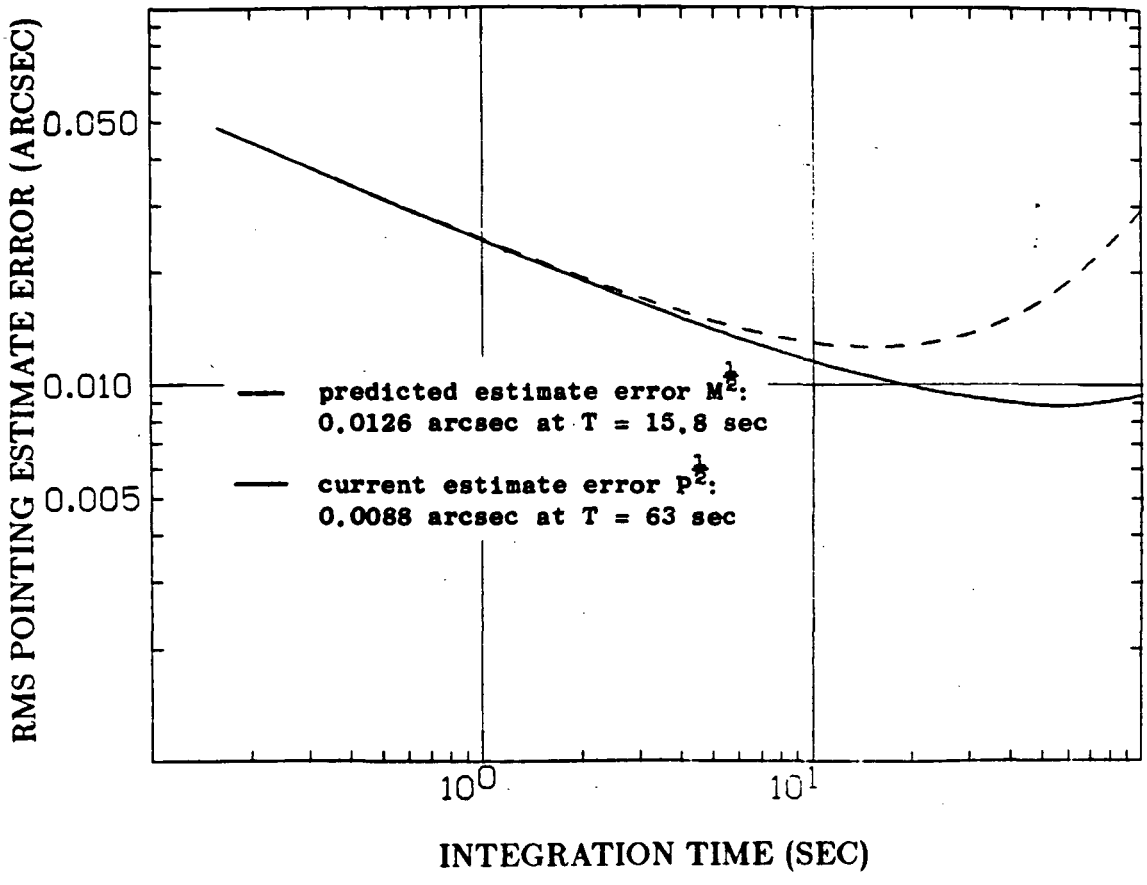

Figure 5–1 Optimal pointing estimate error versus star tracker integration time, Random walk gyro model [PAR–1]

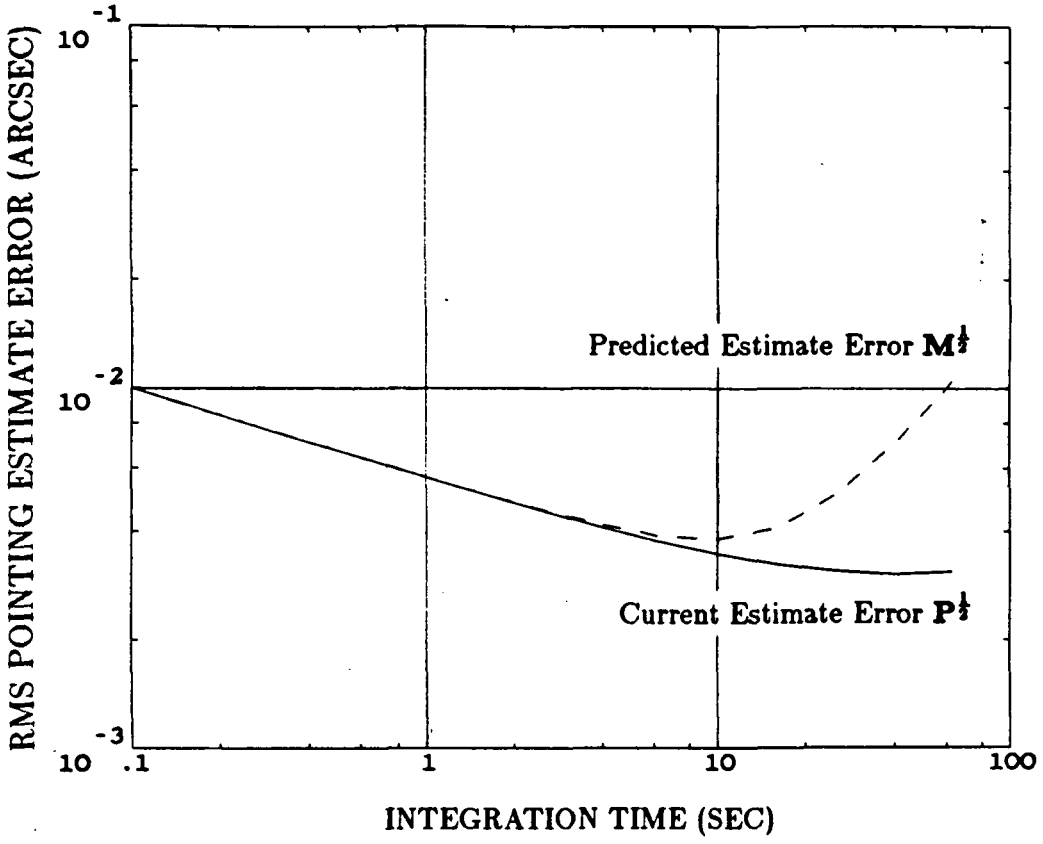

Figure 5–2 Optimal pointing estimate error versus star tracker integration time, Random drift gyro model

Chapter 6

Conclusions

This thesis has presented a basic overview of the application of charge-coupled devices, or CCD's, to the problem of attitude determination in a space-based infrared telescope. The operation of this device has been described and the results of several previous studies on the subject have been summarized. The method is based upon the concept that star images may be defocussed over several pixels of the sensor, with the resulting centroid of the matrix of signal levels on those pixels corresponding to star position. The use of this method, developed by JPL, results in an increase in accuracy of better than an order of magnitude over the case in which the image is focussed on a single pixel. A computer simulation routine for this process has been previously developed and the absolute accuracy estimates that resulted have been presented. The results of previous work have been extended, however, to include a newer device with a different pixel configuration.

The main purpose of this study, however, was to assess the performance levels that may be expected when the CCD is used for purposes of tracking a target in motion. The nature of the motion for any given infrared target is assumed to be scientifically well-tabulated, but, since the particular application pertains to an infrared telescope, the possibility arises that the desired target will have visible

light emissions below the operating threshold of the sensor. The system would then be required to operate in an open loop mode, with a command generated to the spacecraft gyros such that the visible guide stars move across the face of the CCD in a manner corresponding to the charted motion of the infrared target.

A computer simulation of the CCD signals that a moving image would generate was derived for the purpose of performance assessment. Effectively, the CCD averages the position of the star upon its face over a given integration time. While this has acceptable accuracy for a stationary target, the presence of motion means that the calculated position of the star will be somewhere between its position at the beginning and the position at the end of the integration period. If the target motion is linear, a simple correction term based upon projected motion may be added to produce absolute error levels which approach those that are obtainable for a stationary image.

Errors naturally increase when the image strays off the edge of the small intergration subarray of pixels. This limits the amount of motion that any particular target may experience during an integration period which in turn limits the possible combination of subarray sizes, allowable image motion, and integration time. It could, in fact, effectively limit the guide star selection, in that a set of very bright stars may need to be selected in order to allow a decrease in sample time which in turn, insures that the image stays within the area of integration..

The increase in dimension of the pixel integration subarray decreases the probability that the image will stray from the area but this is done at some expense. By increasing the pixel subarray size, the resultant centroid noise, or jitter, is increased. This results largely from the increased 'moment-arm' that background noise signals from the pixel elements have upon the calculation of star position. A possible compromise between reduced absolute accuracy and increased jitter levels

is to increase the dimension of the CCD integration area in the direction of the known motion.

The star tracker and the spacecraft gyroscopes are to work in tandem, with the presence of the star tracker providing necessary gyroscopic drift correction. Previous studies discussed a random walk gyro model incorporated into a Kalman filter for the purpose of estimating gyro drift from star-tracker measurements. The random walk model is applicable to most conventional floated gyros. The gyro currently slated for use on the telescope in question is, however, a gyroscope of a different technology which posesses noise characteristics not adequately described by the simple random walk. The characteristics of this dry-tuned gyro have been modelled to create a noise shaping filter based upon published Power Spectral Density tests. It should be noted, however, that the dynamics of the shaping filter are most interesting at frequencies above the probable telescope pointing bandwidth. Within the system bandwidth, the gyro PSD's are largely flat, meaning that the drift rate is essentially random.

An earlier Kalman filter formulation has been modified to include both the contribution of image motion and the more advanced gyro noise model. The modification to add image motion simply includes the addition of a gyro command term corresponding to the projected image motion.

The addition of the gyro noise shaping filter should readily provide improved drift estimates at high sampling rates. As the sample rates decrease, however, the observability of drift decreases as well, to the point where the shaping filter should be omitted. This is due to the fact that the gyro shaping filter natural frequencies are far faster than the slow integration times that are required to track a dim star. The order of the estimator state equations may then be reduced by modelling gyro drift rate as random noise. The gyro drift angle is then a random walk process.

The error characteristics of the NASA DRIRU-II gyro package lead to lower overall estimate errors and improved pointing accuracy when compared to similar results for the Ferranti 125 gyro model. The documented tradeoff between increased gyro drift angle at longer integration times and increased star tracker noise at short integration times is still evident, resulting in the presence of an optimum sampling rate for a given star magnitude.

Further work needs to be completed before flight, however. This analysis did not include the sizable contribution that star image shape may have upon absolute accuracy or investigate in any depth the effect of nonlinear motion upon performance. If the uncertainty of image motion turns out to be enough to lose track of the target in the infrared field of view, then other methods will have to be devised to close the loop around the infrared target to achieve acceptable performance. The use of scientific instruments within the control scheme may serve this purpose.

References

[B&P–1] Bendat, Julius S., and Piersol, Allan G., *Random Data: Analysis and Measurement Procedures*, John Wiley and Sons, New York, 1971.

[B&L–1] Beynon, J.D.E., and Lamb, D.R., *Charge Coupled Devices and Their Applications*," McGraw–Hill Book Company, London, 1980.

[B&W–1] Blackstone, D.C., and Whitesell, W.J.,"Test Pad Motions at the Celestial Inertial Laboratory, Holloman AFB, N.M.," AIAA Guidance and Control Conference, Boston, Massachusetts, 1975, Paper No. 75-1103

[BRO–1] Brown, Robert A., "Planetary Observations with the Hubble Space Telescope," May, 1984.

[BRY–1] Bryson, A. E., and Ho, Y. C., *Applied Optimal Control*, Hemisphere Publishing Corporation, Washington, D.C., 1975.

[CRA–1] Craig, Robert J. G., "Theory of Operation of an Elastically Supported, Tuned Gyroscope," *IEEE Transactions on Aerospace and Electronic Systems*, Volume AES-8, No. 3, May 1972.

[DON–1] Donoghue, P.J., "Performance Characterisation of the Dry–Tuned–Gimbal Gyro for Application to Precision Spacecraft Attitude Reference Systems," Proceedings of the Ninth Symposium of Automatic Control in Space, Noordwijkerhout, Netherlands, 1982.

[DOU–1] Dougherty, H., et al., "Space Telescope Pointing Control System," *Journal of Guidance and Control," Vol. 5, No. 4, July–August 1982.*

[EIS–1] Eisenman, A.R., Alexander, J.W., and Stanton, R.H., "CCD Sensors for Spacecraft Optical Navigation," *AIAA 17th Aerospace Sciences Meeting,* AIAA Paper No. 79-0392, Jan., 1979.

[F&P–1] Franklin, G.F., and Powell, J.D., *Digital Control of Dynamic Systems,* Addison–Wesley Publishing Company, Menlo Park, Calif., 1980.

[G&G–1] Glavich, T.A., and Goss, W.C., "SIRTF Brassboard Review," Presentation notes to NASA–Ames, October 3, 1984.

[GOS–1] Goss, W.C., "Interpolation of Star Image Coordinates in a Charge–Coupled Image Sensor," Jet Propulsion Laboratory, Pasadena, Calif., Internal Memorandum No. 343-8-74-893, 1974.

[GGS–1] Goss, W.C., Glavich, T.A., and Salomon, P.M., "SIRTF Fine Guidance Sensor Imager Study," Jet Propulsion Laboratory, Pasadena, Calif., Report No. 901-18, Jan., 1982.

[GRE–1] Green, K.N., "AGS DRIRU II System Power Spectral Density Tests," Teledyne Systems Company, Internal Memorandum No. DRIRU:83:006, Feb., 1983.

[GOV–1] Green, K.N., Oshika, E.M., and Van Alstine, R.L., "Spectral Noise Performance of a High Accuracy Dry Tuned Gyroscope and the NASA Standard Redundant Dry Rotor Inertial Reference Unit (DRIRU II)," Ninth Biennial Guidance Test Symposium.

[HIL–1] Hill, R.E., "Preliminary Design with Supporting Studies of a Focal Plane Guidance Sensor Using a Charge–coupled Image Detector for the Space Shuttle Infrared Telescope Facility," Jet Propulsion Laboratory, Pasadena, Calif., Report No. 760-177, May, 1977.

[I&R–1] Irvine, R.B., and Ritter, J.W., "DRIRU–II—The NASA Standard High Performance Inertial Reference Unit," Rocky Mountain Guidance and Control Conference of the American Astronautical Society, February 1979.

[LPP–1] Lorell, K.R., Parsons, E.K., and Powell, J.D., "Image Motion Compensation for the Shuttle Infrared Telescope Facility," *IFAC Automatica*, Vol. 17, No. 4, pp. 555–562, July, 1981.

[M&L–1] Moler, C., and van Loan, C., "Nineteen Dubious Ways to Compute the Exponential of a Matrix," *SIAM Review*, Vol. 20, No. 4, 1978.

[MAR–1] Marx, H.B., "An Algorithm for Interpolation of Interelement Star Positions on the Fairchild 201 CCD," Jet Propulsion Laboratory, Pasadena, Calif., Internal Memorandum No. 343-8-75-510, 1975.

[MAR–2] Marx, H.B., "Optimal Coupling of Star Image Characteristics With Algorithm Form for an Accurate CCD Interelement Star Position Determination," Jet Propulsion Laboratory, Pasadena, Calif., Internal Memorandum No. 343-8-75-778, 1975.

[MAR–3] Marx, H.B., "Image Characteristics of a Zenith 130 mm Catadioptric Lens as Affected by Defocus and Lens Temperature," Jet Propulsion Laboratory, Pasadena, Calif., Internal Memorandum No. 343-8-75-732, 1975.

[PAR–1] Parsons, Eric, "Efficient Sampling Rates for Digital Controllers and Pointing Systems With Digital Solid State Detectors," Department of Aeronautics and Astronautics, Stanford University, Stanford, Calif., SUDAAR No. 533, June, 1982.

[P&P–1] Powell, J. David, and Parsons, Eric, "Control Systems Concepts for the Spacelab Infrared Telescope Facility," Department of Aeronautics and Astronautics, Stanford University, Stanford, Calif., SUDAAR No. 510, Jan., 1978

[PPL–1] Powell, J. David, Parsons, E., and Lorell, K.R., "Control Systems Designs for the Shuttle Infrared Telescope Facility," NASA Technical Memorandum 81159, Feb., 1980.

[PSH–1] Pue, A.J., Strohbehn, K., and Hunt, J.W., "Configuration Trade–offs for the Space Infrared Telescope Facility Pointing Control System," AIAA paper 85–1856.

[S&G–1] Salomon, P.M., and Goss, W.C., "A Microprocessor–controlled CCD Star Tracker," *AIAA 14th Aerospace Sciences Meeting*, AIAA paper No. 76-116, Jan., 1976.

[SAL–1] Sridhar, B., Aubrun, J.N., and Lorell, K.R., "The Design of a Precision Pointing Control System for the Space Infrared Telescope Facility," Lockheed Palo Alto Research Laboratory, Palo Alto, Calif.

[S&H–1] Stanton, R.H., and Hill, R.E., "A CCD Star Sensor for Fine Pointing Control of Spaceborne Telescopes," *Journal of Guidance and Control*, Vol. 3, March–April, 1980.

Appendix

```
C     -------------------------
C     STAR TRACKER SIMULATION
C     -------------------------
C
      REAL*4 IO,M
      DIMENSION HLS(4),VLS(4),HS(4),VS(4),PXY(11),
     1 PYF(11),PY(11),P(11)
      INTEGER*4 SIG(4,4),SUM
      M=11.0
      XC=0.3
      YC=0.50
      XCM=XC*30.
      YCM=YC*18.
      FOV=900.
      AMPNSE=50.
C
C     INTEGRATION PARAMETERS
      ISTEP=10
      ISTEP1=ISTEP+1
      P10=10.**.2
C
      DO 1030 JC=1,20
      T=0.01*(P10**(JC-1))
      IFLAG=0
C
C     PEAK SURFACE-CHARGE INTENSITY
      IO=T*(7.3E+9*(10.**(-.4*M)))/2829.4478
      S=0.0
C
C     INTEGRATE SURFACE-CHARGE DENSITY OVER PIXEL AREAS
C
C     I=PIXEL COLUMN
      DO 1002 I=1,4
      VLS(I)=0.
C
C     J=PIXEL ROW
      DO 1000 J=1,4
      XL=30.*(J-1)-52.0
      YL=18.-(I-1)*18.
      DO 102 KY=1,ISTEP1
      Y=YL+(KY-1)*18./ISTEP
      DO 100 KX=1,ISTEP1
      X=XL+(KX-1)*14./ISTEP
C
C     SURFACE-CHARGE DENSITY
      R=SQRT((X-XCM)**2+(Y-YCM)**2)
      IF (R.GT.43.25) PXY(KX)=0.
      IF ((R.LE.43.25).AND.(R.GE.14.41667)) PXY(KX)=
     1 IO*(1.-(R-14.41667)/28.83333)
  100 IF (R.LT.14.41667)PXY(KX)=IO
C
      H=14./ISTEP
      CALL QTFE(H,PXY,PYF,ISTEP1)
  102 PY(KY)=PYF(ISTEP1)
      H=18.0/ISTEP
      CALL QTFE(H,PY,P,ISTEP1)
      SIG(I,J)=P(ISTEP1)
C
C     CHECK FOR PIXEL SATURATION
      IF (SIG(I,J).GE.250000)SIG(I,J)=250000
      IF (SIG(I,J).EQ.250000)IFLAG=1
C
C     VERTICAL LINE SPREAD
 1000 VLS(I)=VLS(I)+SIG(I,J)
C
```

```
C     TOTAL SIGNAL
 1002 S=S+VLS(I)
C
C     WRITE SIG TO DATA FILE
C      DO 1003 I=1,4
C 1003 WRITE(31,5)(SIG(I,J),J=1,4)
C    5  FORMAT(' ',4I10)

C     HORIZONTAL LINE SPREAD
      DO 1004 J=1,4
      HLS(J)=0.
      DO 1004 I=1,4
 1004 HLS(J)=HLS(J)+SIG(I,J)
C
C     ERROR IN INTERPOLATED HORIZONTAL POSTION
C
      SH=1.5*(HLS(4)-HLS(1))+.5*(HLS(3)-HLS(2))
      HREG=SQRT(.4933333+1.90476*SH/S)
      XT=-.702381+HREG
C      XT=SH/S
C
C     (PIXELS)
      XE=-XC+XT
C
C     (ARCSEC)
      FOVH=1.29545*FOV/190.
      XEA=XE*FOVH
C
C     ERROR IN INTERPOLATED VERTICAL POSITION
C
      SV=1.5*(VLS(4)-VLS(1))+.5*(VLS(3)-VLS(2))
C
C     (PIXELS)
      YE=-YC-SV*1.31926/S
C      YE=-YC-SV/S
C
C     (ARCSEC)
      FOVV=FOV/244.0
      YEA=YE*FOVV
      IF (IFLAG.NE.1) WRITE(31,62)T,XE,YE
   62 FORMAT(' ',3F15.8)
C
C     SENSITIVITY OF INTERPOLATED POSTION TO LINE-SPREAD NOISE
C
      GO TO 1030
C     HORIZONTAL SENSITIVITY
      S2=S**2
      HS(1)=(-1.5/S-SH/S2)**2
      HS(2)=(-.5/S-SH/S2)**2
      HS(3)=(.5/S-SH/S2)**2
      HS(4)=(1.5/S-SH/S2)**2
C
C     VERTICAL SENSITIVITY
      VS(1)=(-1.5/S-SV/S2)**2
      VS(2)=(-0.5/S-SV/S2)**2
      VS(3)=(0.5/S-SV/S2)**2
      VS(4)=(1.5/S-SV/S2)**2
C
C     NOISE IN INTERPOLATED VERTICAL POSTION
C
      VE=0.
      VTRE=0.
      DO 1014 I=1,4
      SUM=0
      DO 1016 J=1,4
C
```

```
C     VERTICAL LINE-SPREAD NOISE (SHOT+BKGRND)
 1016 SUM=SUM+SIG(I,J)+AMPNSE**2
C
 1014 VTRE=VTRE+VS(I)*SUM
C
C     (PIXELS)
      VTRE=SQRT(VTRE)*1.31926
C
C     (ARCSEC)
      VTREA=VTRE*FOVV
      VETA=SQRT(VSTA**2+VTREA**2)
C
C     NOISE IN INTERPOLATED HORIZONTAL POSITION
C
      HTRE=0
      DO 1018 J=1,4
      SUM=0
      DO 1020 I=1,4
C
C     HORIZONTAL LINE-SPREAD NOISE
 1020 SUM=SUM+SIG(I,J)+AMPNSE**2
C
 1018 HTRE=HTRE+HS(J)*SUM
      HTRE=0.95238*HTRE/HREG
C
C     (PIXELS)
      HTRE=SQRT(HTRE)
C
C     (ARCSEC)
      HTREA=HTRE*FOVH
C
C     NOISE COVARIANCE FOR INTERPOLATED HORIZONTAL POSITION
      R=HTREA**2
C
C      IF (IFLAG.EQ.1) WRITE(22,42)
  42  FORMAT(' SATURATION')

 1030 CONTINUE
C 1030 WRITE(23,4)T,HTREA
    4 FORMAT(2(1PE14.6))
      STOP
      END
C
C
C
C    TRAPEZOIDAL INTEGRATION ROUTINE
C
      SUBROUTINE QTFE(H,Y,Z,NDIM)
      DIMENSION Y(1),Z(1)
      SUM2=0.
      IF (NDIM-1) 4,3,1
    1 HH=0.5*H
      DO 2 I=2,NDIM
      SUM1=SUM2
      SUM2=SUM2+HH*(Y(I)+Y(I-1))
    2 Z(I-1)=SUM1
    3 Z(NDIM)=SUM2
    4 RETURN
      END
```

```
C     CV4RCA.FOR
C
C
C     ------------------------------------
C     STAR TRACKER SIMULATION-SMEARED IMAGE,
C     NO MODIFICATION TO ALGORITHM
C     4 X 4 PIXEL SUBARRAY
C     ------------------------------------
C    Data for RCA 501 CCD, 512colX320rows,
C    Each pixel 30x30 microns
C    This version includes correction for
C    estimated tracking velocity
C
C
C
      REAL*8 IO,M,HLS(4),VLS(4),HS(4),VS(4),PXY(31),
     1 PYF(31),PY(31),P(31),SIG(4,4),TSIG(4,4)
      INTEGER*4 SUM,ISIG(4,4)
C
C    Input star magnitude, initial star location in
C    pixels, field background noise level, pixel
C    horizontal and vertical field of
C    view (arcsec).  Convert from pixels to microns.
C
      M=14.0
      XC=0.6
      YC=0.3
      XCM=XC*30.
      YCM=YC*30.
      AMPNSE=98.0
      P10=10.**0.2
C
C    Pixel field of view based on 18 arcmin dia.
C    --512colx320rows
C
      FOVV=5.625
      FOVH=5.625
C
C    Pixel Integration parameters
C
      ISTEP=30
      ISTEP1=ISTEP+1
C
C    Input scan rate (microns/sec) and angle (rad)
C
      SCAN=1.12
C      SCAN=.8
      ANGLE=3.14159/6.0
C
C    Assume a limited accuracy in known target motion
C
      SCANACC=01.0
      SCANA=SCANACC*SCAN
C
C-----------------------------------------------
C
C    Start loop A--vary pixel integration time
C
      DO 1030 JC=1,20
      IFLAG=0
      T=0.01*(P10**(JC-1))
      CT=100.0
      TI=T/(CT+1.0)
C
C    Peak surface charge intensity for a given
C    magnitude and integration time
```

```
C
      IO=TI*(7.3E+9*(10.**(-.4*M)))/2829.4478
C
C   Initialize signal levels
C
      S=0.0
      DO 3 I=1,4
      DO 3 J=1,4
    3 TSIG(I,J)=0.0
C
C   Start loop B--move star image across pixel
C   during a given integration
C
      DO 112 IT=1,CT+1
      XCMM=(IT-1)*COS(ANGLE)*SCAN*T/CT+XCM
      YCMM=(IT-1)*SIN(ANGLE)*SCAN*T/CT+YCM
C
C-----------------------------------------------
C
C   Integrate surface-charge density over pixel areas
C
C   I=Pixel Column
C
      DO 1002 I=1,4
      VLS(I)=0.
C
C   J=Pixel Row
C
      DO 1000 J=1,4
      XL=30.*(J-1)-60.0
      YL=30.-(I-1)*30.
      DO 102 KY=1,ISTEP1
      Y=YL+(KY-1)*30./ISTEP
      DO 100 KX=1,ISTEP1
      X=XL+(KX-1)*30./ISTEP
C
C   Surface charge density (trapezoidal image)
C
      R=SQRT((X-XCMM)**2+(Y-YCMM)**2)
      IF (R.GT.43.25) PXY(KX)=0.
      IF ((R.LE.43.25).AND.(R.GE.14.41667)) PXY(KX)=
     1 IO*(1.-(R-14.41667)/28.83333)
  100 IF (R.LT.14.41667)PXY(KX)=IO
C
C   Integrate surface charge density over pixel area
C
      H=30./ISTEP
      CALL QTFE(H,PXY,PYF,ISTEP1)
  102 PY(KY)=PYF(ISTEP1)
      H=30.0/ISTEP
      CALL QTFE(H,PY,P,ISTEP1)
      SIG(I,J)=P(ISTEP1)
C
      TSIG(I,J)=SIG(I,J)+TSIG(I,J)
C
C   Check for pixel saturation
C
C      IF (TSIG(I,J).GE.390000.)TSIG(I,J)=390000.
C      IF (TSIG(I,J).EQ.390000.)IFLAG=1
C
 1000 CONTINUE
 1002 CONTINUE
  112 CONTINUE
C
C -----------------------------------------------
C
```

```
C   Convert pixel signal to integer value
C
      TS=0.0
      DO 111 IR=1,4
      DO 111 JR=1,4
      TS=TS+TSIG(IR,JR)
 111  ISIG(IR,JR)=TSIG(IR,JR)
C
C   Calculate horizontal line spread
C
      DO 1004 J=1,4
      HLS(J)=0.
      DO 1004 I=1,4
 1004 HLS(J)=HLS(J)+ISIG(I,J)
C
C   Calculate vertical line spread
C
      DO 1006 I=1,4
      VLS(I)=0.
      DO 1005 J=1,4

 1005 VLS(I)=VLS(I)+ISIG(I,J)
 1006 S=S+VLS(I)
C
C   Error in interpolated horizontal position
C   with no geometrical correction factors
C
      SH=1.5*(HLS(4)-HLS(1))+.5*(HLS(3)-HLS(2))
      XT=SH/S
C
C   Correct postion estimate based on known
C   target velocity. Positions calculated for
C   uncertain target velocities as well.
C
      XTCV=XT+T*SCANA*COS(ANGLE)/(2.0*30.0)
      XTCV9=XT+T*0.9*SCAN*COS(ANGLE)/(2.0*30.0)
      XTCV99=XT+T*0.99*SCAN*COS(ANGLE)/(2.0*30.0)
      XTC999=XT+T*0.999*SCAN*COS(ANGLE)/(2.0*30.0)
C
C   Error in pixels
C
      XE=-XCMM/30.0+XTCV
      XEU=-XCMM/30.0+XT
      XE9=-XCMM/30.0+XTCV9
      XE99=-XCMM/30.0+XTCV99
      XE999=-XCMM/30.0+XTC999
C
C   Convert to arcsec
C
      XEA=XE*FOVH
      XEUA=XEU*FOVH
      XE9A=XE9*FOVH
      XE99A=XE99*FOVH
      XE999A=XE999*FOVH
C
C   Error in interpolated vertical position
C   with no geometrical correction factors
C
      SV=1.5*(VLS(4)-VLS(1))+.5*(VLS(3)-VLS(2))
      YT=-SV/S
C
C   Correct vertical postion estimate based on
C   known target velocity. Also calculate the
C   effect of motion uncertainty.
C
      YTCV=YT+T*SCANA*SIN(ANGLE)/(2.0*30.0)
```

```
      YTCV9=YT+T*.9*SCAN*SIN(ANGLE)/(2.0*30.0)
      YTCV99=YT+T*.99*SCAN*SIN(ANGLE)/(2.0*30.0)
      YTC999=YT+T*.999*SCAN*SIN(ANGLE)/(2.0*30.0)
C
C   Calculate error in pixels
C
      YE=-YCMM/30.0+YTCV
      YEU=-YCMM/30.0+YT
      YE9=-YCMM/30.0+YTCV9
      YE99=-YCMM/30.0+YTCV99
      YE999=-YCMM/30.0+YTC999
C
C   Convert to arcsec
C
      YEA=YE*FOVV
      YEUA=YEU*FOVV
      YE9A=YE9*FOVV
      YE99A=YE99*FOVV
      YE999A=YE999*FOVV
C
      ERR=SQRT(XEA**2+YEA**2)
      ERRU=SQRT(XEUA**2+YEUA**2)
      ERR9=SQRT(XE9A**2+YE9A**2)
      ERR99=SQRT(XE99A**2+YE99A**2)
      ERR999=SQRT(XE999A**2+YE999A**2)

C
C   Print results
C
      WRITE(34,62)T,ERR,ERRU,ERR9,ERR99,ERR999
 62   FORMAT(' ',6E12.5)
C      IF (IFLAG.EQ.1) WRITE(34,63)
 63   FORMAT(' SATURATION')
C
C-----------------------------------------------
C
C   SENSITIVITY OF INTERPOLATED POSTION TO
C   LINE-SPREAD NOISE
C
C   Calculate horizontal uncertainty terms
C
      S2=S**2
      HS(1)=(-1.5/S-SH/S2)**2
      HS(2)=(-.5/S-SH/S2)**2
      HS(3)=(.5/S-SH/S2)**2
      HS(4)=(1.5/S-SH/S2)**2
C
C   Calculate vertical uncertainty terms
C
      VS(1)=(-1.5/S-SV/S2)**2
      VS(2)=(-0.5/S-SV/S2)**2
      VS(3)=(0.5/S-SV/S2)**2
      VS(4)=(1.5/S-SV/S2)**2
C
C   Calculate noise in interpolated vertical position
C
      VE=0.
      VTRE=0.
      DO 1014 I=1,4
      SUM=0
      DO 1016 J=1,4
C
C  Calculate the vertical line spread noise as a sum of
C  Shot noise and background noise
C
 1016 SUM=SUM+ISIG(I,J)+AMPNSE**2
```

```
C
 1014 VTRE=VTRE+VS(I)*SUM
C
C  Vertical position jitter in pixels
C
      VTRE=SQRT(VTRE)
C
C  Convert vertical position jitter to arcsec
C
      VTREA=VTRE*FOVV
C
C  Calculate noise in interpolated horizontal position
C
      HTRE=0
      DO 1018 J=1,4
      SUM=0
      DO 1020 I=1,4
C
C  Calculate the horizontal line spread noise as a sum of
C   Shot noise and background noise
C
 1020 SUM=SUM+ISIG(I,J)+AMPNSE**2
C
 1018 HTRE=HTRE+HS(J)*SUM
C
C  Horizontal position jitter in pixels
C
      HTRE=SQRT(HTRE)
C
C  Convert horizontal position jitter to arcsec
C
      HTREA=HTRE*FOVH
C
C  R= noise covariance for interpolated position jitter
C
      R=HTREA**2+VTREA**2
C
C  Output
C
 1030 WRITE(35,4)T,SQRT(HTREA**2+VTREA**2),R
    4 FORMAT(3(1PE14.6))
      STOP
      END
C
C*****************************************
C
C    Trapezoidal integration routine
C
      SUBROUTINE QTFE(H,Y,Z,NDIM)
      REAL*8 Y(1),Z(1)
      SUM2=0.
      IF (NDIM-1) 4,3,1
    1 HH=0.5*H
      DO 2 I=2,NDIM
      SUM1=SUM2
      SUM2=SUM2+HH*(Y(I)+Y(I-1))
    2 Z(I-1)=SUM1
    3 Z(NDIM)=SUM2
    4 RETURN
      END
```